Oxide Nanowire Microfluidics for the Analysis of Extracellular Vesicles

PAISRISARN Piyawan

Table of Contents

This thesis is dedicated to my beloved grandmother who passed away from cancer.

List of Abbreviations

ALD	Atomic Layer Deposition
Alexa488	a cytoskeleton staining fluorescent dye
BSA	Bovine Serum Albumin
CCD-18Co	a human colon cell line
CD147	Cluster of Differentiation 147
CD63	Cluster of Differentiation 63
CD81	Cluster of Differentiation 81
CD9	Cluster of Differentiation 9
CO_2	Carbon dioxide
DI water	Deionized water
DMEM	Dulbecco's Modified Eagle Medium
DNA	Deoxyribonucleic Acid
ECR	Electron Cyclotron
EDS	Energy Dispersive x-ray Spectroscopy
EM-CCD	Electron Multiplying Charge-Coupled Device
EMEM	Eagle's Minimal Essential Medium
EV	Extracellular Vesicle
Exo-L	Large Exosome
Exo-S	Small Exosome
FBS	Fetal Bovine Serum
FESEM	Field Emission Scanning Electron Microscope
HepG2	a human liver cancer cell line
HMTA	Hexamethylenetetramine
Hoechst33342	a nucleus staining fluorescent dye
HRTEM	High Resolution Transmission Electron Microscope
Hs578Bst	a human breast cell line
HTC116	a human colon cancer cell line
IEP	Isoelectric Point
M3-PALS	Mixed Mode Measurement-Phase Analysis Light Scattering

MCF10A	a human mammary gland epithelial cell line
MDA-MB-231	a human breast cancer cell line
MgO	Magnesium Oxide
miRNA/microRNA	Micro Ribonucleic Acid
MV	Microvesicle
NGS	Next Generation Sequencing
NH_3	Ammonia
NiO	Nickel Oxide
NTA	Nanoparticle Tracking Analysis
NW	Nanowire
PbO	Lead Oxide
PBS	Phosphate-Buffered Saline
PDMS	Poly(dimethylsiloxane)
PEEK	Polyetheretherketone
PEI	Polyethylenimine
PKH26	an exosome staining fluorescent dye
RNA	Ribonucleic Acid
SAED	Selective Area Electron Diffraction
SEM	Scanning Electron Microscope
Si substrate	Silicon substrate
SP-IRIS	Single Particle Interferometric Reflectance Imaging System
STEM	Scanning Transmission Electron Microscope
TEM	Transmission Electron Microscope
UEV	Urinary Extracellular Vesicle
XRD	X-Ray Diffraction
ZB	Zinc Blende
ZnO	Zinc Oxide
$Zn(NO_3)_2.6H_2O$	Zinc Nitrate Hexahydrate
ZnO/SiO_2	Zinc Oxide coated with Silicon dioxide layer (core/shell)
ZnO/TiO_2	Zinc Oxide coated with Titanium dioxide layer (core/shell)

Chapter 1. General Introduction

Extracellular vesicles (EVs) have shown promising features as biomarkers for early cancer diagnoses and prognoses. The ability to analyze EVs could strongly impact cancer-related research studies. The outer layer of cancer cell-derived EVs consists of organotropic metastasis-induced membrane proteins and specifically enriched proteoglycans, and these molecular compositions determine EV surface charge. Although many efforts have been devoted to investigating the correlation between EV subsets obtained through density-, size-, and immunoaffinity-based captures and expressed membrane proteins, understanding the correlation between EV subsets obtained through surface charge-based capture for effective downstream analysis of EVs is lacking. Here, we propose a methodology to isolate EV subsets obtained through surface charge-based capture using oxide nanowire microfluidic devices. First, we fabricate oxide nanowires with different surface chemical properties providing diverse surface charges based on isoelectric points of the materials. And, with the ZnO nanowire device, whose use does not require any purification and concentration processes, we demonstrated the correlation between negatively charged EV subsets and expressed membrane proteins of colon cancer cells for cancer detection. We have shown the potential of ZnO nanowires to capture EVs that is rapid and simple compared to conventional methods. Nevertheless, key parameters including crystallinity and morphology of ZnO nanowires to maximize the EVs capture performance had not yet been investigated. Thus, we subsequently present a comprehensive investigation that highlights the correlation of ZnO nanowire physicochemical properties to the capture performance of breast cancer cell-derived EVs. Finally, we adapted our findings in tunable nanowire properties with highly efficient label-free capturing of EVs for other two alternative applications rather than cancer detection, including an EV classification device for specific sorting of EV subpopulations based on surface charge and a nanowire-based blood purification model for eliminating of cancer-derived EVs to suppress the progression of breast cancer via EV-induced metastasis inhibition.

Extracellular vesicles (EVs) are spherically structured, cell-derived membrane vesicles and they play a crucial role in cell-to-cell communication. These micro- and nano-sized vesicles carry molecular messages, including proteins, lipids, DNAs, RNAs, and metabolites (**Fig.1**). The molecules reflect the physiological and pathological conditions of parent cells and provide useful information for clinical applications including early detection, diagnosis, and prognosis of diseases as well as the utilization in monitoring surgery and treatment responses.[1-10] EVs have been identified in many different biological fluids like whole blood, plasma, serum, urine, saliva, breast milk, *etc*.[11, 12]. Among these fluids, urine stands out as a non-invasive sample fluid that is easy and inexpensive to obtain and can be collected over time to monitor changes. The urinary extracellular

vesicles (UEVs) were first isolated by Wiggins *et al.*.[13] Consequently, the work of Pisitkun *et al.*[14] had a major impact of raising interest in UEVs by demonstrating proteomic analysis of urinary exosomes associated with renal diseases (kidney disorders). From that, the potential for clinical applications of UEVs became established. Recent reports have shown the presence of such molecules as RNAs, microRNAs, and proteins, which can be used as potentially as biomarkers in renal diseases (*e.g.*, diabetic kidney disease),[15] urological malignancies (*e.g.*, prostate, bladder and kidney cancers)[16-19], non-urological malignancies (*e.g.*, lung, liver, pancreas cancers),[20] and arterial hypertension[21, 22] in UEVs.

However, there is a concern in application of UEVs to analysis due to the great variability among isolation techniques that have been used; this has resulted in it being difficult to apply the most effective protocol that is convenient and universal in a clinical setting. Thus, the lack of a standardized protocol remains a significant limitation in the field of EV analysis, especially, when all analytical validations of the assay have to be considered including accuracy, precision, specificity, limits of detection and quantification. Comprehensive standardized guidelines for isolation of EVs[23] and over all analytical processes [24, 25] have been provided that suggest all experimental details as well as critical evaluations in the EV analysis procedures. Some researchers have discussed the development of a variety of EV isolation and interrogation approaches, and highlighted potentials and limitations.[26] Others have addressed the whole range of methods that are used for human EV isolation and characterization.[27]

The overall workflow procedures for studying EVs consist of three main steps (**Fig. 2**): pretreatment, isolation, and downstream analysis. The key to successful determination of EVs mostly relies on the sample preparation processes of the pre-analysis and isolation since they directly determine the qualitative and quantitative information of EVs from that sample. Before carrying out any experiment, consideration must be given to what target information is expected to be obtained from UEVs in the downstream analysis, *e.g.* the morphology, variety of components, and proteomic and genomic information. The use of force in some techniques may lead to break-up or deformation of the EV structure. There are many techniques that have been developed for EV isolation. In this literature review, we focus on four principles that rely on specific properties of the EVs including size and density, solubility, and surface affinity, and that can be realized in an integrated microfluidic system. Each technique has its own key potential and limitations, as shown in **Table 1**. A number of recent studies have tried to combine two or more different techniques together to improve isolated matter purity, yield and richness of the biomolecule types, *e.g.* ultra-centrifugation with ultra-filtration (UC-UF),[28, 29]

ultra-centrifugation with size-exclusion chromatography (UC-SEC),[29, 30] and ultra-filtration with size-exclusion chromatography (UF-SEC).[31, 32] Still, all these techniques have intensive labor requirements.

Microfluidics techniques are integrated platform that have been developed within the lab-on-a-chip concept promoting high robustness, sensitivity, and selectivity of EV analysis.[33-36] As noted earlier, the ideal analysis methodology is to detect EVs directly without any extensive pretreatment steps from urine, and numerous studies have tried to find out whether realizing this is possible.

In 2017, we proposed a novel approach to UEV isolation microfluidics that enables EV collections at high efficiency and by in situ extractions of diverse miRNA molecules that significantly exceed the number of items being extracted by the conventional ultracentrifugation method and a commercially available kit.[37] This methodology moves researchers toward the goal of miRNA-based noninvasive and simple early disease diagnoses and timely medical checkups from urine. Although nanowires have shown great potentials for analyzing properties of cells or intracellular components, none of the previous studies have dealt with applications to collect EVs. We discovered utilization of distinct properties of nanowire, including the relatively small size as EV molecule, the large surface-to-volume ratio for high adsorption area, and the variations of surface charge, promoting highly sensitive interaction and the reduction of processing time and sample volume. Furthermore, oxide nanowires provide high flexibility in on demand application by tailoring physical property and surface chemistry in the fabrication process.

Herein, in this research, various oxide nanowire devices were fabricated for analysis of EVs and its contents, namely membrane protein markers and EV-encapsulated miRNAs. This thesis provides the series of nanowire-based device development in order to improve performance and maximize the potentials of nanowire-based devices by manipulating surface physicochemical properties of oxide nanowires. In chapter 2, three types of metal oxide nanowires with distinct surface chemistry were used to evaluate and identify the most suitable candidate material for label-free capturing of EVs. In addition, this device was applied to realize membrane protein profiling of EVs obtained via charge-based capture for detection of colon cancer within a single device. Chapter 3 provides a comprehensive investigation of ZnO nanowire in terms of physical properties in EV capture performance. Various morphologies and crystallinities of nanowires were tailored using an ammonia-assisted hydrothermal method, then the correlation between device efficacy and physicochemical property of nanowires from different growth conditions were observed. Our discoveries in chapter 2 and 3 were subsequently utilized to promote specific adsorption of EVs on nanowires based on crystallinity. Moreover, to achieve releasability of the captured molecules for further downstream analysis, we additionally apply an

elution essay promoting specific desorption of EVs based on ionic strength and surface charge. This classification concept to sort EV subpopulations is described in Chapter 4, we provide the analysis of distinct protein membrane markers and EV-encapsulated miRNAs profiling in each EV fraction. Last but not least, in Chapter 5, an alternative utilization of the nanowire-based methodology in cancer therapeutic application, as a model of blood purification device, were proposed for the first time. Since the device application had been mostly focusing on cancer diagnosis and monitoring in previous studies. Growing of evidences indicated that EVs involve in metastasis and proliferation of cancers, but, thus far, how their elimination from biofluid in order to inhibit the abnormal growth of cell has been poorly understood. Here, we described an EV-elimination device using nanowires which can efficiently remove EV-miRNAs from cancer cell supernatant for inhibiting abnormal growth in recipient cell without toxicity to cell. Finally, Chapter 6 is dedicated to some concluding remarks and future perspectives.

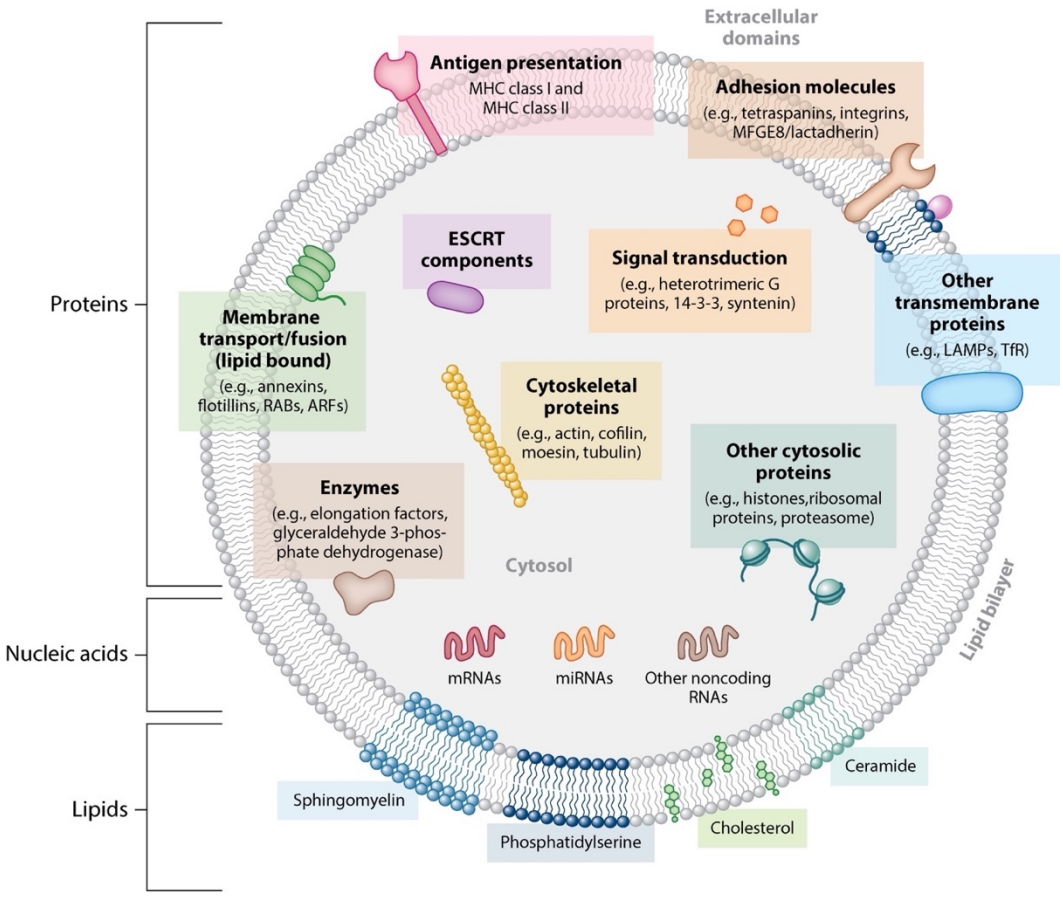

Colombo M, et al. 2014.
Annu. Rev. Cell Dev. Biol. 30:255–89

Fig. 1 Overall composition of extracellular vesicles (EVs).

Schematic representation of the composition (families of proteins, lipids, and nucleic acids) and membrane orientation of EVs. Examples of tetraspanins commonly found in EVs include CD63, CD81, and CD9.

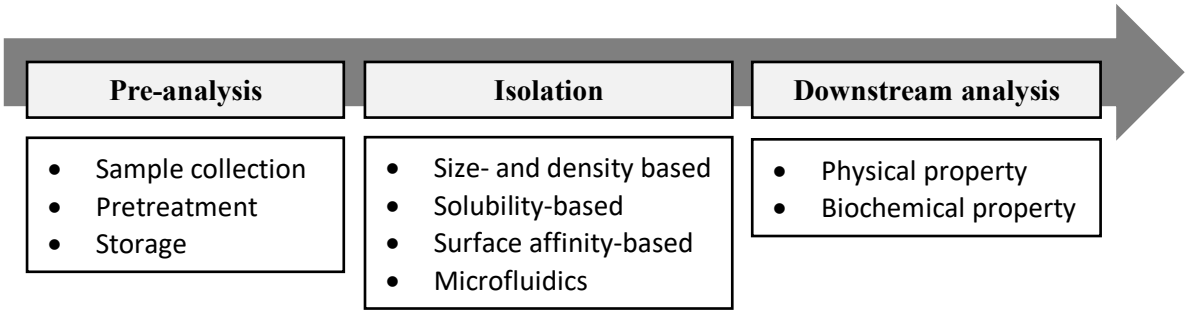

Fig. 2 The workflow of analytical procedure of EVs.

The key to successful determination of EVs mostly relies on the sample preparation processes of the pre-analysis and isolation since they directly determine the qualitative and quantitative information of EVs from that sample. The characterization of EVs is primarily based on the variety of their biophysical and biochemical properties which may be used to determine the molecular composition of vesicles for identifying markers of disease.

Table 1 Summary of isolation techniques for extracellular vesicles.

Isolation Technique	Principle of Technique	Advantages	Disadvantages
Ultracentrifugation	Size and density based seperation by applied centrifugal force	Large sample capacity Large yield	High instrument cost Labor intensive Time consuming Low purity
Ultrafiltration	Size based seperation by ultra-fine pore size membrane	Low instrument cost Fast processing	Vesicles trapping Size overlapping Protein contaminants
Size-Exclusion Chromatography	Size and mobility based separation by packed column with porous materials	High purity Low protein contaminants High yield	Require additional concentration step Long run time
Precipitation	Solubility based seperation by substances in a solution	Fast processing High yield High quality for RNA profilling	Protein contaminants Chemical required
Immuno-based technique	Surface affinity based separation by antibody	High specific High recovery	High antibody cost Low sample capacity
Microfluidics	Surface affinity based separation by various materials	Very fast High sensitivity High selectivity	Complexity of device High cost

Chapter 2. Molecular Profiling of Extracellular Vesicles via Charge-Based Capture using Oxide Nanowire Microfluidics

2.1 Introduction

Extracellular vesicles (EVs; diameters of 30-2000 nm) are membrane vesicles, such as exosomes, microvesicles, and apoptotic bodies,[38-40] and the EVs contain nucleic acids, proteins, and metabolites. The EVs are secreted into the body's blood circulation system by most types of cells. Furthermore, EVs maintain biological functions after their internalization into recipient cells, and therefore, they can regulate cellular information.[41-45] Since EVs can preserve cancer- and disease-related genetic and proteomic information,[46-48] they have been used as a source of cancer and disease biomarkers. To take advantage of their full potential as biomarkers, methodologies that not only capture special subsets of EVs but also profile membrane proteins of EVs are required to identify the correlation between the captured EV subsets and profiled EV membrane proteins.

Current methodologies for EV capture are mainly divided into three groups:[40] density-based capture using ultracentrifugation or differential centrifugation,[49] size-based capture using size exclusion chromatography, and immunoaffinity based capture (for specific membrane proteins, e.g., CD9, CD63, and CD81). In addition, polymer precipitation (for example, ExoQuickTM, a size-based capture according to the kit manufacturer's instruction manual)[50] and microfluidic-based platforms (density-, immunoaffinity-, and size-based captures)[34] have been reported as emerging alternatives. The EV subsets obtained through density-, size-, and immunoaffinity-based captures have EV information corresponding to EV contents or specific membrane proteins (CD9, CD63, or CD81), but not molecular compositions of the EV surface that reflect donor cell information.

Since the outer layer of cancer cell-derived EVs can consist of lipid bilayers, organotropic metastasis-induced membrane proteins,[51] and specifically enriched proteoglycans,[52] the idea that EVs have a correlation between surface molecules and charge is rational. And therefore, understanding the correlation between EV subsets obtained through surface charge-based capture and expressed membrane proteins should also be important, as is the case with density-, immunoaffinity-, and size-based captures. Fewer efforts have been devoted to investigating the correlation between EV subsets obtained through surface charge-based capture and expressed membrane proteins. Among the developed methodologies, the charge-based capture has advantages of rapid and simple operation with high EV yield and high RNA throughput (**Table 2**).

We previously introduced a nanowire-based concept that could collect over 99% of the EVs present; the analysis targets were urinary microRNAs.[37, 53] The correlation between EV subsets obtained through surface charge-based capture and expressed membrane proteins has not been addressed as yet, however. Here we propose a methodology using oxide nanowires with different surface potentials to subdivide EVs based on surface charge and we investigate a correlation between surface charge and expressed proteins on the EVs.

2.2 Method

a. Cell culture and EV purification by ultracentrifugation.

Human breast adenocarcinoma cells (MDA-MB-231, American Type Culture Collection Co., Ltd.) were cultured in Dulbecco's modified eagle medium (DMEM, Thermo Fisher Scientific Inc.) with 10% exosome-depleted fetal bovine serum (FBS, System Biosciences, LLC.) without any addition of antibiotics. In each passage, 2×10^6 cells were seeded into 15 mL of cell medium in a culturing flask and cultured in an incubator (Panasonic Corp.) at 37ºC and in 5% CO_2. After 48 h, the cell medium was taken from the culturing flask and filtered through a 0.22-μm filter (Merck Millipore Ltd.) to remove cellular debris. Next, 20 mL of the filtered medium was ultracentrifuged (80 min, 4°C, 110,000 *g*). After discarding the supernatant, we added 10 mL of 0.22-μm filtered phosphate-buffered saline (PBS; Thermo Fisher Scientific Inc.) to wash the collected EVs, and this was ultracentrifuged again (80 min, 4°C, 110,000 *g*). After discarding the supernatant, 1 mL of 0.22-μm filtered PBS was added to collect EVs, and the collected EVs were stored at 4ºC. For HepG2, HTC116 (American Type Culture Collection Co., Ltd.), CCD-18Co, and Hs578Bst, the media we used were DMEM, McCoy's 5A (American Type Culture Collection Co., Ltd.), Eagle's minimal essential medium (EMEM, American Type Culture Collection Co., Ltd.), and Hybri-Care Medium (American Type Culture Collection Co., Ltd.), respectively. EV zeta potential was measured at 25ºC using the Zetasizer nano-ZS (Malvern Panalytical Ltd) by means of the M3-PALS (Mixed Mode Measurement-Phase Analysis Light Scattering).

b. Nanowire fabrication and characterization.

We fabricated ZnO nanowires on Si substrate using the previously reported method,[37] and deposited a TiO_2 layer or a SiO_2 layer on the ZnO nanowires by atomic layer deposition. The morphology and the composition of ZnO (bare) (**Fig. 3**), ZnO/TiO_2 (core/shell) (**Fig. 4**), and ZnO/SiO_2 (core/shell) (**Fig. 5**) nanowires were characterized by field emission scanning electron microscope (FESEM), scanning transmission electron microscopy (STEM) and energy dispersive x-ray spectroscopy (EDS). For the cross-sectional SEM-EDS analysis, we utilized an accelerating voltage of 15 kV. For the single-nanowire STEM-EDS analysis, we

used an accelerating voltage of 30 kV. The EDS mapping images were 512 × 384 pixels and the delay time for each pixel was 0.1 ms. The images were integrated for 100 cycles. The peaks of Zn Kα (8.630 keV), O Kα (0.525 keV), Si Kα (1.739 keV), and Ti Kα (4.508 keV) were chosen to construct the elemental mapping images. Nanowire zeta potential was measured using commercial apparatuses (Otsuka Electronics Co., Ltd.).

c. EV capture on nanowires.

We used a custom-made Teflon holder in the experimental capturing of EVs on each nanowire. The nanowires on a substrate were set into one part of the unassembled holder (**Fig. 6a**), and the holder parts were then fasted together with screws (**Fig. 6b**). 1 mL of EV-suspended PBS was supplied to the holder and the EVs were captured onto each nanowire. EV concentration and size were analyzed using a nanoparticle tracking analysis (NTA) instrument (Malvern Panalytical, Ltd.). After appropriate dilutions, video data were collected 5 times for a 60-s time period for each video. Camera level and detection threshold were set to 13 and 5, respectively. Data analysis was performed automatically by NanoSight NTA 3.2 software (Malvern Panalytical, Ltd.). After drying the EVs on the ZnO nanowires, we coated the EVs with gold film via plasma exposure (Vacuum Device Inc.) to a thickness around 25 nm for FESEM imaging (Carl Zeiss AG).

d. Nanowire microfluidic device fabrication.

A glass substrate (26 Å ~ 38 mm, Matsunami Glass Ind., Co., Ltd.) was cleaned and then heated at 300ºC. A solution mixture of 75 mM zinc acetate dihydrate and 75 mM ethanolamine was prepared by dissolving them in 2-methoxyethanol. This solution was used to spin-coat a ZnO layer on the glass substrate (7000 rpm, 30 s), followed by heating of the coated substrate at 300ºC for 3 min; this ZnO layer deposition step was repeated 6 times. Next, positive photoresist (OFPR8600, Tokyo Ohka Kogyo Co., Ltd.) was coated on the substrate (1500 rpm, 120 s) and then the nanowire pattern was formed by photolithography. The ZnO nanowires were grown by immersing the substrate in a solution mixture of 20 mM hexamethylenetetramine (HMTA, Wako Pure Chemical Industries, Ltd.) and 20 mM zinc nitrate hexahydrate ($Zn(NO_3)_2.6H_2O$, Thermo Fisher Scientific Inc.) at 95ºC for 8 h. After removal of the resist, a sheet of poly(dimethylsiloxane) (PDMS) (Silpot 184, Dow Corning Corp.) patterned with microchannels was bonded to the substrate (**Fig. 7**).

e. In-situ profiling of EV membrane proteins.

When introducing EVs into the nanowire device, we allowed the EVs to be captured onto the ZnO nanowires for 1 h at room temperature; then PBS was introduced into the device to remove the uncaptured EVs. Next, we introduced 1% bovine serum albumin (BSA) solution (Kirkegaard & Perry Laboratories, Inc.) into the device and let it stand for 15 min. After washing out the device using PBS, we introduced a mouse

monoclonal anti-human AlexaFluor488-labeled CD63 antibody (10 μg/mL, Santa Cruz Biotechnology, Inc.) or a mouse monoclonal anti-human CD9, CD81, and CD147 antibody (10 μg/mL, Abcam, Plc.) into the device, and let the antibody solution stand for 15 min. Lastly, we washed out the device using PBS. For CD9, CD81, and CD147 detections, additionally, we introduced a goat polyclonal anti-mouse AlexaFluor488-labeled IgG secondary antibody (5 μg/mL, Abcam, Plc.) into the device, and let the secondary antibody solution stand for 15 min. Finally, we washed out the device using PBS and followed that by fluorescence observation with an EM-CCD camera (C9100-13, Hamamatsu Photonics K.K.; measured area, 212 μm^2) through the fluorescence microscope (Olympus, Co., Ltd.) (**Fig. 8**), and then the fluorescence intensity was analyzed by image-processing software (AquaCosmos, Hamamatsu Photonics K.K.; measured area, 212 μm^2).

2.3 Results and Discussion

a. Surface charge-based EV capture followed by in-situ profiling of EV membrane protein via the oxide nanowires in microchannels.

For charge-based EV capture followed by in-situ profiling of EV membrane proteins, we introduce biological samples and then fluorescently labelled antibodies into an array of the oxide nanowires in microchannels; we call this a nanowire device. First, the nanowires harvest EVs from the introduced biological samples, and then, the fluorescently labelled antibodies demonstrate in-situ profiling of EV membrane proteins corresponding to the antibody types. **Fig. 9** is a schematic of our proposed concept to perform surface charge-based EV capture followed by in-situ profiling of EV membrane protein via the nanowire device. Oxide nanowires may be a good candidate for EV surface charge-based capture due to the diverse isoelectric points of oxides[54] and the large surface-to-volume ratios of nanowire structures.[37, 55] The microchannels play an important role in shortening distances and increasing contact frequencies between nanowires and EVs[56]. Since the herringbone structure in our previous design[37] made a convection flow, which may have the risk of noncharge-based capture of EVs, we fabricated the microchannels without mixing structures (straight channel design). Thus, the present nanowire device allows us to analyze the relationship between surface charge and proteins on EVs.

To confirm the feasibility of charge-based capture on nanowires, we captured EVs onto charged surfaces of the nanowires (**Fig. 10a**). The cell-derived EVs in PBS, which were purified by ultracentrifugation, had a mean zeta potential of -21.0 mV (**Fig. 10b**) and a mean diameter of about 94.6 nm (**Fig. 10c**). We deposited two different oxide materials, TiO_2 and SiO_2, on ZnO nanowires to form different surface potentials

of the nanowires in the same pH range. Around pH = 7, the ZnO (bare) nanowires had a positively charged surface, and the ZnO/TiO_2 (core/shell) and the ZnO/SiO_2 (core/shell) nanowires had a negatively charged one (**Fig. 10b**). The ZnO (bare), ZnO/TiO_2 (core/shell), and the ZnO/SiO_2 (core/shell) nanowires could capture EVs in response to the surface potential (**Fig. 10d**). Although the positively charged surface of the ZnO (bare) nanowires showed the highest capture efficiency among the three types of nanowires, the negatively charged surface of the ZnO/TiO_2 and the ZnO/SiO_2 nanowires could also capture EVs. This result implied that the captured subsets of EVs using each nanowire type were different; the ZnO (bare) nanowires could capture negatively charged EVs, while the ZnO/SiO_2 nanowires could capture positively charged EVs. The ZnO (bare) nanowires were our first choice in this paper from the standpoint of capture efficiency; however, the ZnO/SiO_2 nanowires also would be good candidates to further investigate EV characteristics of the positively charged EVs. The EV subsets obtained through charge-based capture would provide a unique insight into EV information corresponding to EV contents or specific membrane proteins. We thought it reasonable that surface potential, density and aspect ratio of nanowires could further improve the capture efficiency of EVs. Considering the relationship between zeta potential of nanowires and capture efficiency, we assumed more positive surface materials, such as NiO, MgO, and PbO,[54] would be better suited to enhance the capture efficiency. Since the ZnO surface area relates to the capture efficiency, increasing the nanowire density in the array with enough space for EVs to enter and increasing the aspect ratio of the nanowires by making them thinner and longer, would also offer ways to enhance the capture efficiency. Using a precursor of NiO, MgO, and PbO for atomic layer deposition and adding PEI and ammonia into the growth solution for making nanowires thinner and longer such as done in the literatures[57-59] would allow researchers to capture more EVs in the nanowire device.

For in-situ profiling of the membrane protein of the EVs, here, we used the ZnO (bare) nanowires to capture EVs. We fabricated ZnO nanowires on a glass substrate (**Fig. 11a**; 700 μm × 15 mm; height, 2 μm) and then bonded a sheet of poly(dimethylsiloxane) (PDMS) with microchannels to the substrate (**Fig. 11b**; 700 μm × 15 mm; height, 20 μm) to form the nanowire device (**Fig. 11c**). Analysis of an FESEM image showed that the nanowires had an average diameter of 100 nm and the nanowire density was 20 nanowires/μm^2 (**Fig. 11d**). We could estimate 2.0×10^8 nanowires were presented in the fabricated area, resulting in around a 12-fold larger surface-to-volume ratio compared to the no-nanowire surface. To introduce biological samples, we supplied 1 μL of sample through an inlet, and aspirated the sample using a vacuum pump (**Fig. 11e**). Considering the spatial volume of one microchannel, we could introduce 0.21 μL amounts of biological samples

into the microchannel. Generally, EV concentrations in biological samples[60] are 10^8 - 10^{10} /mL and the number of EVs in the microchannel are 2.0×10^5 - 2.0×10^7, and therefore, we could say that the present nanowire device has a large enough number of nanowires (2.0×10^8 nanowires) to capture EVs, as charge-based subsets, in the biological samples. We verified whether the nanowire device demonstrated in-situ profiling of the membrane protein of the charge-based captured EVs onto the ZnO (bare) nanowires. We introduced EVs and fluorescence-labeled antibodies into the nanowire device, and followed that by observing the fluorescence intensities (**Fig. 12**). Compared with in-situ profiling of the membrane protein of EVs in a microchannel without nanowires and no EVs in the nanowire device, we confirmed charge-based EV capture followed by in-situ profiling of EV membrane proteins using the ZnO nanowires (**Fig. 11f**). The FESEM images also allowed us to confirm the EV capture onto the ZnO nanowires (**Fig. 11g**). To show the superiority of our nanowire-based methodology to the conventional methodology, we used a 96-well plate, protein adsorption platform for comparison (**Fig. 11h**). Comparison of p-values between the cases of EVs captured onto nanowires and EVs captured onto plate wells of the 96-well plate showed that nanowires could capture EVs and profile membrane proteins efficiently (**Figs. 11f and 11h**). We concluded that charge-based EV capture by the nanowire device outperformed protein adsorption-based EV capture by the 96-well plate platform, and our nanowire device was suitable for membrane protein profiling of EVs.

b. Correlation between surface charge and membrane proteins.

To elucidate a correlation between surface charge and membrane proteins on EVs, we profiled three membrane proteins, CD9, CD63, and CD81, on EVs in the nanowire device. We evaluated effect of the purification method before introduction into the nanowire device on in-situ profiling of the membrane protein of the charge-based captured EVs. Cell-derived EVs in cell medium, without any purification and concentration processes, showed larger fluorescence intensity than those purified and concentrated by Exoquick and ultracentrifugation (**Fig. 11i**) with similar CD9/CD81 ratio, though CD63 on EVs using charge-based capture showed a little bit higher expression level than on those using conventional techniques (Exoquick and ultracentrifugation). The charge-based capture on nanowires could purify and concentrate EVs onto them from cell supernatant. Then, we profiled the expression level of membrane proteins derived from each cell, liver cancer cells (HepG2), breast cancer cells (MDA-MB-231), breast cells (HS578Bst), colon cancer cells (HCT116), and colon cells (CCD-18Co), and determined that each of the cell-derived EVs had unique expression profiles of CD9, CD63, and CD81 (**Fig. 11j**). As reported using ultracentrifugation, the concentrations of collected EVs differed among different cells and the ratio of expressed membrane protein on

EVs also differed among different cells.[61-64] Reconstruction of the data points of fluorescence intensity clarified that CD9 and CD81 would have an inherent expression level related to each cell type, and CD63 would have an inherent expression level related to EV concentrations (**Figs. 12a-12c**). A correlation of expression levels between CD9 and CD81 might be worth considering further; a high expression level of CD9 had a low expression level of CD81 and vice versa. With the ZnO nanowire device, whose use does not require any purification and concentration processes, we demonstrated the correlation between negatively-charged EV subsets obtained through surface charge-based capture and expressed membrane proteins derived from each cell. Since some reports have shown the use of EV membrane proteins in cancer and other disease diagnoses has performance superior to that of standard clinical biomarkers;[65-67] we profiled CD9 and CD147 membrane proteins, which have both been found to be highly expressed on EVs and on colon cancer related EVs, respectively.[38, 67-71] We confirmed that EVs derived from each cell type were captured on the ZnO nanowires and CD9 and CD147 membrane proteins were profiled on the EV surface (**Fig. 13a**), leading to the negatively charged EVs derived from cells being CD9 and CD147 double-positive. Specific membrane proteins on cancer cell-derived EVs seemed to be more highly enriched than those on non-cancer cell-derived EVs,[72] and the fluorescence intensity of the membrane proteins for cancer cell derived EVs was higher than that for non-cancer cell-derived EVs even though the EV concentrations were comparative (**Fig. 13b**); colon cancer cells (HCT116) > colon cells (CCD-18Co). Profiling membrane proteins of negatively charged EVs demonstrated that colon cancer cell-derived EVs had a significant difference in expression level ratio between CD9 and CD147, compared to other cancer cell-derived EVs and non-cancer cell-derived EVs (**Fig. 13b**). The breast cancer cell-derived EVs and the breast cell-derived EVs expressed both CD9 and CD147, but there was no significance difference in their expression level ratios (CD147/CD9). Since a correlation between high expression of CD147 and poor prognosis has previously been shown in colorectal cancer,[68] it makes sense that the present methodology has a potential for ex-vivo analysis of tumor-derived EVs. Finally, we introduced a urine sample from a healthy volunteer into our microfluidics device and confirmed that EVs in the urine were captured on the ZnO nanowires and CD9 and CD147 membrane proteins were profiled on the EV surface. The present nanowire device allowed us to profile membrane proteins of urinary EVs from the healthy volunteer (**Fig. 13c**). The expression level ratio (CD147/CD9) of urinary EVs from the healthy volunteer showed a significance difference, compared to colon cancer cell-derived EVs and colon cell-derived EVs; however, the expression level ratio (CD147/CD9) of urinary EVs was identical to that of breast cell-derived EVs (**Fig. 13d**). Considering the fact that the urinary EVs from the healthy volunteer include all EVs derived from all types of cells, it is

plausible that the expression level ratio (CD147/CD9) of urinary EVs is identical to that of breast cell-derived EVs and has a significance difference to that of colon cell-derived EVs. These results and previous reported data[37] imply that our methodology holds promise for application to urine-based cancer diagnosis.

2.4 Conclusions

To summarize, we have demonstrated our nanowire device could achieve membrane protein profiling of EV subsets obtained through surface charge-based capture from biological samples. The positively charged surface of the ZnO (bare) nanowires had an important role in the charge-based capture of EVs that we then used for in-situ profiling of EV membrane proteins, CD9, CD63, CD81, and CD147. The ZnO (bare) nanowires allowed us to obtain a higher expression level ratio (CD147/CD9) from colon cancer cell-derived EVs and to detect an expression level ratio (CD147/CD9) from the EVs of a healthy volunteer urine sample. Our methodology showed the potential to provide a novel indicator of the EV subset role (surface charge) for cancer diagnosis, although we need to perform further trials for the confirmation of the indicator. Since we have already identified cancer-related microRNAs from urine samples using ZnO nanowires,[37, 53] we expect it would also be possible to identify the membrane protein-based markers from urine samples after making a correlation between in-situ EV profiling and EV encapsulated microRNAs. At this point, a startup company (Craif Inc.) has already introduced a ZnO nanowire-based device to the market based on microRNA profiling, and in the future, in-situ EV profiling should come to be commercialized widely. Although we need to perform more trials for cancer diagnosis, the present results have led us to believe our developed approach will be a powerful tool that offers a new strategy for researchers to perform cancer diagnosis using urine samples.

Table 2 Comparison of capture techniques for extracellular vesicles.

Method	Time	Principle	Advantages	Disadvantages	Sample matrix
Ultracentrifugation [73, 74]	140-600 min	Size and density-based technique	Standard method; no additional chemicals needed	Damages EVs; promotes aggregation; low RNA yield	Large variety possible
Immunoaffinity [75, 76]	240 min, 12-24h incubation	Affinity-based technique	High selectivity; high purity	Difficulties with detachment of molecules	Culture medium; plasma
Filtration [77, 78]	130 min	Size-based technique	Large scale; simple operation	Filter plugging; deformation of EVs; protein contamination	Culture medium; serum; urine
Oxide nanowire microfluidics [53, 79]	20 min	Charge-based technique	Rapid and simple operation; high EV yield; high RNA throughput	Interference in complex sample matrices	Urine

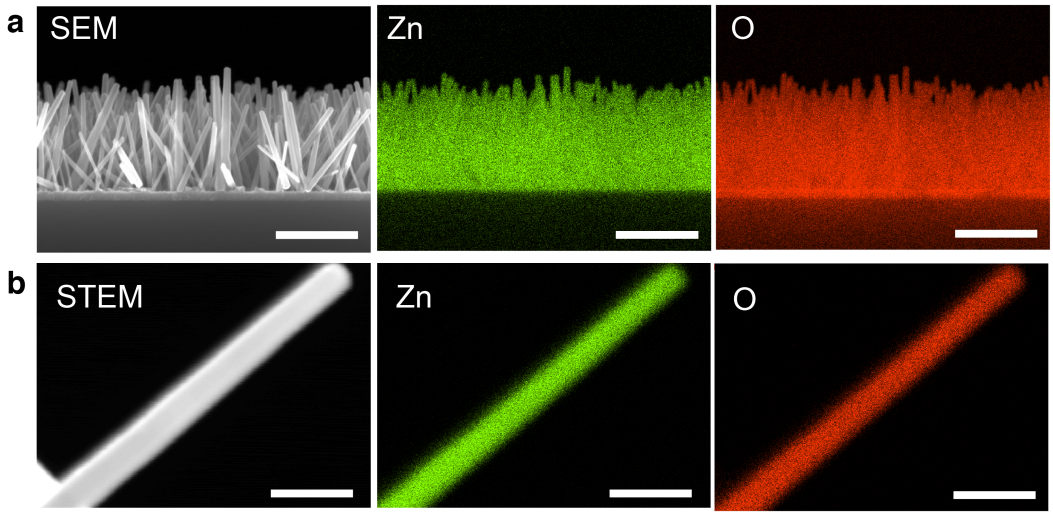

Fig. 3 FESEM images, STEM images and EDS elemental mappings of ZnO (bare) nanowires.

(a) A cross-sectional FESEM image and corresponding EDS elemental mappings of the nanowires on Si substrate; scale bars = 1 μm. Zn and O are respectively highlighted as green and red for single elemental mappings. (b) An STEM image of a nanowire and corresponding EDS elemental mappings; scale bar = 200 nm. Zn and O are respectively highlighted as green and red for single elemental mappings.

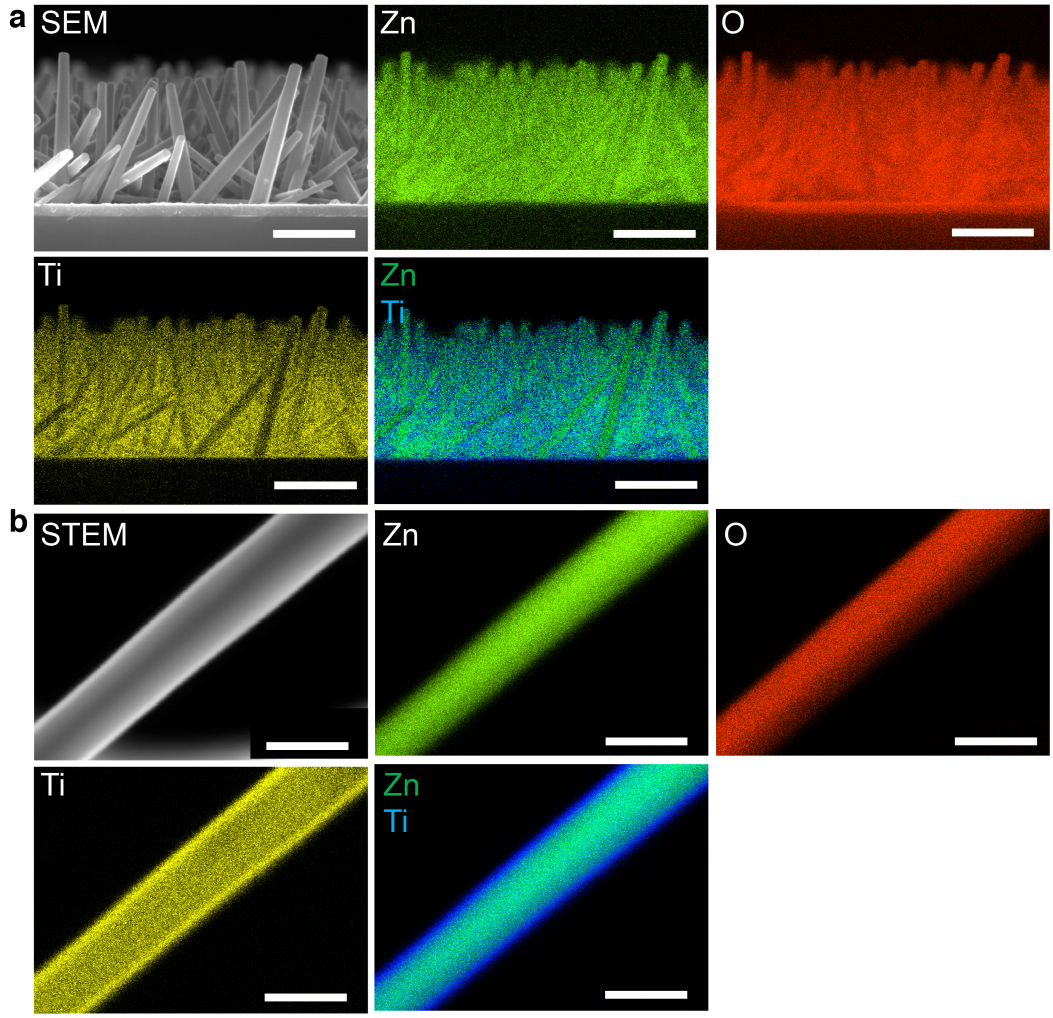

Fig. 4 FESEM images, STEM images and EDS elemental mappings of ZnO/TiO_2 (core/shell) nanowires. (a) A cross-sectional FESEM image and corresponding EDS elemental mappings of the nanowires on Si substrate; scale bars = 1 μm. Zn, O and Ti are respectively highlighted as green, red and yellow for single elemental mappings. Zn and Ti are respectively highlighted as green and blue for dual elemental mappings. (b) An STEM image of a nanowire and corresponding EDS elemental mappings; scale bar = 200 nm. Zn, O and Ti are respectively highlighted as green, red and yellow for single elemental mappings. Zn and Ti are respectively highlighted as green and blue for dual elemental mappings.

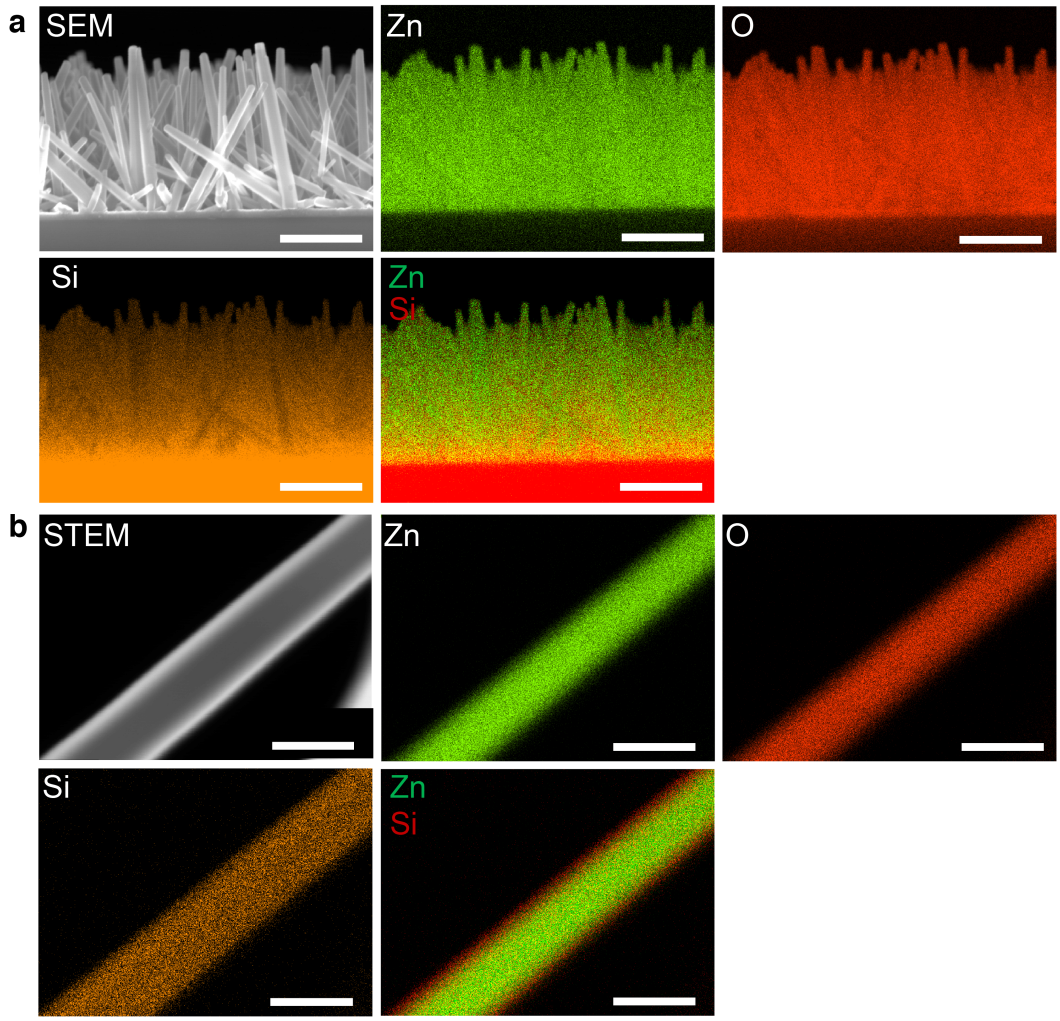

Fig. 5 FESEM images, STEM images and EDS elemental mappings of ZnO/SiO_2 (core/shell) nanowires. (a) A cross-sectional FESEM image and corresponding EDS elemental mappings of the nanowires on Si substrate; scale bars = 1 μm. Zn, O and Si are respectively highlighted as green, red and orange for single elemental mappings. Zn and Si are respectively highlighted as green and red for dual elemental mappings. (b) An STEM image of a nanowire and corresponding EDS elemental mappings; scale bar = 200 nm. Zn, O and Si are respectively highlighted as green, red and orange for single elemental mappings. Zn and Si are respectively highlighted as green and red for dual elemental mappings.

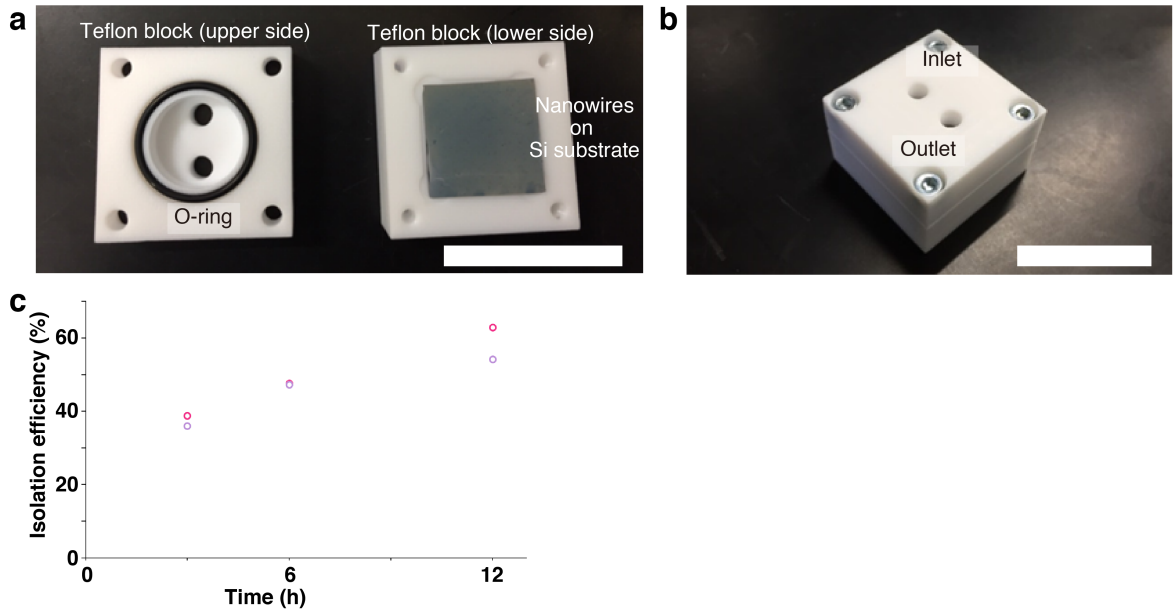

Fig. 6 EV capture using two types of nanowires.

(a) A photo of a custom-made Teflon holder before assembly; scale bar = 3 cm. The holder consists of two Teflon blocks (upper and lower sides), sandwiching an O-ring. The nanowires of different core/shell materials were grown on the Si substrate and the substrate was set on the lower side Teflon block. (b) A photo of the custom-made Teflon holder after assembly; scale bar = 3 cm. After assembly, 1 mL of EV-suspended PBS was supplied from an inlet. (c) Capture efficiency of EVs using each nanowire type (pink, ZnO (bare); purple, ZnO/ZnO core/shell) in response to capture time. The ZnO/ZnO core/shell nanowires were fabricated by depositing a ZnO layer on the ZnO nanowires by atomic layer deposition.

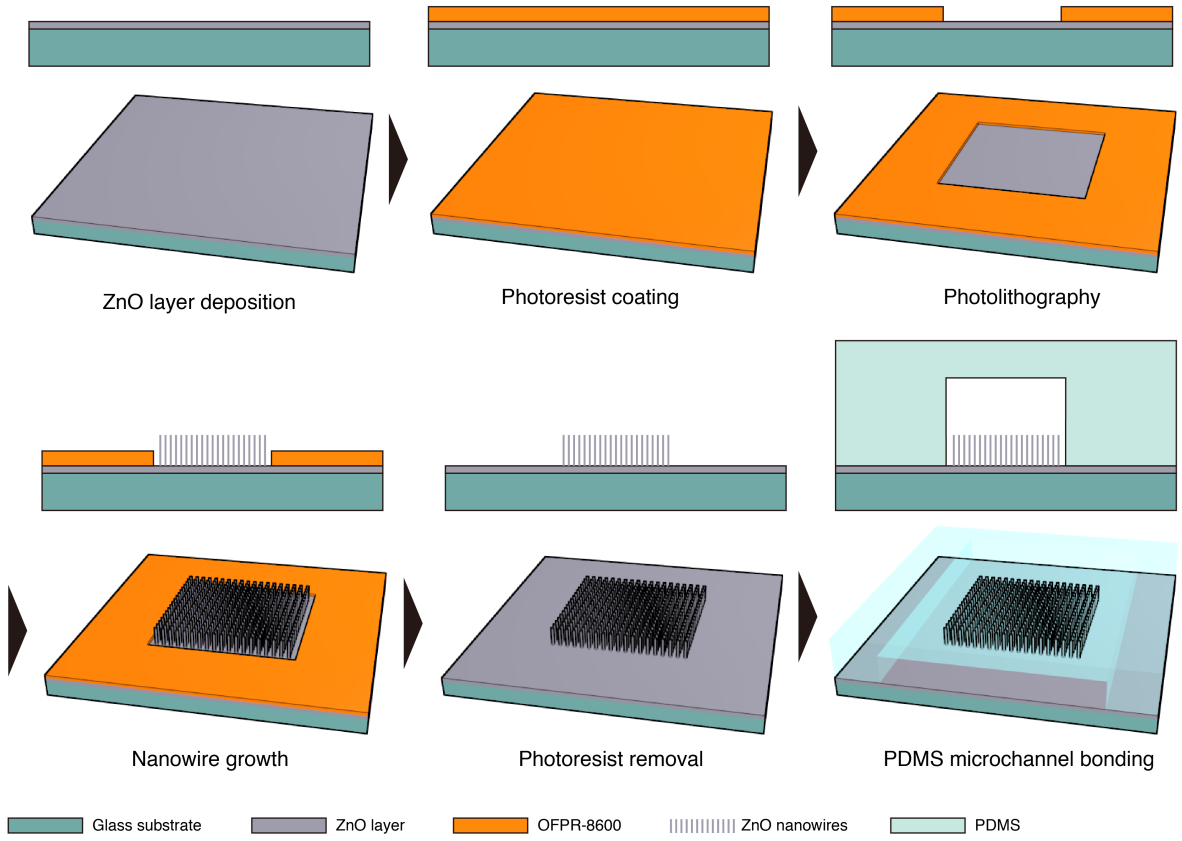

Fig. 7 Schematic drawing of the fabrication procedure for the nanowire device.

Materials included in the drawing are the glass substrate (shown as dark cyan), ZnO layer (gray), OFPR8600 photoresist (orange), ZnO nanowires (dark gray) and PDMS sheet with microchannels (faded cyan).

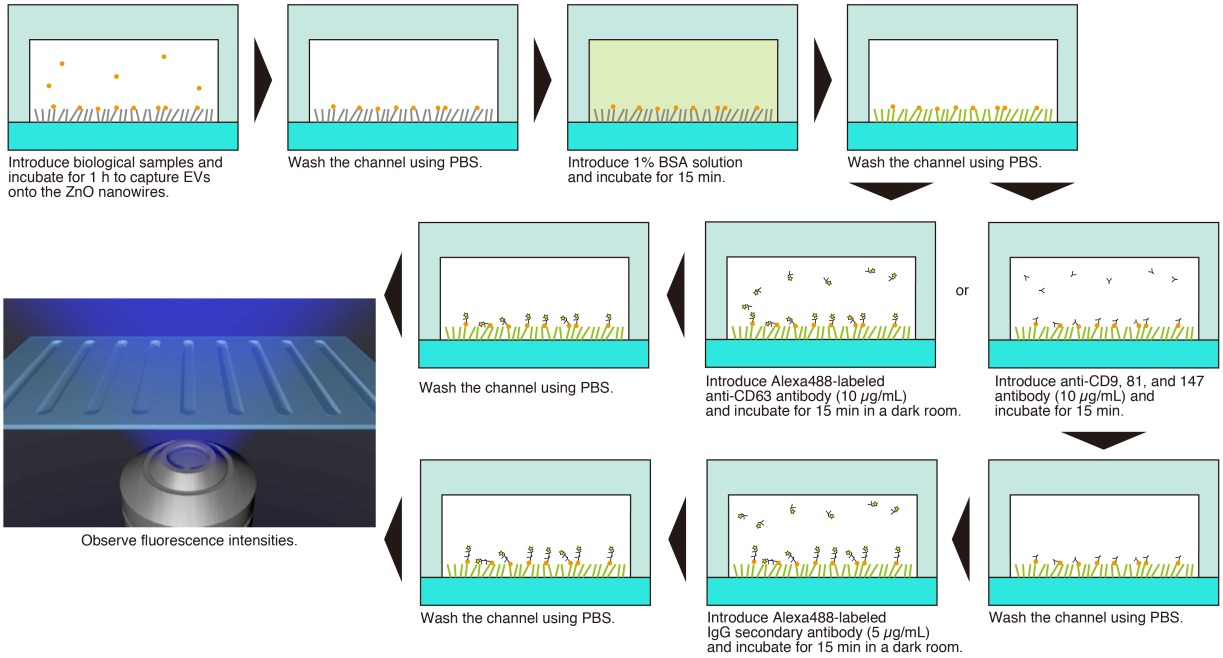

Fig. 8 Schematic drawing of the experimental procedure.

Materials included in the drawing are the glass substrate (shown as light cyan), ZnO (bare) nanowires (gray rods), PDMS sheet with microchannels (faded cyan), EVs (orange circles), BSA solution (green), antibodies (gray).

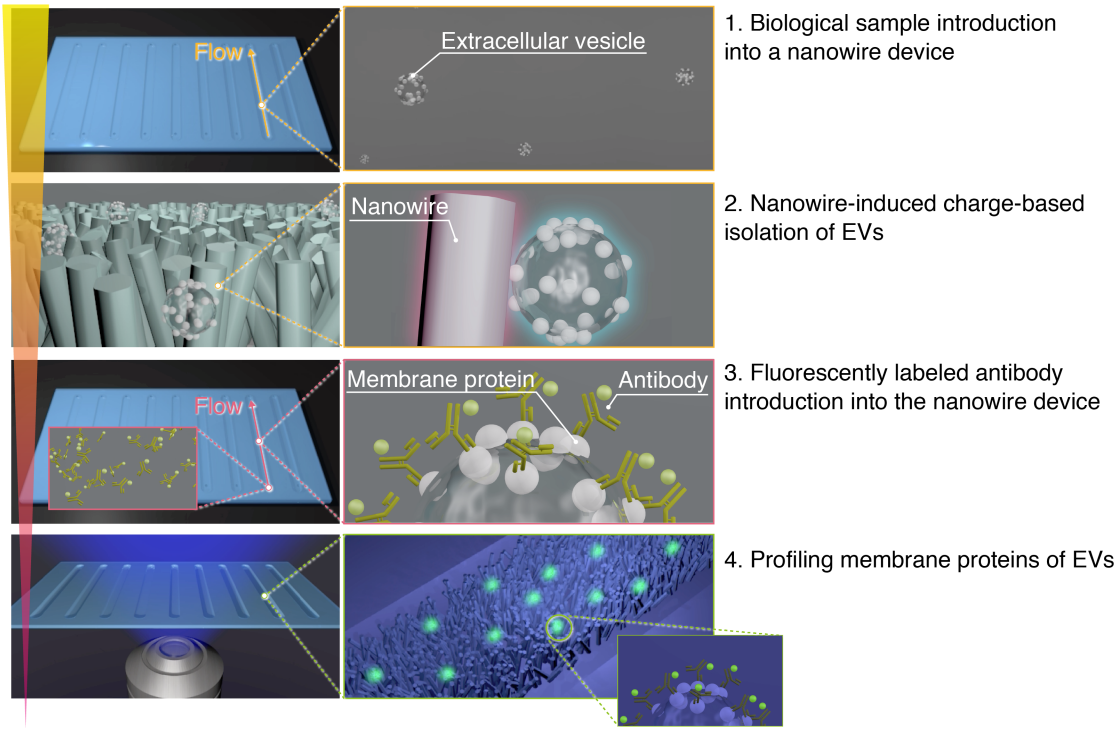

Fig. 9 Nanowire device to explore surface charge-based capture of EVs and *in-situ* profiling of EV membrane proteins.

Schematic illustrations showing steps in profiling membrane proteins via surface charge-based capture of EVs.

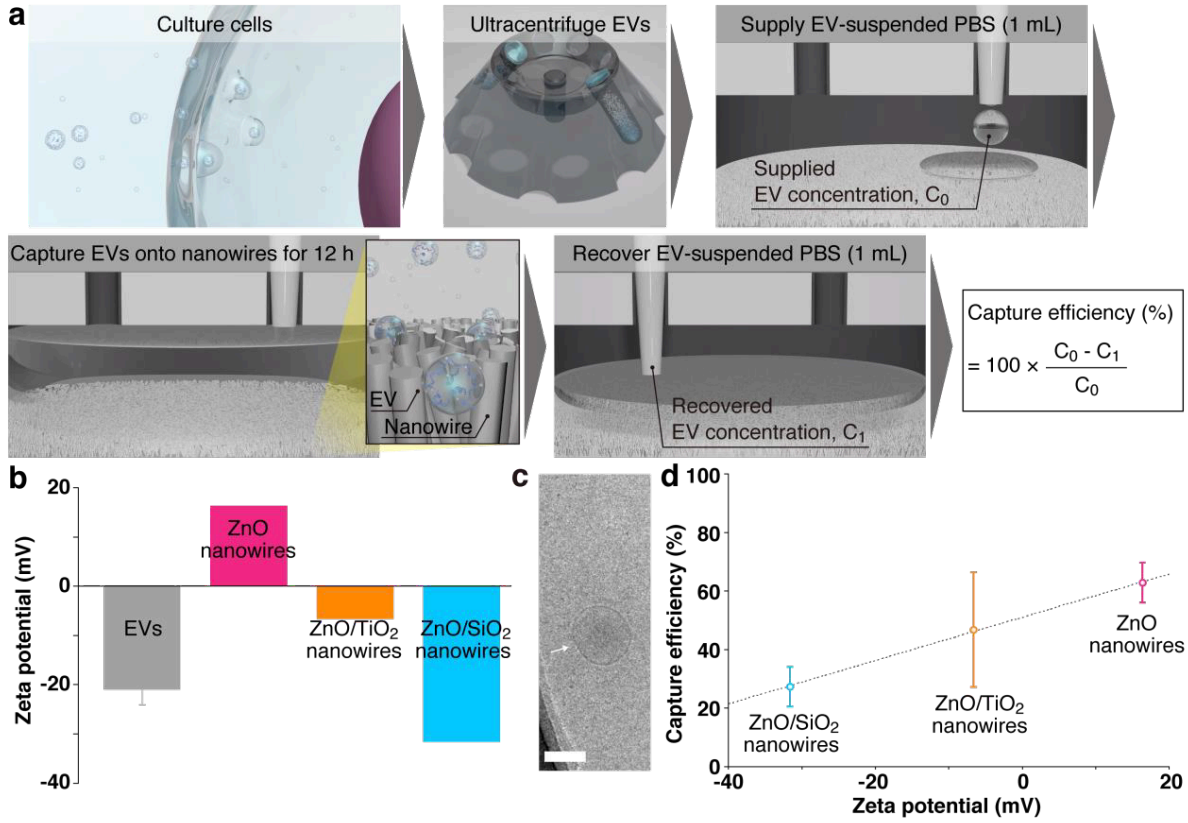

Fig. 10 Nanowire-induced charge-based capture of EVs.

(a) Schematic illustrations showing steps in calculating capture efficiency for surface charge-based capture of EVs. (b) Zeta potential of the cell-derived EVs in PBS, and ZnO (bare), ZnO/TiO_2 (core/shell) and ZnO/SiO_2 (core/shell) nanowires in water. (c) A cryo-TEM image of the cell-derived EVs; scale bar = 100 nm. The white arrow indicates the EVs. (d) Capture efficiency of EVs using different material nanowires (pink, ZnO (bare); orange, ZnO/TiO_2 (core/shell); cyan, ZnO/SiO_2 (core/shell)). Nanowires of each material on Si substrate were set into a Teflon holder to avoid any unintended adsorption onto the sample holder. Initial concentration of EVs was 1.0×10^9 (/mL). Error bars show the standard deviation for a series of measurements ($N = 3$).

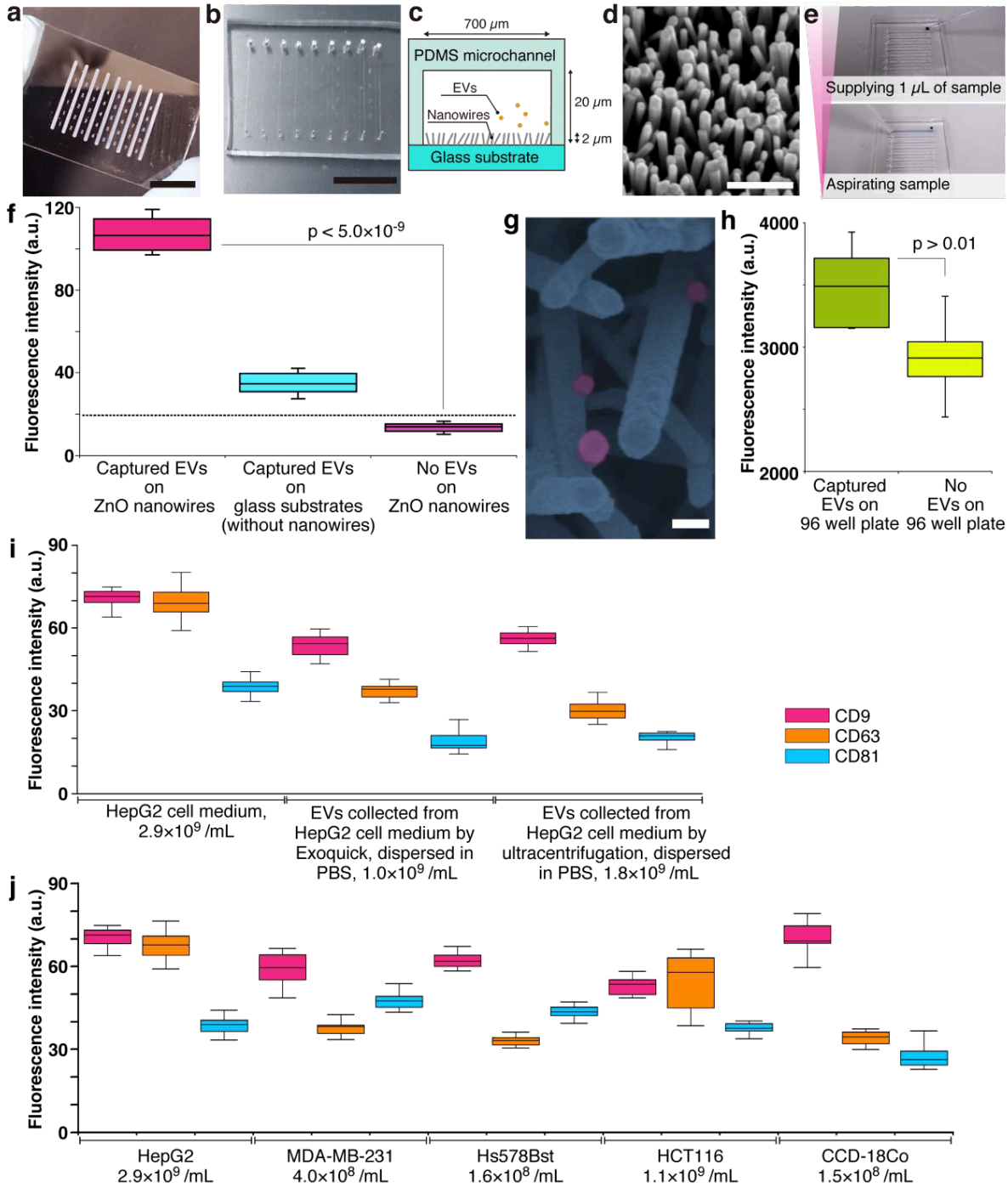

Fig. 11 In-situ profiling of charge-based captured EV membrane proteins.

(a) Photo showing the patterned area of ZnO (bare) nanowires on a glass substrate; scale bar = 10 mm. (b) A photo of a PDMS sheet with fabricated microchannels; scale bar = 10 mm. (c) A schematic cross-sectional illustration of the nanowire device. (d) An FESEM image of ZnO nanowires; scale bar = 1 μm. (e) Photos taken during experimental procedures. (f) Box and whiskers plot of CD63 membrane protein profiling of captured EVs using the microfluidic devices (pink, with ZnO nanowires; cyan, without ZnO nanowires; purple, no EVs). A measurement series was $N = 16$. Initial concentration of EVs was 1.0×10^{10} (/mL). The horizontal black

dotted line shows the signal level at 3 standard deviations above the background (3SD). (g) An FESEM image of captured EVs (colored in pink) on ZnO nanowires (colored in blue); scale bar = 100 nm. (h) Box and whiskers plot of CD63 membrane protein profiling of captured EVs using the 96 well plate (moss green, with EVs; yellow without EVs). A measurement series was $N = 6$. In (f) and (h), colored box lengths represent the interquartile range (first to third quartiles), the line in the center of each box represents the median value, the bars show the data range (maximum to minimum), and the p-value was calculated by a non-parametric test, the Mann–Whitney U test. (i) Box and whiskers plot of membrane protein profiling of captured EVs (pink, CD9; orange, CD63; cyan, CD81). EVs were purified from HepG2 cell-cultured medium by different protocols: no purification, Exoquick and ultracentrifugation. A measurement series was $N = 20$. (j) Box and whiskers plot of membrane protein profiling of captured EVs (pink, CD9; orange, CD63; cyan, CD81) in different cell-cultured medium. A measurement series was $N = 20$. In (i) and (j), colored box lengths represent the interquartile range (first to third quartiles), the line in the center of each box represents the median value, and the bars show the data range (maximum to minimum).

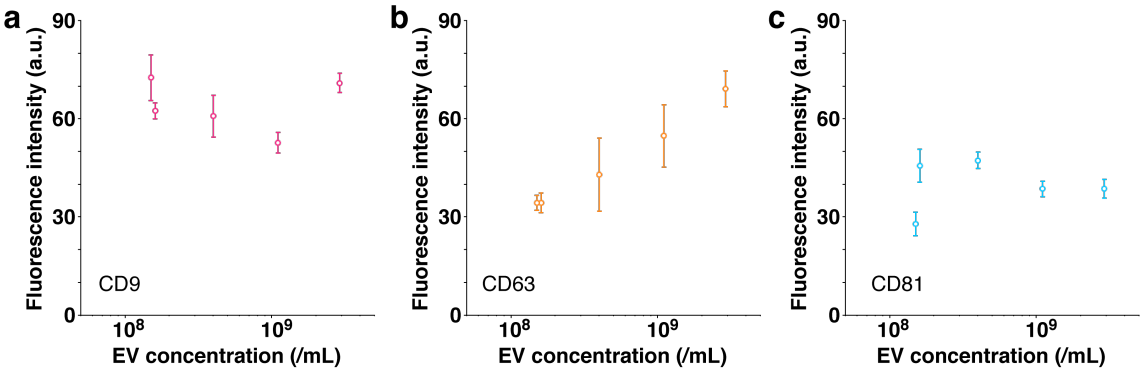

Fig. 12 Membrane protein profiling of captured EVs on ZnO (bare) nanowires.

(a-c) Plots of fluorescence intensity for (a) CD9, (b) CD63, and (c) CD81 membrane proteins vs. EV concentration. Different cell-derived EVs were used (Fig. 11j). Error bars show the standard deviation for a measurement series ($N = 20$).

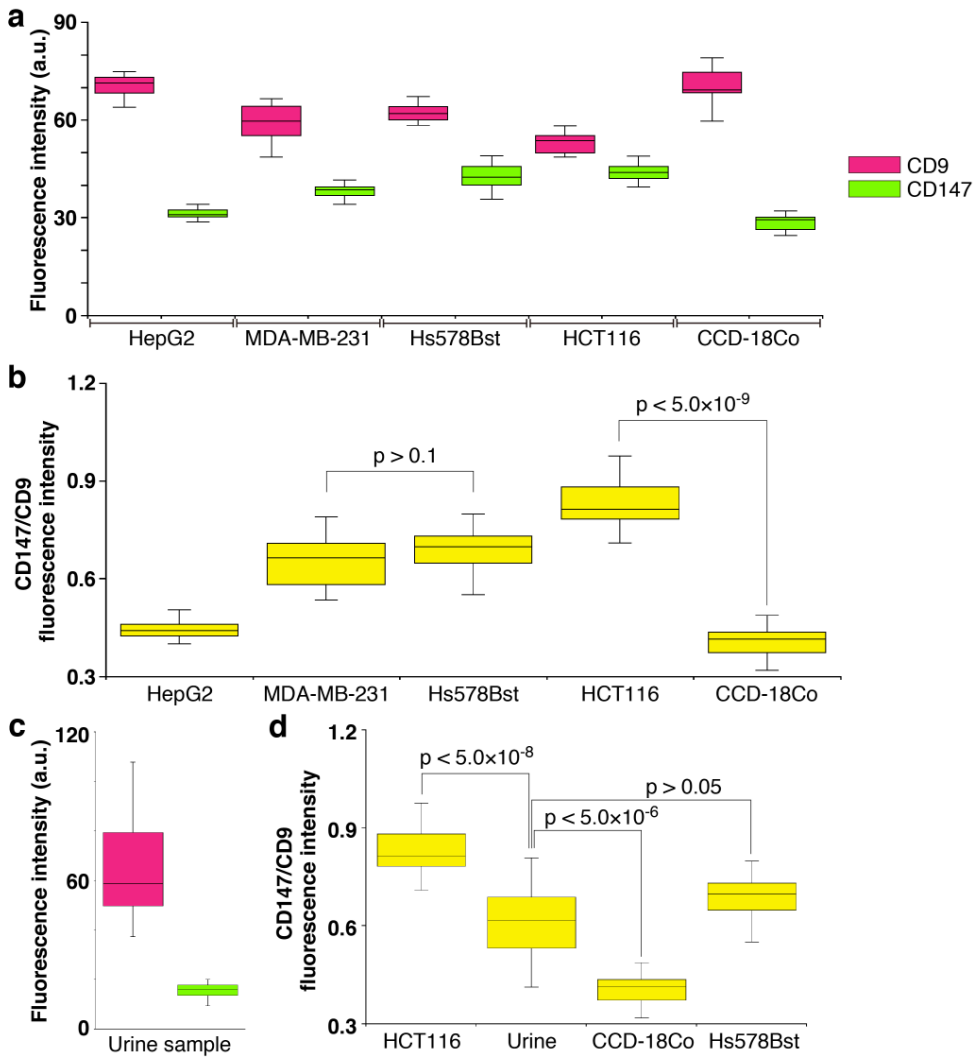

Fig. 13 Membrane protein, CD9 and CD147, profiling of EVs.

(a) Box and whiskers plot of membrane protein profiling of captured EVs (pink, CD9; light green, CD147) in different cell-cultured medium. A measurement series was *N = 16*. (b) Box and whiskers plot of the ratio of CD147 fluorescence intensity to CD9 fluorescence intensity. The p-value was calculated by a nonparametric test, the Mann–Whitney U test. (c) Box and whiskers plot of membrane protein profiling of captured EVs (pink, CD9; light green, CD147) in urine. A measurement series was *N = 20*. (d) Box and whiskers plot of the ratio of CD147 fluorescence intensity to CD9 fluorescence intensity. The p-value was calculated by a non-parametric test, the Mann–Whitney U test. In (a-d), colored box lengths represent the interquartile range (first to third quartiles), the line in the center of each box represents the median value, and the bars show the data range (maximum to minimum).

Chapter 3. Tailoring ZnO Nanowire Crystallinity and Morphology for Label-Free Capturing of Extracellular Vesicles

3.1 Introduction

Zinc oxide (ZnO) nanowires have shown their potential in isolation of cancer-related biomolecules such as extracellular vesicles (EVs), RNAs, and DNAs for early diagnosis and therapeutic development of diseases. Since the function of inorganic nanowires changes depending on their morphology, previous studies have established strategies to control the morphology and have demonstrated attainment of improved properties for gas and organic compound detection, and for dye-sensitized solar cells and photoelectric conversion performance. Nevertheless, crystallinity and morphology of ZnO nanowires for capturing EVs, an important biomarker of cancer, have not yet been discussed. Here, we fabricated ZnO nanowires with different crystallinities and morphologies using an ammonia-assisted hydrothermal method, and we comprehensively analyzed the crystalline nature and oriented growth of the synthesized nanowires by X-ray diffraction and selected area electron diffraction using high resolution transmission electron microscopy. In evaluating the performance of label-free EV capture in a microfluidic device platform, we found both the crystallinity and morphology of ZnO nanowires affected EV capture efficiency. In particular, the zinc blende phase was identified as important for crystallinity, while increasing the nanowire density in the array was important for morphology to improve EV capture performance. These results highlighted that the key physicochemical properties of the ZnO nanowires were related to the EV capture performance.

At the nanoscale, device properties and performance are no longer dependent solely on the material type, but also on material geometry. Nanowires, anisotropic structures with diameters from one to hundreds of nanometers and lengths of tens to hundreds of microns, provide a unique platform for harnessing nanoscale phenomena.[80] Semiconductor nanowires are a broad class of materials which, through controlled growth and organization, have led to a number of novel nanoscale mechanical, electrochemical, thermoelectric, photonic and electronic devices.[81-83] In order to produce and utilize these properties for nanowires, reliable and controllable nanowire syntheses are required. A hydrothermal method offers flexible control over nanowire crystal structure and growth orientation, enabling fabrication of high-quality single-crystalline materials with control of diameter, length, composition, and phase.[84] When ZnO nanowires are hydrothermally synthesized, they are single crystals, and as a result of their narrow diameter, the nanowires have an extremely high surface area allowing highly sensitive interaction with various substances.[85-88] This high surface-to-volume ratio makes

the nanowires very sensitive to changes in surface chemistry and permits rapid interaction with comparatively small sizes of biomolecules including extracellular vesicles (EVs) and nucleic acids giving rise to their prevalence in isolation and detection technology development.[37, 89-93]

The physical phenomena in the radial and axial directions and the high surface-to-volume ratios of the nanowires have been controlled and that has led to an explosion of applications utilizing these structures. Getting preferential nucleation at the ZnO (0001) polar plane and suppressing the lateral growth, such as of the (1010) plane, are key essentials to produce a well-defined nanowire structure.[94-96] Many growth parameters have been explored to manipulate the morphology of hydrothermally synthesized ZnO nanowires including the addition of auxiliary agents such as organic ligands, metal ion impurities and ammonia ions.[58, 97-101] The solution-grown ZnO nanowires generally adopt the wurtzite crystal structure and grow along the *c* axis with a (0002) top facet and (1010) side facets. At pH = 11 basic conditions, it was found that the top facet is negatively charge and the side facets are positively charged, enabling control of the nanowire dimensions based on the facet-selective electrostatic interaction;[102] and therefore, the radial growth of colloidal nanowires can be effectively suppressed. In other words, control of the nanowire mean length and diameter can be achieved by optimizing the concentration of ammonia ions, for example. Several studies have investigated physicochemical properties of the developed high aspect ratio ZnO nanowires in various applications including photocatalysis, a piezoelectric transducer, a UV detector, photovoltaic devices, and gas and chemical sensors.[103-108] To the best of our knowledge, the correlation of ZnO nanowires in terms of crystal structure and morphology with biomolecule capture has not been discussed until now.

Here, we propose a methodology using oxide nanowires with different crystallinities and morphologies synthesized by ammonia-assisted hydrothermal growth to evaluate capture performance of extracellular vesicles (EVs) and we investigate a correlation between surface crystallinity and numbers of the captured EVs. The EVs are nano- to micro-sized vesicles secreted from all cells, including cancer cells, and they are released into their environment to act as intercellular messengers.[12, 109, 110] Since they enclose components from the parent cells, including nucleic acids and proteins, EVs are being examined as sources of biomarkers in various diseases, including neurodegenerative diseases, cardiovascular diseases and cancers.[111-114] EVs are also being explored for the delivery of therapeutic payloads to specific cells or tissues in cancer therapeutics,[115, 116] owing to their distinct biological features. The enrichment of these proteoglycans has led to the idea that EVs are charged molecules.[52, 117] We have initiated studies exploiting ZnO nanowire integrated microfluidic devices for label-free capture of EVs through surface charge-based capture which can collect massive numbers of EVs and

their molecular cargos.[37, 92] However, comprehensive studies of nanowires with a diverse crystal structure and morphology system have not been made yet.

3.2 Method

a. Synthesis of ZnO nanowires.

We fabricated ZnO nanowires on Si substrates via a seed-assisted hydrothermal process. First, double-microchannel patterns (20 × 2 mm^2) were formed by photolithography onto each Si (100) substrate and a 20 nm thick seed layer was deposited with an electron cyclotron resonance (ECR) sputtering system (Elionix, EIS-200ERT-YN). High melting-point Cr-based alloy with purity of 99.999% was used as a sputtering target. The substrates with seed layer were oxidized in an oven at 400°C for 2 h to prepare them as a scaffold for the ZnO nanowires. After seed layer preparation on substrate, the nanowire growth solutions were prepared using 15 mM hexamethylenetetramine (HMTA) and 15 mM zinc nitrate hexahydrate ($Zn(NO_3)_2.6H_2O$) as the precursors, and 0.8 M ammonium solution was added for ultra-lengthening of ZnO nanowires. The nanowires were grown at 95°C with varying duration times (3 h, 6 h and 9 h). We renewed the growth solutions every 3 h to maintain the concentrations.

b. Fabrication of the microfluidic device.

The dried nanowires grown on the substrate were treated with oxygen plasma. A sheet of 30-μm-depth Polydimethylsiloxane (PDMS) was attached to the substrate. The sheet was patterned with two microchannels (20 × 2 mm^2) and 0.05 mm inlet and outlet holes at the end of channels for sample injection.

c. Characterization of ZnO nanowires.

The morphology and the composition of ZnO nanowires were characterized with a field emission scanning electron microscope (FESEM; Carl Zeiss, Supra 40VP), a high-resolution transmission electron microscope (HRTEM; JEOL, JEM-2100) and an energy dispersive X-ray spectroscopy (EDS) system (Oxford Instruments, Ultim Max 100). For the cross-sectional SEM-EDS analysis and the single-nanowire HRTEM analysis, we utilized an accelerating voltage of 15 kV and 200 kV, respectively. The EDS mapping images were integrated for 100 cycles. The peaks of Zn Kα (8.6313 keV), O Kα (0.5249 keV), Si Kα (1.7398 keV), and Cr Kα (5.4117 keV) and were chosen to construct the elemental mapping images. An X-ray diffraction (XRD) analyzer (Bruker, D8 Advance) was used to examine the crystalline nature and oriented growth of synthesized ZnO nanowires. The conditions were set to be Cu Kα XRD source, λ = 0.1542 nm, accelerating voltage of 40 kV,

acceleration current 40 mA, scan step 0.02 deg, scan rate 0.5 s/step, and scan range 20 to 80 deg. The XRD patterns were analyzed using Diffrac.EVA 5.0 software.

d. Cell culture and extraction of EV by ultracentrifugation.

We cultured human breast adenocarcinoma cells (MDA-MB-231) in DMEM supplemented with 10% exosome-depleted FBS and 1% penicillin streptomycin. The concentration of 2×10^6 cells were seeded into 15 mL of complete medium in a 75 cm^2 culturing flask and incubated at 37ºC and with 5% CO_2. After 48 h, the cell medium was taken from the culturing flask and filtered through a 0.22-μm filter to remove cellular debris. Next, the filtered medium was ultracentrifuged at 110,000 *g*, 4°C, 80 min. After discarding the supernatant, we added 5 mL of 0.22-μm filtered PBS to wash the EV pellets, and this solution was ultracentrifuged again with the same conditions. After discarding the supernatant, 1 mL of 0.22-μm filtered PBS was added to collect EVs. The EV suspension was stored at 4ºC until use.

e. Evaluation of EV capture efficiency.

We integrated a nanowire device with a dual-channel syringe pump to continuously infuse EV sample with the flow rate of 10 μL/min. The volume of 250 μL of EV-suspended PBS was supplied to the nanowire device to isolate EVs onto each nanowire. EV numbers and size distribution were analyzed using a nanoparticle tracking analysis (NTA) system (Malvern Panalytical, NanoSight LM10). After appropriate dilutions, video data were collected 5 times for a 60-s time period for each video. Camera level and detection threshold were set to 13 and 5, respectively. Data analysis was performed automatically by NanoSight NTA 3.2 software. To observe EVs on nanowire surfaces, the device was left to dry naturally at room temperature. The PDMS sheet was removed from the substrate, the captured EVs on the nanowire surfaces were directly observed using FESEM at 5 kV of accelerating voltage without any fixation or coating processes.

3.3 Results and Discussion

a. Morphology dependence of fabricated ZnO nanowires.

For controlling the morphology of ZnO nanowires, we introduced ammonia solution into the ZnO precursor growth solution during the growth step and hydrothermally fabricated nanowires in varying growth duration times for 3, 6, and 9 h. Ammonium hydroxide is an additive that has been widely used to enhance the nanowire growth rate along the *c*-axial ZnO plane via face-selective electrostatic crystal growth inhibition.[102] As ammonia concentration was reported to critically affect the morphology of nanowires,[57, 103, 118] we evaluated the optimum concentration of ammonia for our experimental conditions and found the concentration of ammonia at 0.8 M provided the longest nanowires (**Fig. 14**). The pH values in growth solutions with ammonia addition (**Fig. 15**) indicated the presence of OH^- ions during the time before nanowire growth (initial) to after it (final). Morphology observations showed that the nanowires obtained were larger in length and diameter in comparison to nanowires grown without ammonia addition, and nanowire length could be enlarged by increasing the growth duration time (**Fig. 16**). The EDS mapping images of Zn Kα as a main constituent of the synthesized nanowires confirmed that various lengths of ZnO nanowires could be obtained by using the ammonia-assisted hydrothermal fabrication method (**Figs. 16c** and **17**).

To clearly reflect the effect of ammonia in controlling the morphology of nanowires, we examined the length, diameter, aspect ratio and density of the synthesized nanowires as a function of growth duration times (**Fig. 18**). Both length and diameter increased with increasing growth time (**Figs. 18a** and **18b**), especially, for the 3 h growth time, the addition of NH_3 lead to nanowires about 5-fold longer than those grown without NH_3 in the reaction mixture. Also, the nanowire lengths with ammonia addition increased with time in a linear manner; however, the nanowires grown for 9 h clearly tended to have a large diameter, indicating the occurrence of the (1010) radial plane growth. In addition, we noticed that the nanowires grown for 6 h with NH_3 addition had the highest aspect ratio of over 55, calculated from the ratio of length to diameter, after which the ratio decreased (**Fig. 18c**). Furthermore, the density of ZnO nanowires decreased with increasing the growth time due to the lateral growth effect and the competition among nanowires (**Figs. 18d** and **19**). Although the precursor supply for the ZnO nanowire growth was replenished with fresh solution to maintain the concentration and growth rate, the diameter of the nanowires still continued to increase and they were expected to eventually attach together to form a ZnO film.[119] When the nanowires grow longer in random directions, only a few wires with a high growth rate will sustainably grow because nanowires with their orientation close to the substrate will be restricted by neighboring nanowires.[96, 120] These results indicated the significant role of ammonia and

the effect of growth time on the nanowire morphology: the length and diameter of the nanowires increased with increasing growth time but the aspect ratio and density decreased.

b. Crystal structure analysis by XRD and SAED.

Since the morphological changes to the nanowires are expected to have a significant effect on the crystal structure of the nanowires, we next examined the crystallinity of the nanowires with different morphologies synthesized under each growth condition. Normalized XRD spectra showed the single crystallinity of these nanowires; however different preferential orientations were observed (**Fig. 20a**). The three main characteristic peaks (100), (002), (101) of wurtzite ZnO phase in the 2θ = 31° to 37° range demonstrated alterations of the dominant ZnO-related peak for each condition (**Fig. 20b** and **Table 3**). When ammonia was added for the 3 h growth time, the ZnO nanowires started to grow preferentially in the orientation (101) higher than (002), in contrast, the dominant peak shifted back to (002) direction at 6 h and 9 h with NH_3 addition, and the highest intensity (002) peak was observed at 6 h with NH_3 addition (**Fig. 20c**). Besides, the ZnO (004) peak which is the characteristic peak of the cubic zinc blende phase[121, 122] was observed at 6 h and 9 h with NH_3 addition (**Fig. 20d**). This was attributed to the fact that the synthesis of ZnO nanostructures under a thermodynamic condition generally results in the wurtzite structure since the wurtzite phase is thermodynamically more stable than the zinc blende phase.[123] However, compared with the wurtzite ZnO phase, zinc blende ZnO has lower ionicity and higher crystallographic symmetry, and zinc blende ZnO is expected to have higher carrier mobility and electrical gain.[121] The presence of different phases in the nanowires may play a role in the capture of EVs by these nanowires, because the chemical and physical properties of nanowires are expected to be significantly influenced by their crystal structure. The above results clearly showed that the effect of ammonia occurred not only on the morphology of the ZnO nanowires but also on their crystallinity, especially in the growth rate of ZnO nanowires in the vertical c-axis direction, where the NH_3 addition for 6 h had the highest growth rate.

The differences in local crystallinity caused by the nanowire morphological change in the upper, middle, and lower regions were investigated (**Fig. 21**), because the nanowires grown with NH_3 additions were found to have a needle-like shape, with the upper part of the nanowires being sharper and smaller in diameter than the lower part. Electron diffraction patterns indicated that the structures of ZnO nanowires with different morphologies synthesized under each growth condition were a single crystal. In case of 3 h growth without NH_3 addition, the nanowires grow mainly only along the (0002) direction without any significant lateral sidewall growth for all positions. For the 3 h growth with NH_3 addition, the nanowires tended to have varying diameters from upper to lower parts but the selective area electron diffraction (SAED) measurements yielded

consistent diffraction patterns. Distinct patterns among the nanowire regions were identified for the cases of 6 and 9 h growth with NH_3 addition. At the short 3 h growth time, the wurtzite growth mode was dominant; whereas, the larger diameter nanowires grown with longer reaction times (6 h and 9 h) had a zinc blende crystal structure. In other words, a transition to the zinc blende growth mode occurred at longer times. We investigated the inter planar spacing and diffraction planes from XRD and HRTEM for further understanding of the crystal structure of the nanowires (**Table 4**).

The above results highlighted that the growth time with NH_3 addition not only affected the lateral diameter but also the growth direction and crystal plane. The anisotropic growth structure of the nanowires is caused by the highest growth rate occurring along the *c*-axis, which has a high surface energy but a small area leading to the wire-like structures.[124] A possible explanation for the wurtzite phase in the nanowires is that side walls of wurtzite have a lower surface energy than the zinc blende nanowires,[125-127] and the successful phase transition we achieved was attributed to alterations in nanowire surface energy at different growth conditions with NH_3 addition (**Fig. 22a**). Although the difference in atomic arrangement on a nanoscale is subtle, it is expected to cause a large difference in the physical and chemical properties of the nanomaterials, such as their EV capture efficiency.[128, 129] We anticipated that the preferential capture of the negatively charged EVs[92, 117, 130] onto the positively charged surfaces with different crystal planes of ZnO nanowires would lead to the higher EV capture efficiency.

c. Evaluation of EV capture performance.

Finally, we demonstrated the effect on EV capture capability for ZnO nanowires fabricated by the ammonia-assisted hydrothermal growth. To do this, we integrated nanowires with PDMS microchannels to fabricate a nanowire microfluidic device (**Fig. 23a**). The experimental setup of a double-channel nanowire microfluidic device connected with an automatically continuous flow syringe pump supplied EVs into the device (**Fig. 24**). The nanowires grown with NH_3 additions resulted in the efficacy of EV capture being increased. Furthermore, the nanowires grown for 6 h, with the highest aspect ratio, achieved the highest performance of 68% after which the efficacy dropped at 9 h (**Figs. 23b** and **23c**). The FESEM images visualizing EVs on the ZnO nanowire surface after the EV capture experiment showed that EVs were directly captured along the nanowire surface (**Fig. 23e**). We attributed the efficacy enhancement to the fact that nanowires which were long in the vertical could interact with each EV species; however, the capture rate did not increase monotonically within this regime. This was due to the decreased density of nanowires (**Fig. 18d**), which resulted in fewer possibilities for capture events of EVs onto nanowire surfaces.

In addition to the change in EV capture efficiency due to nanowire morphological changes, we also found a change in EV capture efficiency due to changes in nanowire crystallinity. The nanowires grown with NH_3 addition for 9 h showed the lowest capture efficiency due to the low density of the nanowires, but the contribution of a single nanowire to EV capture was qualitatively found to be the highest (**Fig. 23d**), indicating that changes in the crystallinity of the nanowires were also important. To confirm the effect of the nanowire crystallinity on EV capture, we prepared ZnO nanowires of wurtzite ZnO phase with the same morphology by annealing the nanowires at 500 ºC for 2 h[131-133] after nanowire growth since this annealing process is known to cause the phase transition from zinc blende to wurtzite (**Fig. 22b** and **Table 3**). The nanowires grown with NH_3 addition for 6 h followed by the annealing process exhibited lower EV capture efficiency than those grown without the annealing process (**Figs. 23b** and **23c**). And also, the contribution of a single nanowire to EV capture showed that annealing process significantly decreased the number of captured EVs on a single nanowire, and then the zinc blende phase increased the number of captured EVs on a single nanowire (**Fig. 23d**). Our results highlighted that designing and controlling the crystal structure of ZnO nanowires could be achieved by using NH_3 addition to enhance the capability for label-free capture of EVs via the variations of their electrostatic interactions with the ZnO crystal plane. However, NH_3 addition and the growth time also affected the morphology of nanowires leading to lower efficiency as the nanowires being larger in diameter and lower in density. Further studies are needed in order to achieve the optimum crystal structure and morphologies of nanowires for a specific application.

3.4 Conclusions

This is the first study to identify the effects of crystallinity and morphology of ZnO nanowires grown hydrothermally with NH_3 addition on their electrostatic properties for label-free EV capturing. As found from results of the XRD and HRTEM analyeses, the crystal structures of all samples had the main characteristics of the ZnO wurtzite phase, but they were also mixed with zinc blende phase when grown under some conditions, making them suitable for EV capture on the nanowires. Considering the crystallinity and the morphology of the nanowires, the nanowires grown for 6 h with NH_3 addition offered the highest EV capture performance due to the presence of zinc blende phase and high density of the nanowires. These findings are expected to facilitate the realization of tunable nanowires with high potential suitability for integration into advanced label-free EV capture devices which will open up opportunities for further fundamental studies (*i.e.*, adsorption mechanisms by biomolecules) and alternative applications in high-performance integrated nanowire devices.

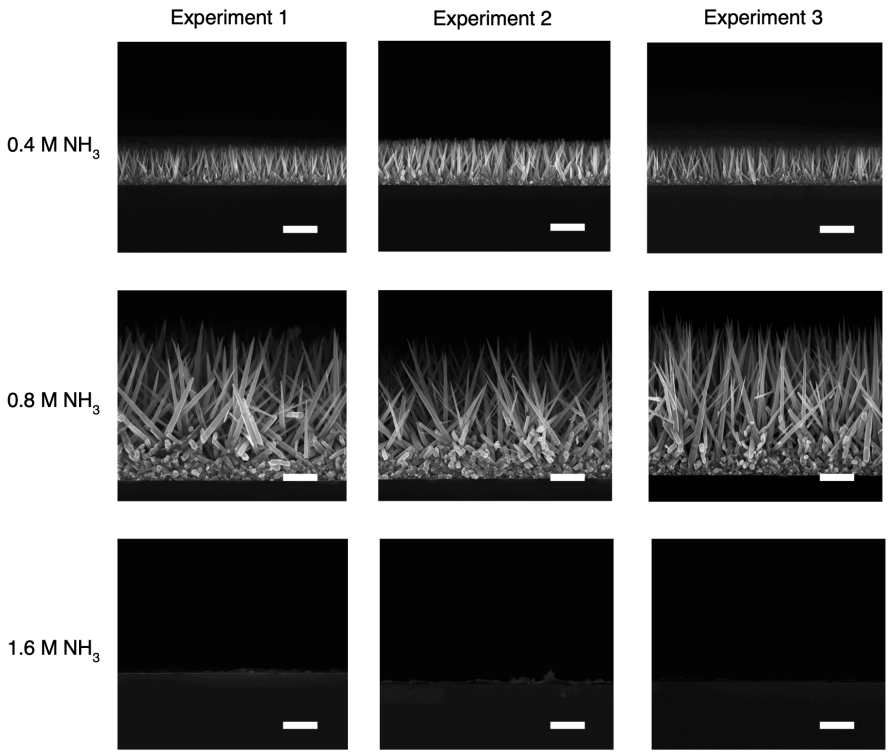

Fig. 14 The optimization of ammonia concentration.

FESEM characterization of ammonia concentration dependence of ZnO nanowires (0.4, 0.8, and 1.6 M). The scale bars are 2 μm. The concentration of ZnO precursors was fixed at 15 mM. The ammonium concentration at 0.8 M resulted in the longest nanowires and its use is promising for promoting ZnO nanowire growth in the designed patterning area.

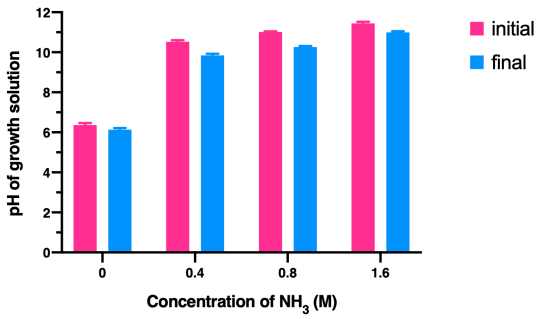

Fig. 15 The pH of growth solution.

The pH values in growth solutions that resulted from ammonia addition indicated the presence of OH^- ions during the time before nanowire growth (initial) to after it (final). The error bars are defined by standard deviation values (N = 3). The slight changes of pH after the 3 h hydrothermal reaction that were observed resulted from the consumption of OH^- ions and some evaporation.

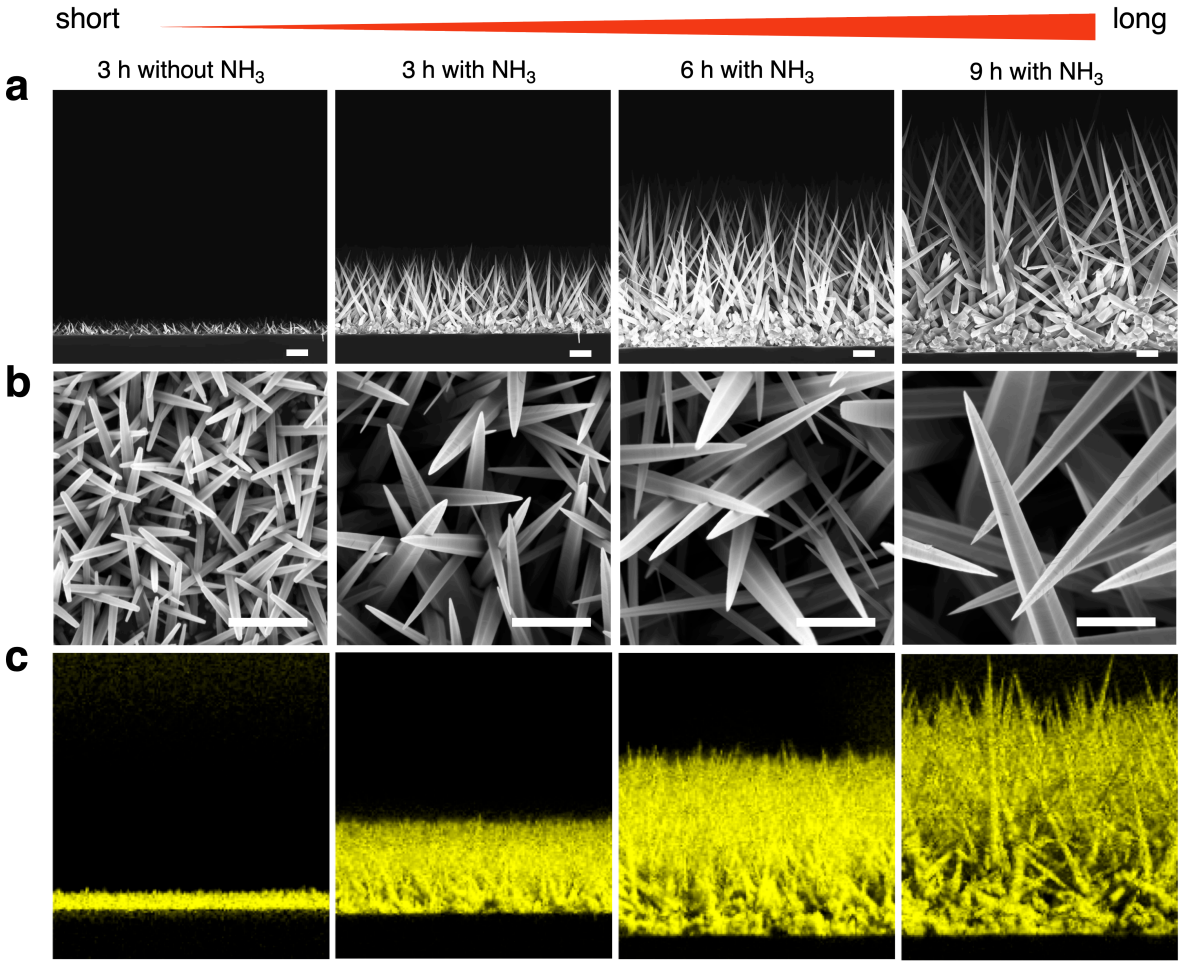

Fig. 16 The characterization of nanowire morphology and composition.

(a) FESEM images of cross-sectional nanowires for different growth conditions. The scale bars are 2 μm. (b) FESEM images of top-view nanowires. The scale bars are 1 μm. (c) Elemental mapping of Zn Kα (8.6313 keV) highlighted in yellow, as a main constituent of the nanowires.

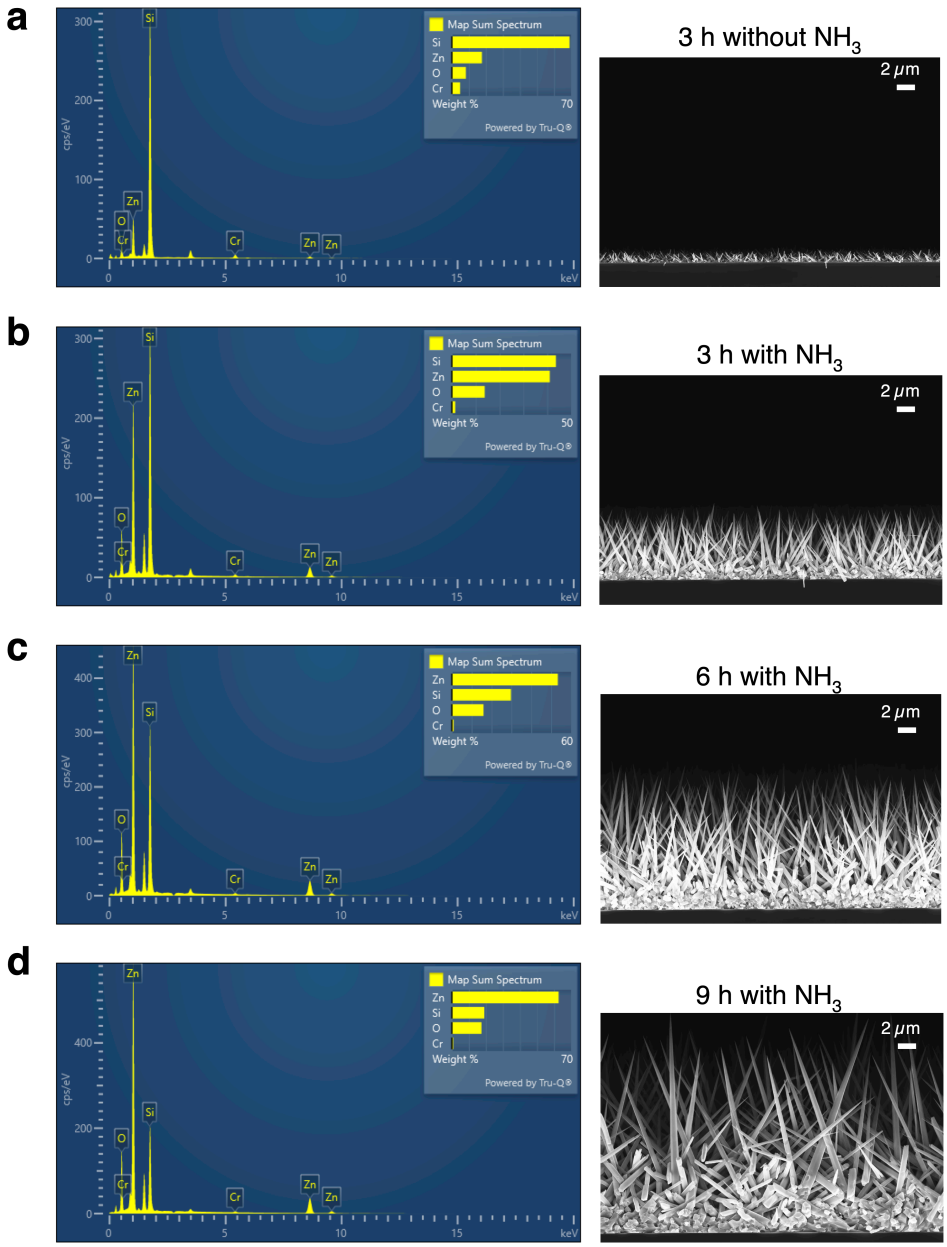

Fig. 17 Composition analysis of nanowires.

(a-e) The top-viewed FESEM images of ZnO nanowires from three different regions of each condition (3 h without NH_3, 3 h, 6 h, and 9 h reactions with NH_3 and annealed 6 h with NH_3, respectively). The scale bars are 1 μm.

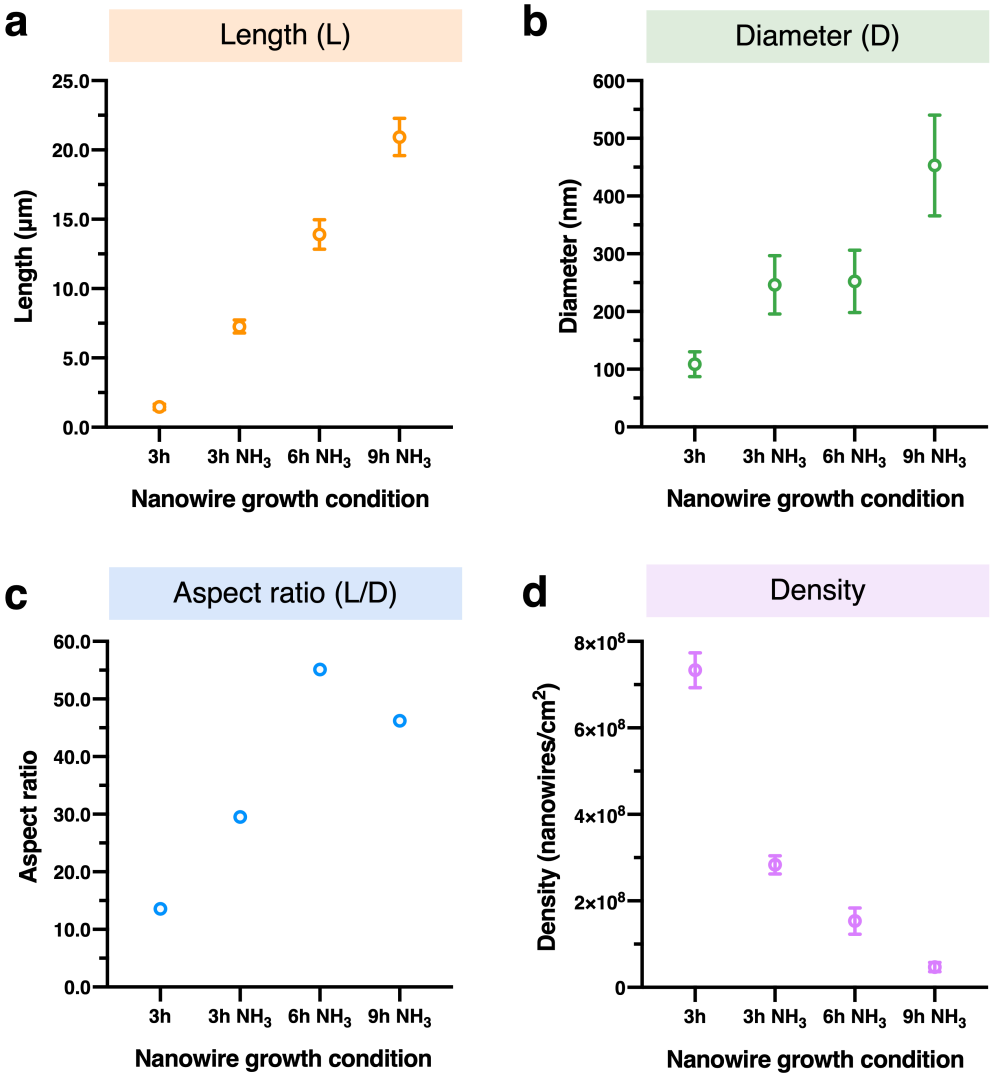

Fig. 18 The dependence of the morphology of ZnO nanowires on four nanowire characteristics.

(a) Statistic length and (b) diameter of nanowires. The error bars are defined by standard deviation values (*N = 100*). (c) Aspect ratio (length/diameter) of nanowires. (d) Density of nanowires calculated by counting the tips of nanowires in a known area. The error bars are defined by standard deviation values (*N = 486, 187, 103, 31* counted nanowires at each condition, respectively).

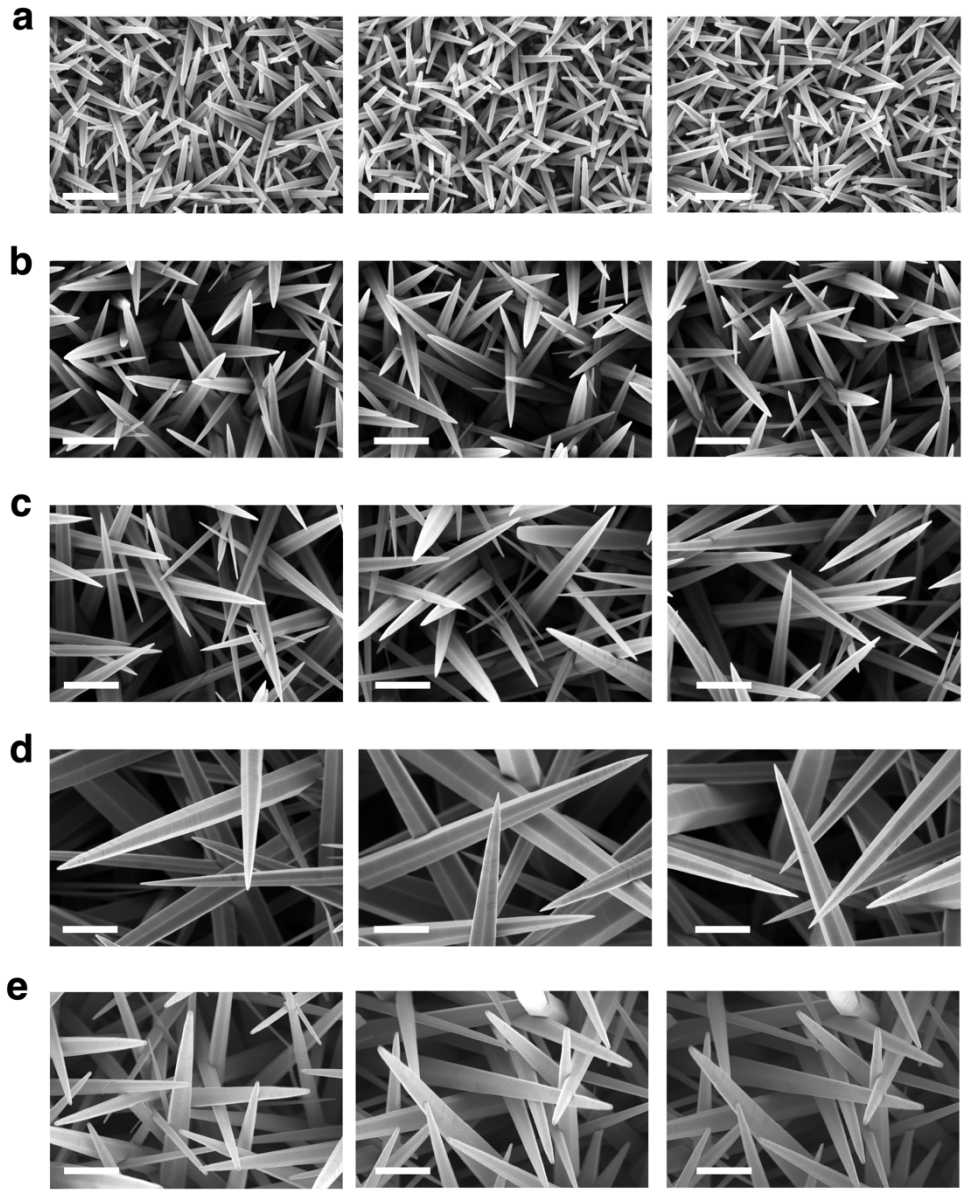

Fig. 19 Nanowire density measurement.

(a-d) The top-viewed FESEM images of ZnO nanowires from three different regions of each condition (3 h without NH_3, 3, 6, and 9 h reactions with NH_3, respectively). The scale bars are 1 μm. Numbers of nanowire tips in a known area were counted (*N = 486, 187, 103, 31, 105* counted nanowires for each condition, respectively) and then used to calculate the density of nanowires in the area (Fig. 18d).

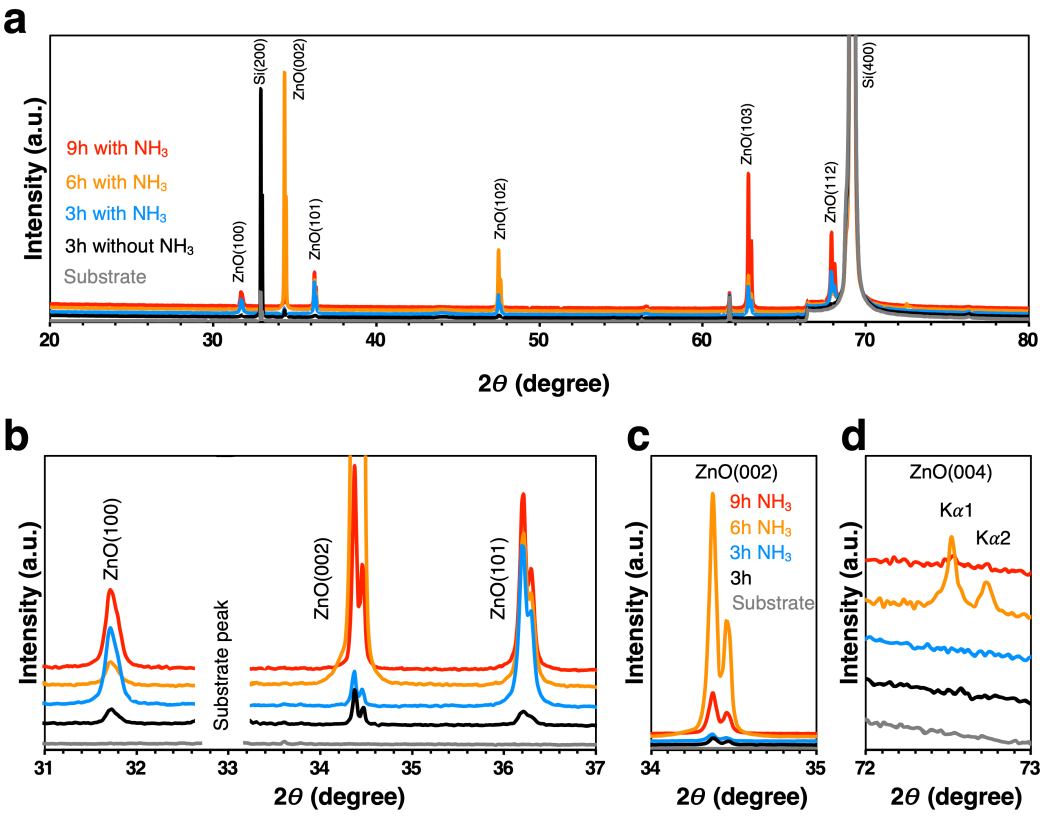

Fig. 20 The characterization of nanowire crystal structure and phase composition.

(a) Normalized full spectra XRD patterns. (b) Main characteristic peaks of ZnO wurtzite phase. (c) Enlarged ZnO (002) plane. (d) Enlarged ZnO (004) plane.

Table 3 The comparative intensity ratio of the characteristic XRD peaks of ZnO nanowires.

Sample	Peaks ratio		
	(002)/(100)	(002)/(101)	(100)/(101)
3h without NH_3	1.7	1.8	1.1
3h with NH_3	0.6	0.3	0.5
6h with NH_3	23.6	6.9	0.3
9h with NH_3	2.1	1.1	0.5
6h with NH_3 500℃	2.1	0.7	0.3

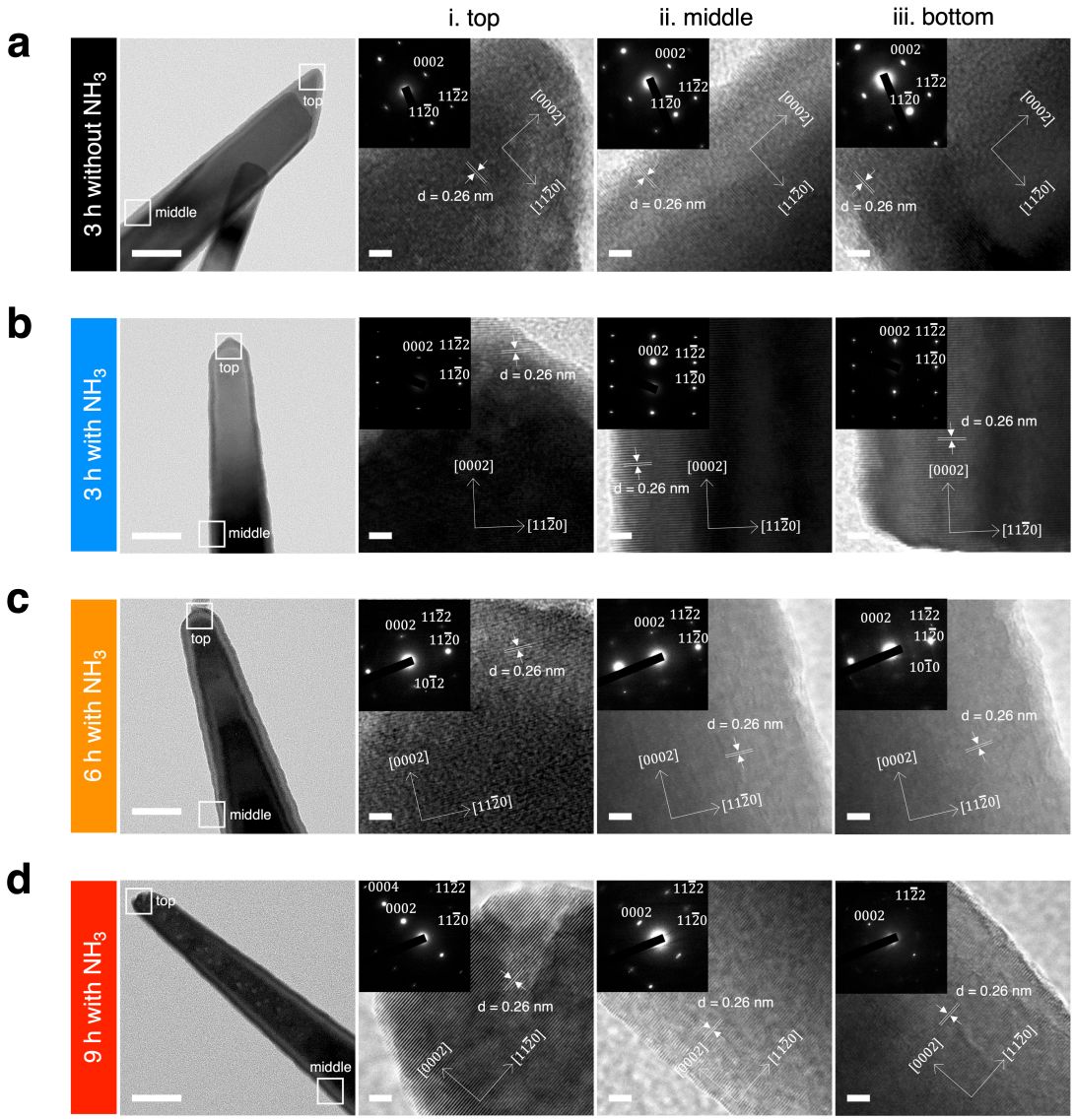

Fig. 21 The selective area electron diffraction (SAED) patterns of ZnO nanowires.

(a-d) Low-resolution TEM images, and HRTEM images in three regions of i. upper, ii. middle and iii. lower of a single ZnO nanowire, where (a) is a nanowire grown for 3 h without NH_3 addition; (b) is a nanowire grown for 3 h with NH_3 addition; (c) is a nanowire grown for 6 h with NH_3 addition; and (d) is a nanowire grown for 9 h with NH_3 addition. The insets are SAED patterns of each HRTEM micrograph. The scale bars are 50 nm and 2 nm in low-resolution TEM and HRTEM images, respectively.

Table 4 The inter planar spacing and diffraction planes of ZnO nanowires. ZB represents zinc blende.

Sample		Peak 2θ	d-spacing calculated from XRD (nm)	d-spacing calculated from HRTEM (nm)	hkl	Structure
3 h without NH_3	top	34.37	0.2609	0.2598	002	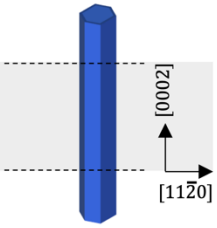
		56.31	0.1634	0.1602	110	
		67.91	0.1380	0.1359	112	
	middle	34.37	0.2609	0.2570	002	
		56.31	0.1634	0.1591	110	
		67.91	0.1380	0.1352	112	
	bottom	34.37	0.2609	0.2570	002	
		56.31	0.1634	0.1580	110	
		67.91	0.1380	0.1352	112	
3 h with NH_3	top	34.37	0.2609	0.2598	002	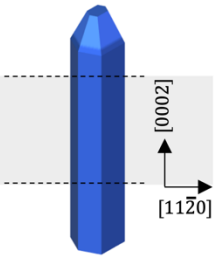
		56.31	0.1634	0.1602	110	
		67.91	0.1380	0.1359	112	
	middle	34.37	0.2609	0.2598	002	
		56.31	0.1634	0.1591	110	
		67.91	0.1380	0.1359	112	
	bottom	34.37	0.2609	0.2598	002	
		56.31	0.1634	0.1602	110	
		67.91	0.1380	0.1352	112	
6 h with NH_3	top	34.37	0.2609	0.2584	002	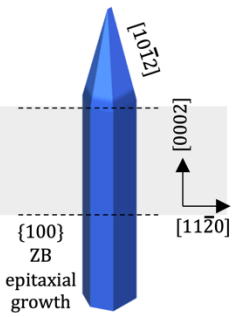
		47.49	0.1914	0.1897	102	
		56.31	0.1634	0.1596	110	
		67.91	0.1380	0.1371	112	
	middle	34.37	0.2609	0.2635	002	
		56.31	0.1634	0.1577	110	
		67.91	0.1380	0.1363	112	
	bottom	31.28	0.2859	0.2887	100	
		34.37	0.2609	0.2488	002	
		56.31	0.1634	0.1585	110	
		67.91	0.1380	0.1363	112	
9 h with NH_3	top	34.37	0.2609	0.2562	002	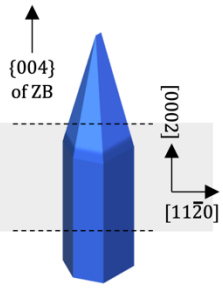
		56.31	0.1634	0.1602	110	
		67.91	0.1380	0.1352	112	
		72.52	0.1303	0.1294	004	
	middle	34.37	0.2609	0.2555	002	
		56.31	0.1634	0.1577	110	
		67.91	0.1380	0.1365	112	
	bottom	36.21	0.2480	0.2436	101	
		47.49	0.1914	0.1886	102	

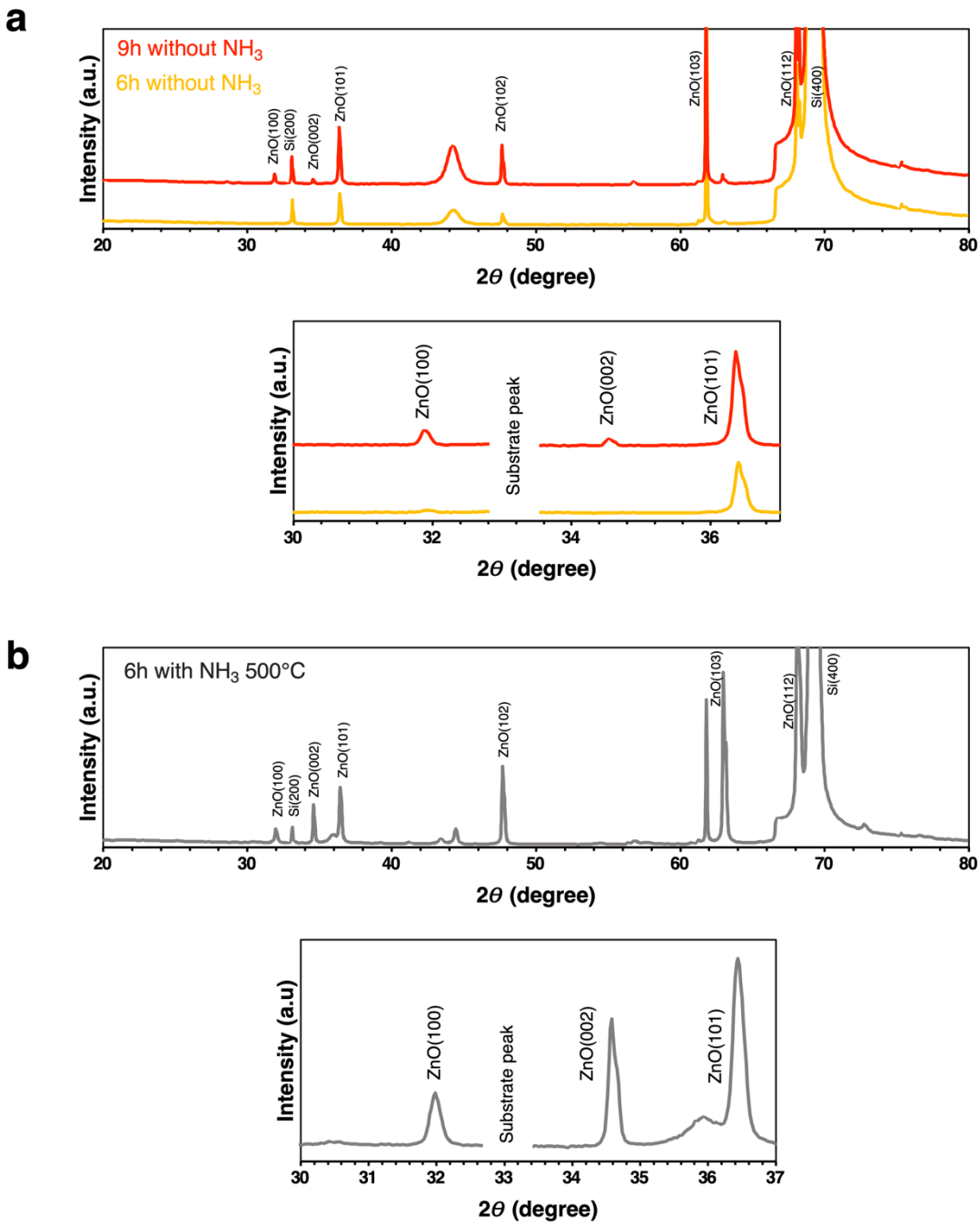

Fig. 22 XRD patterns.

(a) Normalized full spectra XRD patterns of 6 h and 9 h without NH_3 addition nanowires and the characteristic peaks of ZnO wurtzite phase. (b) Full spectrum XRD pattern of ZnO nanowire at 6 h with NH_3 annealed at 500°C, 2 h and the characteristic peaks of ZnO wurtzite phase.

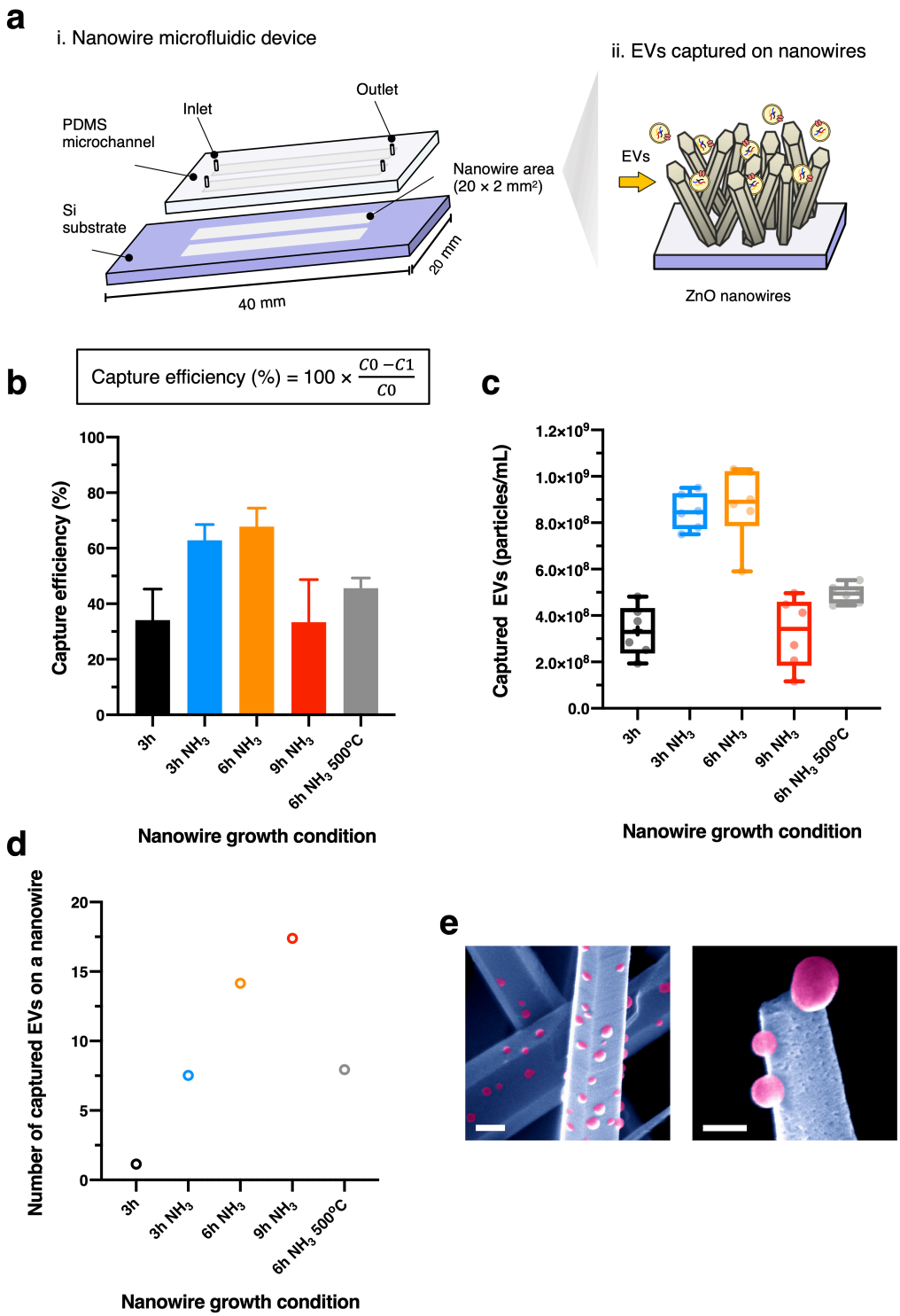

Fig. 23 The evaluation of EV capture performance by nanowires.

(a) Schematic images of the nanowire microfluidic device and EVs captured by nanowires. (b) The comparative EV capture efficiency and (c) NTA-based numbers of captured vesicles obtained using ZnO nanowire devices. Initial concentration of EVs was about 1.0×10^9 (particles/mL). Error bars indicate the standard deviation ($N = 6$). (d) Colored FESEM images visualize the adsorption of EVs (pink) on a ZnO nanowire surface (blue) after the EV capture experiment from 6 h with NH_3 and 3 h without NH_3 conditions, respectively. Scale bars are 100 nm. (e) The comparative capture capacity per unit area of a nanowire for each nanowire condition.

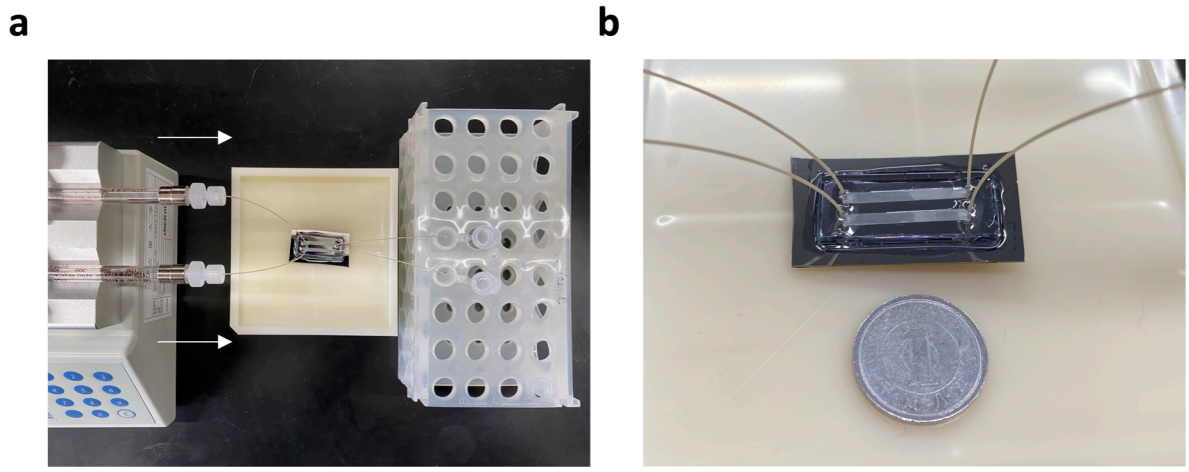

Fig. 24 EV capture experiment configuration.

(a) Sample injection system using an automatic syringe pump to continuously infuse EV sample into the flow channels with a constant flow rate of 10 μL/min. (b) Photograph of an assembled microfluidic device with the double-channel nanowire area comparing its size to that of a Japanese one-yen coin (diameter = 1.5 cm). ZnO nanowires grown in two patterned areas on Si substrated were integrated with a sheet of 30-μm-depth PDMS microchannels and PEEK capillary tubes for inlets and outlets. One channel was used for one experiment.

Chapter 4. Classifying Tumor-Specific Extracellular Vesicles via Charge-Based Isolation using ZnO Nanowire Microfluidics

4.1 Introduction

Extracellular vesicles (EVs) are small vesicles that contain and delivery molecular messages (e.g. DNA, microRNAs, proteins) in cell-to-cell communication.[134-136] In cancer research fields, these molecules serve as potential biomarkers that reflect physiological and pathological conditions of primary tumor cells. Therefore, isolation and analysis of EVs offer great potential in clinical applications including early detection, progression of the disease, as well as monitoring surgery and treatment responses.[111, 137-139] Trends of using extracellular EVs as highly informative biomarkers in disease diagnostics and precision medicine have been gradually growing up. Various methods have been proposing to isolate EVs from biological fluids, conventionally ultracentrifugation which provides high isolation yield, yet high uncertainties.[76, 140, 141] Moreover, in recent studies about heterogeneities of EVs subtypes, including small EVs (e.g. exosomes, exomeres) and large EVs (e.g. microvesicles), showed large verities in biological functions of each molecule and the separation of distinct EV subpopulations remains a challenge.[49, 142, 143] In order to reach the highest potential utilization of EVs, a specific separation with high purity of each molecule subset needs to be developed. The objective of this research is to develop a new methodology for specific separation and classification of EV subpopulations using oxide nanowire microfluidic devices based on physically and chemically specific surface-adsorption and desorption of EVs onto nanowire surfaces.

Extracellular vesicles (EVs), especially small EVs including exosomes, present a promising biomarker in liquid biopsy for cancer diagnosis and therapeutic monitoring, as they are enriched of bioactive molecules (for example, proteins, DNA, and microRNAs) which reflect current physiological conditions of the parental cells. Therefore, several approaches have been developed to isolate EVs from biological fluids base on the vesicle size, charge, density, and membrane affinity.[144] Ultracentrifugation is presently the main technique for EV isolation offering high yields, but low specificity and purity. The co-isolated contaminants, including lipoproteins and cell-free nucleic acids, could interfere with EV-encapsulated molecule interpretation resulting in the lower diagnostic efficiency.[145-147] Other approaches, such as immunoaffinity assay and size-exclusion chromatography, have emerged to enhance specific EV capture. However, they typically require expensive reagents (antibodies) and complex protocols with long incubation time. Besides, the heterogeneity of EVs have found to become another key barrier to our understanding of the composition and functional properties of

distinct secreted components.[139, 148] Whereas the biogenesis and function of exosomes is relatively well defined, other small EVs such as Exso-S and Exo-L which have overlapping sizes to exosome is still fundamentally mysterious.[149] The high-resolution density gradient fractionation and asymmetric flow field-flow fractionation methods have been developed to specifically isolate subpopulations of EV by their size and density, but its throughput is conceded by the complex sample preparation procedures.[49, 117, 150-152] Moreover, only size does not fully separate them according to the subpopulation.

In this study, we developed a methodology to classify small EV subpopulations via charge-based capture using nanowire device and a specific sequential elution assay for greater precision in sorting small EV subsets. The proposed method offers a great platform in nanoscale analysis; fast processing time, high EVs capturing efficacy, label-free detection, and simple elution assay, which is crucial for identification of biomarkers, fundamental study and design of future medical inventions. Our device is configurable between charge-based capture of EV onto nanowire surfaces via electrostatic interaction[37, 53, 92] and a sequential elution assay of different ionic strength solutions for specific desorption of the vesicles. Hence, the EV surface zeta potential is altered by the ionic strength of surrounding medium,[130] we designed our sequential elution assay using different concentrations of PBS buffer for specific EV subsets released without devastating of the vesicles (**Fig. 26**).

4.2 Method

a. Nanowire fabrication and characterization.

We fabricated ZnO nanowires on Si substrate via a seed-assisted hydrothermal process. A chromium (Cr) layer with thickness of 20 nm was deposited onto Si (100) substrate (Advantec Co., Ltd.) by electron cyclotron resonance (ECR) sputtering method (EIS-200ERT-YN, Elionix Inc.). High melting-point Cr-based alloy with purity of 99.999% (Kojundo Chemical Laboratory Co., Ltd.) was used as a sputtering target. First, Si (100) substrates were cut into 2 × 4 cm^2, the two fluidic areas (20 × 2 mm^2) were coated with a positive photoresist (OFPR8600, Tokyo Ohka Kogyo Co., Ltd.), the microchannel patterns were formed by photolithography and developed with a developer solution (NMD-3 2.38%, Tokyo Ohka Kogyo Co., Ltd.). After depositing Cr seed layer, the photoresist was removed using isopropanol at 70°C in a sonicator. The substrates with seed layer were oxidized in an oven at 400°C for 2 h to be scaffold of ZnO nanowires. After the seed layer preparation, the growth solutions were prepare using 15 mM hexamethylenetetramine; HMTA (ACS, Thermo Fisher Scientific) and 15 mM zinc nitrate hexahydrate; $Zn(NO_3)_2.6H_2O$ (Wako Pure Chemical Industries, Ltd.) as ZnO

nanowire precursors, and 0.8 M ammonium solution (Wako, Pure Chemical Industries) was added for ultra-lengthening of ZnO nanowires. The nanowires were grown with typical growth temperature of 95°C in an oven for 3 h. The morphology and the composition of ultra-long ZnO nanowires were characterized by field emission scanning electron microscope; FESEM (Supra 40VP, Carl Zeiss AG.), transmission electron microscopy; TEM (JEM-2100, JEOL USA Inc.) and energy dispersive x-ray spectroscopy; EDS (Ultim Max 100, Oxford Instruments). For the cross-sectional SEM-EDS analysis, we utilized an accelerating voltage of 15 kV.

b. Nanowire device fabrication.

After fabrication of ZnO nanowires on microchannel patterns, the substrates and nanowire were washed by deionized water and dry with nitrogen gas flow. The dried substrates were treated with oxygen plasma and attached a sheet of 30-μm-depth poly(dimethylsiloxane); PDMS (Silpot 184, Dow Corning Corp.) patterned with microchannels and 0.05 mm inlet and outlet holes. We used capillary PEEK tubes (ICT-55, Institute of Microchemical Technology Co., Ltd.) connecting microchannels with a microliter syringe (Hamilton Company) for sample injection.

c. Cell culture and EV purification by ultracentrifugation.

Human breast adenocarcinoma cells; MDA-MB-231 (American Type Culture Collection Co., Ltd.) were cultured in a complete medium DMEM (Thermo Fisher Scientific Inc.) supplemented with 10% exosome-depleted FBS (System Biosciences, LLC.) and 1% penicillin streptomycin (Life technologies). In each passage, 2×10^6 cells were seeded into 15 mL of complete medium in a 75 cm^2 culturing flask (Asahi Glass Co., Ltd.) and cultured in an incubator (Panasonic Corp.) at 37ºC and in 5% CO_2. After 48 h, the cell medium was taken from the culturing flask and filtered through a 0.22-μm filter (Merck Millipore Ltd.) to remove cellular debris. Next, the filtered medium was ultracentrifuged at 110,000 *g*, 4°C, 80 min (CS150FNX, Hitachi, Ltd.). After discarding the supernatant, we added 10 mL of 0.22-μm filtered phosphate-buffered saline; PBS (Thermo Fisher Scientific Inc.) to wash the EV pallets, and this solution was ultracentrifuged again with the same condition. After discarding the supernatant, 1 mL of 0.22-μm filtered PBS was added to collect EVs, the EV suspension was stored at 4ºC until use.

d. EV isolation and classification by nanowire device.

We integrated a nanowire device with a dual-channel syringe pump (Fusion 100, Chemyx Inc.) to continuously infuse EV sample with 10 μL/min of the constant flow rate. 250 μL of EV-suspended PBS was supplied into microfluidic nanowire device to capture EVs onto each nanowire. Subsequently, different concentrations of PBS were used for releasing the captured EVs by introducing 250 μL of buffer with 10 μL/min

of the flow rate. We used 1.0X M and 0.1X M PBS to evaluate specific elution based on alternation of EV surface charge in each buffer concentration. The feasibility of specific EV elution in each buffer was confirmed by designing the sequential elution experiments. For elution sequence #1, we firstly introduced 250 μL of 1.0X PBS to wash the nanowire device, followed by 250 μL of 0.1X PBS in the second wash. Conversely, in elution sequence #2, we introduced 0.1X and then 1.0X PBS, respectively.

e. EV characterization.

Concentration and size distribution of collected EVs were analysed using a nanoparticle tracking analysis (NTA) instrument (Malvern Panalytical, Ltd.) to calculate EV capture efficiency of nanowire device (**Fig. 25a**). After appropriate dilutions, video data were collected 5 times for a 60-s time period for each video. Camera level and detection threshold were set to 15 and 5, respectively. Data analysis was performed automatically by NanoSight NTA 3.2 software ((Malvern Panalytical, Ltd.). After isolation of EV onto nanowire surface, the nanowire devices were left to dry naturally at room temperature. Upper PDMS sheet was removed from the substrate, then the captured EVs on nanowire surface were directly observed using field emission scanning electron microscope; FESEM (Supra 40VP, Carl Zeiss AG.) at 5 kV of accelerating voltage without any fixation or coating processes. The surface charge of EVs was demonstrate by zeta potential measurement using a zeta-potential and particle size analyser (ELSZ-2000, Otsuka electronics).

f. Surface biomarker analysis by ExoView.

To obtain surface biomarker characteristics of each isolated EV subpopulation, we used single particle interferometric reflectance imaging sensing (SP-IRIS) by ExoView platform (ExoView R100, NanoView Biosciences). Starting from 10^8 to 10^9 particles of EV sample, the sample were adjusted to optimal concentrations; no dilution needed for 10^8 particles, diluted 1:1 of 10^9 particles with incubation solution supplied in the ExoView kits to avoid oversaturating the chip. The results presented in this research were obtained by using the ExoView Plasma Tetraspanin kit (NanoView Biosciences). We performed the analysis by using CD9, CD63 and CD81 as the detection antibodies and anti-CD9, anti-CD63 and anti-CD81 as the capturing antibodies. The diluted EVs was loaded on the ExoView chips and performed the protein membrane analysis following the manufacturer's instructions.

g. MicroRNA profile analysis by next generation sequencing (NGS).

After capturing of EVs in the device, the total exosomal RNAs (including small RNA and microRNA) were isolated using a commercial urine microRNA purification kit (Norgen, Biotek Corp.) and QIAseq miRNA library kit following the manufacturer's instructions and determine mutual miRNAs sequences on an NGS instrument (NextSeq 550, Illumina).

4.3 Results and Discussion

a. Capture and release of EVs by nanowire device and elution assay.

In this experiment, the nanowires grown with addition of ammonia (NH_3) solution at 3 h were used to demonstrate specific adsorption and desorption of EVs on nanowire surface. The device showed capacity of EV capture at 54% from the initial concentration about 1.0×10^9 EVs/mL (**Fig. 25a**). SEM image was used to confirm the adsorption of EVs on nanowire surface (**Fig. 25b**). This result indicated that the nanowire device had capability of label-free EV capture. To confirm the specific classification of EV subpopulations, we fabricated two different morphology and crystallinity (3 h with and without NH_3) based on our knowledge in chapter 3 that different crystallinities played crucial role in EV capture efficiency. Thus, we hypothesized that the crystal structure could adsorb different EV subtypes according to different surface energy and electrostatic properties between nanowire phases. Then, the elution buffers were introduced in two sequences (**Figs. 25c** and **25d**). Phosphate buffered saline (PBS) was used as an elution buffer since it is well known to preserve biomolecules from rupturing or shriveling up due to osmosis.[153, 154] Since the variation of buffer concentration, ionic strength, and pH value is possible to alter EV surface charge,[130] we took this advantage to competitively release the captured EVs on nanowire surfaces. The zeta potential measurement of EVs in different PBS concentrations was shown in **Fig. 26** indicating the largest charge difference could be achieved with 100% (1.0X M) PBS and 10% (0.1X M) PBS. Thus, with these elution buffers, EVs were isolated into two fractions based on surface charges. The sequential elution assay showed similar ratios of the released vesicles from two fractions in 3 h without NH_3 nanowire. Interestingly, in 3 h with NH_3 nanowire, the 0.1X PBS could elute a greater number of EVs compared to 1.0X PBS in both sequences. Moreover, the releasability was up to 99% from the total captured EVs. This result implied that the eluted subset of EVs using each buffer concentration were different and a specific desorption could be achieved with this assay.

b. EV membrane marker analysis using protein immunoassay.

To obtain surface biomarker characteristics of each isolated EV subpopulation, we used a single particle interferometric reflectance imaging sensing (SP-IRIS) by an ExoView analysis platform (**Fig. 27**). The protein immunoassay confirmed the presence of exosome-associated proteins (CD63, CD81, CD9)[155, 156] with unique ratio in each fraction. For the crude EVs from ultracentrifugation and uncaptured EVs had similarity in vesicle sizes (mean = 130 nm) and expression of all tetraspanins but highly enriched in CD63 (**Figs. 27a** and **27b**). Interestingly, the released EVs by 1.0X PBS showed relatively smaller in vesicle size (mean = 118 nm) and was enriched in CD9 with 83.6% from the total of three markers (**Fig. 27c**). Whereas, the 0.1X PBS eluted EVs that were enriched in CD81 (44.6%) compared to CD63 and CD9 (**Fig. 27d**). The results indicated that each EV fraction has different representative markers which might lead us to a distinguished group of EVs. Conventionally, an exosome fraction obtained from ultracentrifugation at 100,000 *g* has been considered as P100 fraction[157, 158] and the subsequently centrifuged at 200,000 *g* can obtain P200 pallets which are smaller than exosomes.[159] CD63 was found in both P100 and P200 fractions, and CD81 is highly enriched in the P100 fraction (i.e., exosomes) but not in the P200 (i.e., small EVs). EVs bearing only CD9 or CD81 but not CD63 probably did not form in endosomes (and were thus ectosomes), whereas those bearing CD63 together with one or the two other tetraspanins may correspond to endosome-derived exosomes.[160] Thus, we hypothesized that our approach could provide classification of EV subsets based on surface protein markers and determine the exosomal or extosomal nature of EVs containing the different tetraspanins.

c. EV-microRNA expression analysis.

Finally, we demonstrated the potential of in situ extraction of classified EV–encapsulated miRNAs using the nanowire device to find a unique miRNA profile in each subpopulation (**Fig. 28**). Because the device allowed us to analyze many species of miRNA, we compared the differentiated expression between EV groups. NGS analysis showed that crude EVs provided a greater variety of species miRNAs when compared to other groups (**Figs. 28a, c, d**). However, in the concept of classification, our methodology could provide distinguished profile of miRNA in 1.0X PBS and 0.1X PBS (**Fig. 28b**) and **Table 5**. Although we need to make more trials for clear recognition of statistically significant down-regulated and overexpressed miRNAs, based on current results, we can say that the device mainly classified two types of miRNA groups: miRNAs from CD9-enriched EV and CD81-enriched EV.

4.4 Conclusions

In previous study, we succeeded to control various morphologies of NWs by varying fabrication parameters in hydrothermal method and found that in different nanowires provide different EV isolation efficacy. In this study, we showed the development of a configurable the tailored zinc oxide nanowire microfluidic device to enable isolating and sorting tumor-derived small EVs with high sensitivity and specificity. The characterization of vesicles and quantification of carried molecules including membrane protein markers and EV-encapsulated miRNAs were analyzed to confirm specific isolation of the device. The recovered EV subsets obtained through charge-based isolation would provide a unique insight into EV information corresponding to EV contents, offer a new understanding of small EV heterogeneity base on surface charges in tumor cell biology as well as would be beneficial for the development of high precision of cancer diagnostic and therapeutic strategy.

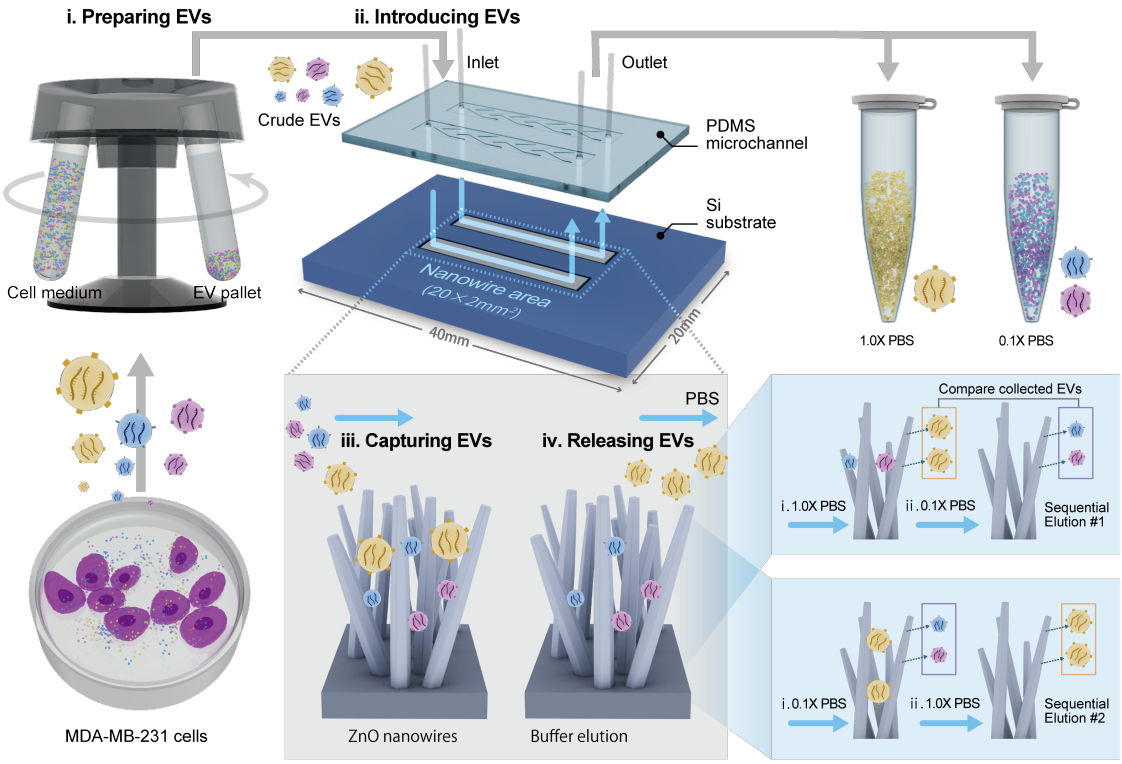

Fig. 24 EV classification by nanowire device.

(a) The Schematice illustration shows steps in EV classification by surface charge-based isolation using ZnO nanowire device. Breast cancer (MDA-MB-231) cell-derived EVs were collected and extracted from cell culture medium using ultracentrifugation (i. and ii.). EV pallets (crude) were resuspended in PBS and flown through nanowire device, the EVs were captured onto nanowire surface and subsequently releaseded by different concentrations of PBS (iii. and iv.).

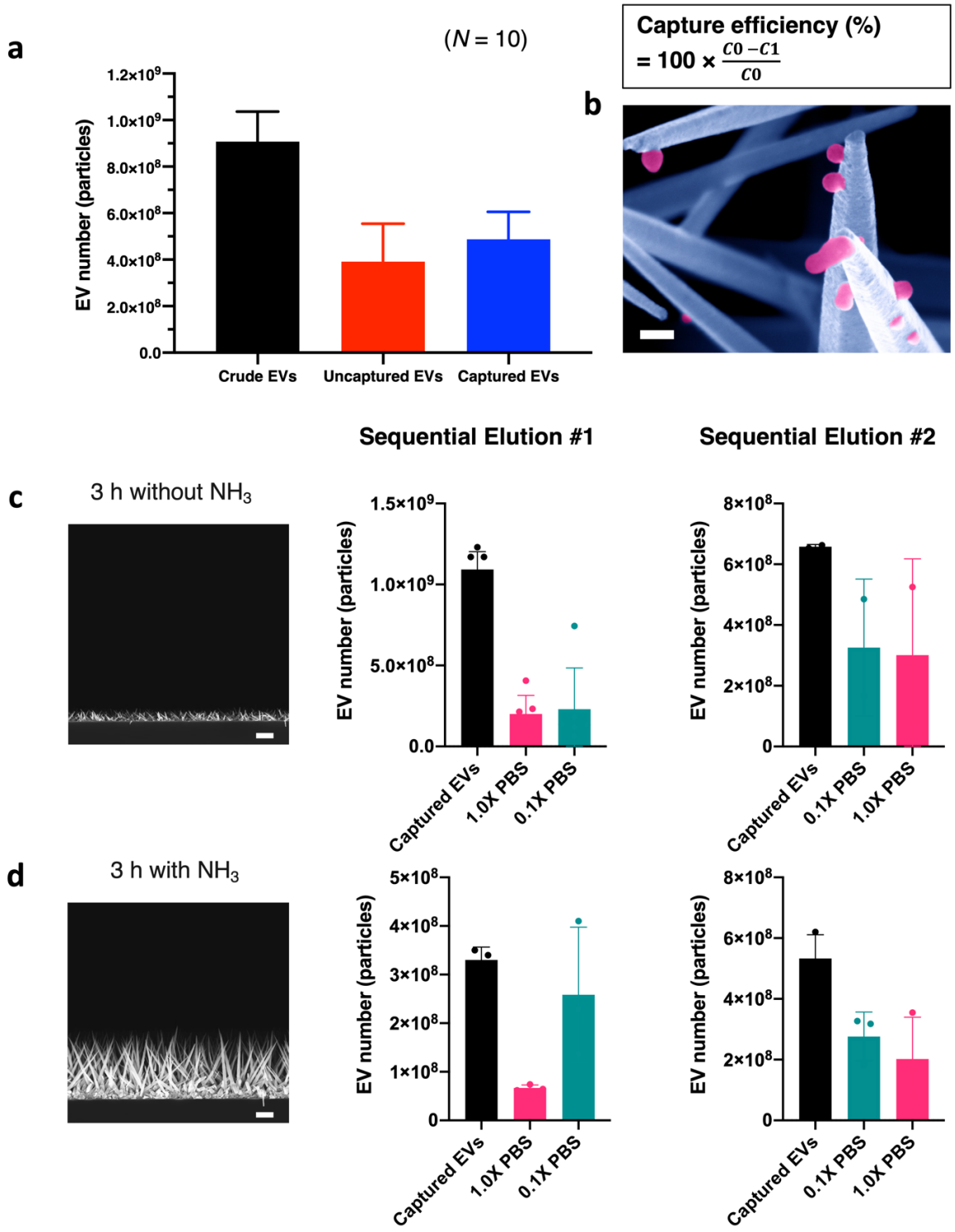

Fig. 25 Capture and release of EVs by nanowire device and elution assay.

(a) The performance to isolate EVs using nanowire device was evaluated by capture efficiency. The initial concentration of crude EVs was about 1×10^9 particles/mL, around 5×10^8 particles were captured by nanowire device (*N = 10*), which was 54% of total initial EVs. (b) The SEM image shows adsorbtion of EV particles (pink) onto ZnO nanowire surface (blue). The scale bar is 100 nm. (c) The sequential elutions using different PBS concentrations (1.0X M PBS and 0.1X M PBS) to specicfically release EV subpopulations from 3 h

without NH_3 nanowire (*N = 3*). (d) The sequential elutions using different PBS concentrations (1.0X M PBS and 0.1X M PBS) to specicfically release EV subpopulations from 3 h with NH_3 nanowire (*N = 3*). Sequential elution #1 was to introduce 1.0X PBS followed by 0.1X PBS. Sequential elution #2 was to introduce 0.1X PBS followed by 1.0X PBS.

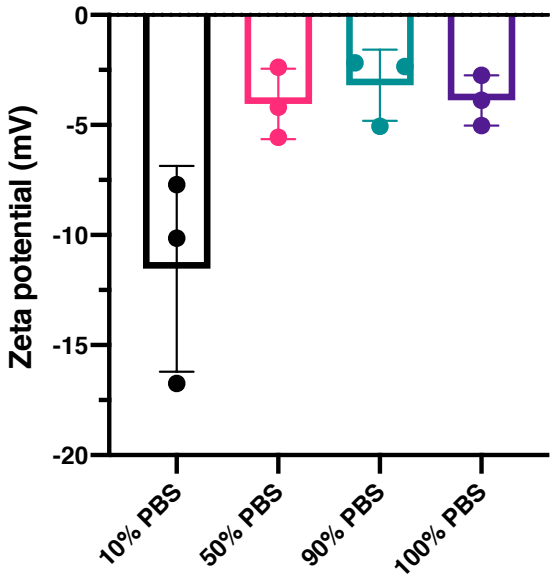

Fig. 26 Zeta potential of EVs in different PBS concentrations.

Since the variation of buffer concentration and ionic strength is possible to alter EV surface charge, we took this advantage to competitively release the captured EVs on nanowire surfaces. The zeta potential measurement of EVs in different PBS concentrations indicated the largest charge difference could be achieved with 100% (1.0X M) PBS and 10% (0.1X M) PBS.

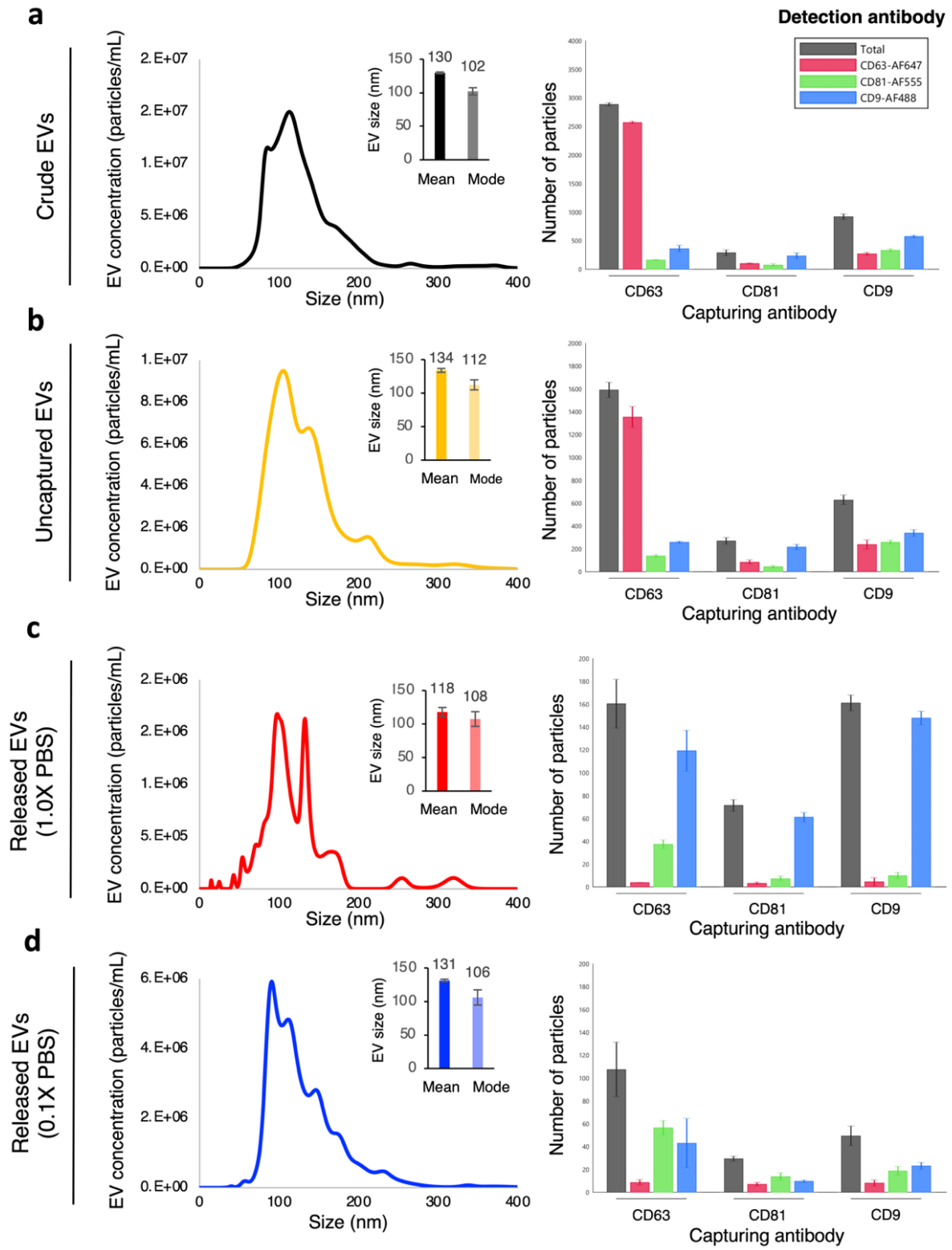

Fig. 27 Size distribution of EVs and membrane protein analysis.

(a) The size distribution and membrane protein signatures of crude EVs obtained from ultracentrifugation. (b) The size distribution and membrane protein signatures of uncaptured EVs by nanowires. (c) The size distribution and membrane protein signatures of released EVs from nanowires by 1.0X PBS. (d) The size distribution and membrane protein signatures of released EVs from nanowires by 0.1X PBS.

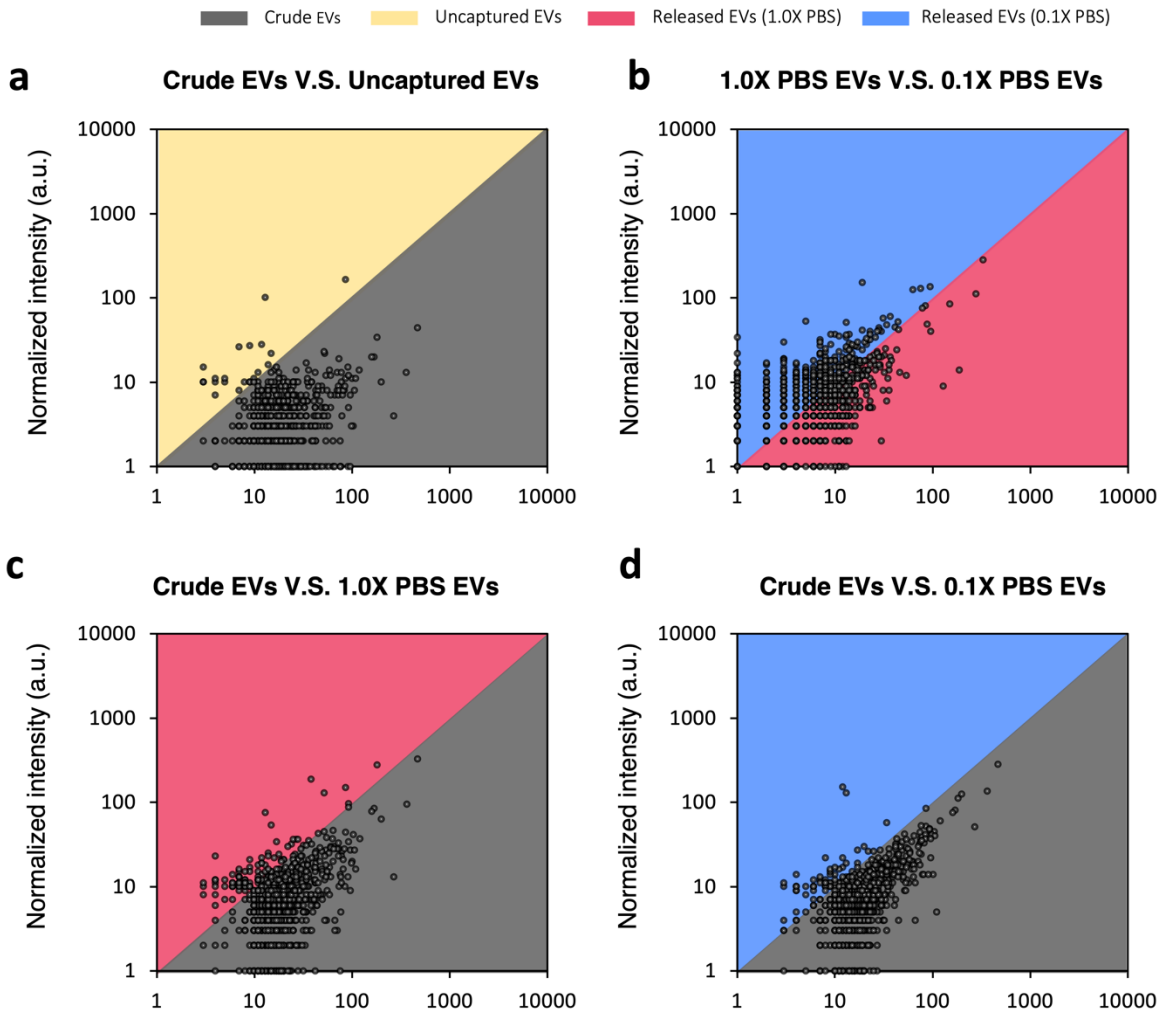

Fig. 28 EV-miRNA expression analysis from next generation sequencing (NGS).

(a) The scatterplot of normalized intensities of miRNAs extracted from crude EVs (ultracentrifuged) versus uncaptured EVs by nanowires. Each point corresponds to a different miRNA species. The boundary between yellow and gray represents the same level of miRNA expression for the two subsets. (b) The scatterplot of normalized intensities of miRNAs extracted from the released EVs from nanowires by 1.0X PBS versus 0.1X PBS. The boundary between pink and blue represents the same level of miRNA expression for the two subsets. (c) The scatterplot of normalized intensities of miRNAs extracted from crude EVs (ultracentrifuged) versus the released EVs from nanowires by 1.0X PBS. The boundary between gray and pink represents the same level of miRNA expression for the two subsets. (d) The scatterplot of normalized intensities of miRNAs extracted from crude EVs (ultracentrifuged) versus the released EVs from nanowires by 0.1X PBS. The boundary between gray and blue represents the same level of miRNA expression for the two subsets.

Table 5 The profiling of top 50 high expression miRNAs from each EV fraction.

EV-miRNAs from 1.0X PBS	EV-miRNAs from 0.1X PBS	Mutual miRNAs
hsa-miR-4448	hsa-miR-625-3p	hsa-miR-4651
hsa-miR-598-3p	hsa-miR-4517	hsa-miR-143-3p
hsa-miR-610	hsa-miR-3130-5p	hsa-miR-5196-5p
hsa-miR-6727-5p	hsa-miR-4793-5p	hsa-miR-3974
hsa-miR-6879-3p	hsa-miR-3162-3p	hsa-miR-197-3p
hsa-miR-6752-5p	hsa-miR-6815-3p	hsa-miR-6801-5p
hsa-miR-3688-3p	hsa-miR-188-3p	hsa-miR-1909-3p
hsa-miR-6834-5p	hsa-miR-765	hsa-miR-6779-5p
hsa-miR-6750-5p	hsa-miR-936	hsa-miR-3168
hsa-miR-7974	hsa-miR-944	hsa-miR-6745
hsa-miR-4661-5p	hsa-miR-92a-1-5p	hsa-miR-5692a
hsa-miR-3938	hsa-miR-6857-3p	hsa-miR-3141
hsa-miR-6717-5p	hsa-miR-7111-5p	hsa-miR-4440
hsa-miR-4302	hsa-miR-7108-3p	hsa-miR-6729-3p
hsa-miR-6802-5p	hsa-miR-4655-5p	hsa-miR-6825-3p
hsa-miR-532-3p	hsa-miR-218-2-3p	hsa-miR-6795-5p
hsa-miR-4459	hsa-miR-1273e	hsa-miR-1247-5p
hsa-miR-6781-5p	hsa-miR-3935	hsa-miR-3613-3p
hsa-miR-483-3p	hsa-miR-874-3p	hsa-miR-6078
hsa-miR-5001-5p	hsa-miR-659-5p	hsa-miR-6756-3p
hsa-miR-6738-5p	hsa-miR-4786-5p	hsa-miR-4739
hsa-miR-6749-5p	hsa-miR-3127-5p	
hsa-miR-885-3p	hsa-miR-3124-5p	
hsa-miR-1908-5p	hsa-miR-6768-5p	
hsa-miR-6743-3p	hsa-miR-6785-5p	
hsa-miR-6790-5p	hsa-miR-1237-3p	
hsa-let-7b-5p	hsa-miR-4716-3p	
hsa-miR-4796-3p	hsa-miR-3668	
hsa-miR-718	hsa-miR-326	

Chapter 5. Elimination of Cancer Cell-Derived Extracellular Vesicles by Oxide Nanowires for *in vitro* Metastasis Suppressing

5.1 Introduction

Growing of evidences indicated that EVs involve in metastasis and proliferation of cancers, but, thus far, how their elimination from biofluid in order to inhibit the abnormal growth of cell has been poorly understood. Here, we describe an EV-elimination device using nanowires which can efficiently remove metastases from cancer cell-derived EV components including proteins and miRNAs for inhibiting abnormal growth in recipient cell without toxicity to the cells. EVs from breast adenocarcinoma cells (MDA-MB-231) supernatant incubated within an integrated device that induces specific adsorptions of EVs onto oxide nanowire surfaces. The cleansed medium is then transferred to the culture environment of mammary gland epithelial cells (MCF10A), the proliferation rate was evaluated to demonstrate *in vitro* metastasis suppressing using nanowire devices. The data provides evidence that the irregularly high proliferation rate of cells almost abolished by eliminating the number of EVs by nanowires. Our methodology provide new possibilities for researchers to achieve a deeper understanding of metastasis supressing by the effective and specific reduction of EV numbers from body fluids for developing an alternative tool, namely a nanowire-based blood purification device, in cancer therapy.

Extracellular vesicle (EV) is a membrane vesicle with heterogeneous types and sizes ranging from 40-1000 nm secreted from all cells in the body,[39, 43, 109] and it presents circulating in body fluids such as blood, urine, saliva, and semen.[161] In recent years, it has been found that EV is involved in various *in vivo* phenomena including intercellular communication, diseases progression and aging.[5, 38, 45, 109, 162, 163] EVs play a key role in propagating the spread of disease-related conformation including miRNA and proteins in cancers, cardiovascular diseases, and neurodegenerative diseases.[164, 165] In cancers, evidence supporting a role for EVs in propagation the spread of disease-associated regulators to distant cells through the blood vessels and lymph has been drawn from a number of studies.[1, 42, 166, 167]

Metastasis are characterised by the presence of abnormal, pathogenic agents that can induce abnormal growth of specific normal cells and leads to the development of cancer tumors.[166, 168-171] It is reported that the level of EVs is significantly higher in body fluids as EVs are increasingly secreted from cancer cells, compared to normal cells.[172-174] The investigation of EVs elimination is an important aspect of understanding metastasis suppression mechanism, as the disease-associated regulators in EVs, such as miRNAs, can trigger healthy cells

to grow abnormally.[175, 176] While EVs depletion is difficult to study, *in vitro* studies suggesting direct corelation of EV-depleting by nanowire device[37, 177] and cell proliferation as potential mechanisms for inhibiting cancer propagation is possible. Although some studies examined how manipulating the release of EVs impacted proteins and miRNA transmission between cells,[61, 178-181] the studies of EVs depletion are lacking.

Blood purification is a methodology of removing pathogens which trigger severity and mortality in patients with infectious and non-infectious diseases, including sepsis,[182, 183] COVID-19,[184-186] and cancers.[187, 188] Several blood purification devices have been developed as an alternative treatment and several devices are currently on the market.[189-191] From the best of our knowledge, a therapeutic model using blood purification device that specifically remove EVs for cancer metastasis suppressing has not been studied elsewhere. Here, we propose a methodology using oxide nanowires with potential to eliminate EVs from cell culture medium based on surface charge and we investigate a correlation between isolation efficiency of EVs and *in vitro* cancer metastasis suppressing. The importance of EV depletion in biological fluid was highlighted, we used a cell proliferation assay to show that EV-driven modulation of a healthy epithelia cell over differentiating is dependent on the amounts of EV in cell culture environment. As the normal state of cell proliferation was observed, the proliferation rate could possibly be used to distinguish between normal and EV-associated states of cell growth.

5.2 Method

a. Cell culture.

For culture of human breast adenocarcinoma cells (MDA-MB-231; American Type Culture Collection), the complete growth medium was prepared by DMEM (Lonza) and 10% (v/v) exosome-depleted FBS (System Biosciences). The concentration of 2×10^6 cells/mL suspension was then dispersed in a 75 cm^2 cell culturing flask with 15 mL of the complete medium, and cultured in an incubator (Sanyo) at 37ºC and in 5% CO_2. For mammary gland epithelial cells (MCF10A; American Type Culture Collection), the 1×10^6 cells/mL suspension was seeded in a 25 cm^2 cell culturing flask with 5 mL of the MEGM BulletKit medium (Lonza), and cultured in an incubator (Sanyo) at 37ºC and in 5% CO_2.

b. Extracellular vesicles extraction from MDA-MB-231 cells.

After 48 h of cell incubation, the supernatant of cultured MDA-MB-231 cells was collected and filtered through a 0.22-μm filter (Merck Millipore) to remove cellular debris. Next, the filtered suspension was ultracentrifuged (80 min, 4°C, 110,000 *g*; Hitachi) to exact EV pallets. The supernatant was removed, then 10 mL of 0.22-μm filtered phosphate-buffered saline (PBS; Thermo Fisher Scientific) was added to wash the pallets, and the ultracentrifugation was performed one more time under the same condition. After discarding the supernatant, 1 mL of 0.22-μm filtered PBS was added to disperse palleted EVs, and the EV suspension was stored at 4ºC. The size and concentration of EVs were determined by nanoparticle tracking analysis (NanoSight NTA; Malvern Instruments). The zeta potential of EVs was measured using a zeta potential analyser (Zetasizer Nano ZS; Malvern Instruments).

c. Nanowire fabrication and characterization.

ZnO nanowires were fabricated using previous reported method.[92] Briefly, 15 nm-thick chromium (Cr) seeding layer was deposited onto 20 mm × 20 mm Si (100) substrate by ECR sputtering (Elionix). The Cr layer was oxidized at 400ºC for 2 h, then immersed in 50 mL growth solution (15 mM HMTA; Fujifilm Wako Pure Chemical Corp. and 15 mM $Zn(NO_3)_2.6H_2O$; Thermo Fisher Scientific) at 95 ºC for 3 h. Metal oxides, including TiO_2 layer and SiO_2 layer, were deposited on the ZnO nanowires by atomic layer deposition (ALD) technique. Morphology and composition analysis of ZnO (bare), ZnO/TiO_2 (core/shell), and ZnO/SiO_2 (core/shell) nanowires were characterized by field emission scanning electron microscope (FESEM; Jeol), scanning transmission electron microscopy (STEM) and energy dispersive x-ray spectroscopy (EDS).

d. Extracellular vesicles capture using nanowire device.

The EV-treatment by nanowires was set in the chamber between two connector blocks of a custom-made Teflon holder (**Fig. 34**). The nanowire substrate was aligned on the lower block, and assembled with the upper block into a single integrated device that was tightened together by screws. The holder was placed in a closed container filled with an amount of water to prevent the sample evaporation. The 1 mL of EV-suspended PBS was supplied and incubated in the chamber at room temperature for 1, 3, 6, and 12 h with a shaker. After isolate EVs by each nanowire device, the solution was collected and used as a recovered solution. Size distribution and concentration of EVs were determined by nanoparticle tracking analysis (NanoSight NTA; Malvern Instruments).

e. Cell proliferation assays.

The MCF10A cells were seeded in a 96-well microplate (Corning) with the density of 5×10^3 cells/well and incubated at 37ºC and with 5% CO_2. After 24 h, the culture medium was discarded and replaced, independently, with EV-suspended and EV-treated media using oxide nanowire devices. On the first and fifth day (Day 1 and Day 5) of culturing, the cell viability was examined using cell counting kits (Dojindo Laboratory). The absorbance was measured at 450 nm wavelength in a microplate reader (BMG Labtech).

f. *In-vitro* imaging of EVs diffused in MCF10A cells.

The purified EVs obtained by ultracentrifugation from the MDA-MB-231 cells were labelled using PKH26 red fluorescent cell linker kits (Sigma-Aldrich) with instructions from the company. The MCF10A cells were seeded into a 33 mm culture dish at 5×10^3 cells/200 μL, and first incubated for 24 h. The medium was then replaced by the suspension of 20 μL of labelled EVs in 200 μL of DMEM and 10% (v/v) exosome-depleted FBS, and further incubated for 24 h. The cells were fixed with 10% (w/v) paraformaldehyde solution (Fujifilm Wako Pure Chemical Corp.), followed by the nuclei staining with Hoechst33342 fluorescent dye (Dojindo Molecular Technologies) and cytoskeleton Alexa488 fluorescent dye (Thermo Fisher Scientific). Cell morphology and composition were observed using a confocal microscope (Nikon).

g. EV-derived microRNA sequencing analysis.

The 1 mL of cell lysis buffer (Fujifilm Wako Pure Chemical) was added into the MDA-MB-231-derived EV pallets, and incubated at room temperature for 5 min. The EV- encapsulated miRNAs were extracted using a SeraMir Exosome RNA purification column kit (System Biosciences). Concentration and sequencing of the EV-derived microRNAs were then analysed by an ultra-micro spectrophotometer (NanoDrop Technologies) and a next-generation sequencing (BGI Genomics), respectively.

5.3 Results and Discussion

a. Cell proliferation test for evaluating metastatic activity.

To evaluate the effect of EVs elimination for cancer metastasis suppressing, we used a cell proliferation test as a model system. The model of cancer metastasis induced by EVs was described by the phenomenon that normal mammary gland epithelial cells cultured with breast cancer cell-derived EVs were acquired abnormal growth rate, which potentially resulting in tumor development in the recipient cells. We constructed an evaluation system for the suppression of metastasis activity by removing cancer cell-derived EVs from the culture environment using oxide nanowire devices. Then, the degree of proliferation of the epithelial cells were compared, and it was evaluated whether or not abnormal proliferation can be suppressed by the EV elimination effect by nanowires (**Fig. 29**).

In constructing this system, it is necessary to optimize the abnormal growth conditions of normal cells (positive control in this study). EVs derived from MDA-MB-231 (breast cancer cells) was added into the cultural environment of MCF10A (mammary gland epithelial cells), conditions that EVs induce abnormal cell growth were identified. The definition of abnormal cell growth is defined as comparing the growth rate with cells cultured in a normal state without adding EVs suspension when the p-value is less than 0.01 in statical analysis by T-test. The optimal condition parameters to promote abnormal proliferation rate in MCF10A cells were examined, including cell culture medium, cell passage number, cell seeding concentration, and concentration of added EVs. **Fig. 30** shows the ratio of the degree of cell proliferation under each condition to the degree of cell proliferation without the addition of cancer cell-derived EVs. From these results, it was confirmed that MCF10A cells at passage number 5 (P5) which were seeded at 5000 cells/well and cultured in MEBM medium with the condition of 10^8 to 10^9 EVs/mL were optimal for evaluating proliferation rate.

b. Surface charge-based EV capture ability of oxide nanowire devices.

To remove EVs from cell supernatant, we developed a device integrated oxide nanowires which provides the high surface-to-volume ratios with diverse isoelectric points of metal oxide materials to promote efficient charge-based EV capture. Zinc oxide nanowire (ZnO) were prepared by a hydrothermal synthesis method, then TiO_2 layer and SiO_2 layer were deposited onto ZnO nanowires to promote core-shell structure of ZnO/TiO_2 and ZnO/SiO_2 nanowires using atomic layer deposition (ALD) technique (**Fig. 31a** and **31b**). The hydrothermal synthesis method allows us to manipulate the morphology and crystal growth orientation of nanowire by controlling the growth time and the precursors concentration. For EV separation in this device, we used the precursors concentration at 15 mM and 3 h growth time as it offered ZnO nanowire with the highest surface-

to-volume ratio. The presence of TiO_2 and SiO_2 layers was confirmed on the ZnO nanowire surface by energy dispersive X-ray spectroscopy (EDS) (**Fig. 31c**). To provide enough space allowing the EVs with 40 – 1000 nm in diameter to enter the gap between nanowires, it is necessary to perform thin metal oxide layer while maintaining the structure. SEM images were used to measure the diameter of nanowires before and after deposition, the thin metal oxide layer about 15 nm were calculated (**Fig. 31d**).

The cancer cell-derived EVs used for the elimination test was concentrated from the culture supernatant of breast cancer cells (MDA-MB-231) at 80% cell confluency by ultracentrifugation. The vesicles had an average zeta potential (ζ) of -22.5 mV (**Fig. 32a**) and average diameter of 140.1 nm (**Fig. 32b**). The EVs were introduced into the devices integrated ZnO nanowires, ZnO/TiO_2 nanowires, or ZnO/SiO_2 nanowires, and the elimination efficiency was evaluated by comparing the EV concentrations before and after the introduction into the devices (**Fig. 33**). These results showed that the device with ZnO nanowires could separate EVs with the highest efficiency followed by ZnO/TiO_2 nanowires and ZnO/SiO_2 nanowires, respectively (**Fig. 32c**). This difference in separation efficiency was considered to be an effect of magnitude relationship of the electrostatic interaction between EVs and oxide nanowire surface charges. Each metal oxide has its instinct isoelectric point (IEP); the surface is positively charged when the isoelectric point is large relative to solution pH, in the other hand for negatively charged surface.[192, 193] Since the pH of the EV dispersion solvent (PBS: saline) in this experimental system was 7.2, it was supposed that the surface charge of ZnO nanowire (IEP 8.7 – 10.3) will be positive, ZnO/TiO_2 nanowire (IEP 3.9 – 8.2) and ZnO/SiO_2 (IEP 1.6 – 3.5) nanowire will be negative. According to the negatively charged EVs, the magnitude relation of the electrostatic interaction with nanowires is in the order of ZnO > TiO_2 > SiO_2, which is consistent with the elimination efficiency in the present results. On one hand, this suggests that the difference in the isolation capacity of each metal oxide nanowire is due to the difference in electrostatic interaction. On the other hand, TiO_2 and SiO_2 which cause electrical repulsion to EVs also had ability to separate EVs. Therefore, it was supposed that there are possibilities that EVs are adsorbed by nanowire in different manners other than the electrostatic interaction. The presence of a sugar chain has been confirmed on EV membrane surface where hydroxy group, carboxyl group and amide group are found.[110, 194, 195] One of the possibilities is that adsorption occurring by unpaired electrons in these functional groups formed a coordination bond to metal atoms on the oxide surface. In addition, the size distribution of EVs before and after the introduction to nanowire devices were measured showing the variations in each oxide nanowire (**Fig. 34**). In case of ZnO nanowires, the size distribution of uncaptured EV was relatively larger than

the ones of TiO_2 and SiO_2 nanowires. This result supports the assumption that EV subgroups were specifically separated in different metal oxide materials.

c. Evaluation of cancer metastasis inhibitory ability by cell proliferation test.

The ability of oxide nanowires to suppress cancer metastasis was evaluated using an evaluation system based on a cell proliferation test. EVs derived from MDA-MB-231 cells in MEBM medium were eliminated by each oxide nanowire device (incubated and stirred for 1 h), then the recovered solution from device was added to MCF10A cell culture medium. The numbers and cell proliferation rate of MCF10A cells cultured in the recovered solution were observed. The results showed that when ZnO nanowire device was used, the degree of normal cell proliferation was zero (**Fig. 35a**), and microscopic observation found that cell growth was stopped or cells died (**Fig. 35b**). The same phenomenon was observed when only the culture medium without EVs (negative control) was introduced into the ZnO nanowire device and the recovered solution was added to the MCF10A cells. Therefore, it was considered that the factor that deteriorated the cell state was due to the cytotoxicity of ZnO nanowire.[196-198] Therefore, ZnO nanowires were considered to be unsuitable for EV elimination device to inhibit metastasis, even though it provided the highest EV capture efficiency.

Next, the elimination capacity of the ZnO/TiO_2 nanowires and the ZnO/SiO_2 nanowires were evaluated. In these cases, the suppression of abnormal growth of MCF10A cells was observed by the EV eliminating using the devices. This was considered to be a result of the concentration of EVs added to MCF10A cells was partially eliminated and were lower than the threshold value of causing the abnormal growth. When the concentration of the extracellular vesicle was reduced to one-tenth, it was confirmed that abnormal growth did not occur (**Fig. 35c**). In addition, it was confirmed that there was no cytotoxicity from the result of the microscopic observation and the result of the control condition (**Fig. 35d**). From the above results, abnormal growth suppression was confirmed by the cell proliferation test, suggesting that ZnO/TiO_2 nanowires and ZnO/SiO_2 nanowires were able to eliminate cancer cell-derived EVs and inhibit cancer metastasis in the culture condition.

In addition, to confirm the localization of cancer cell-derived EVs in the epithelia MCF10A cells, we used a red fluorescent dye (PKH26) for EV tracking. Confocal microscopic imaging showed PKH26-labelled EVs were found assembled inside the cytoplasm of MCF10A cells, indicating the diffusion of EVs into the recipient cells (**Fig. 36**). Furthermore, microRNAs extracted from MDA-MB-231 cancer cell-derived EVs were analysed to confirm the inducing effect in the abnormal epithelia MCF10A cell growth. The next-generation sequencing analysis (NGS) showed the presence of miRNA-21[199] and miRNA-10b[200] which were reported to be associated with cancer progression suggesting that the EV-miRNAs induced abnormal growth in the

recipient cells (**Table 6**). We confirmed that our methodology of introducing EVs into the culture medium of a normal cell in a certain condition promotes abnormal growth by the invasion of EVs into cell cytoplas and the association of EV-miRNA regulations.

5.4 Conclusions

To summarize, we have demonstrated that our nanowire device could achieve eliminating of cancer cell-derived EVs to reduce the abnormal cell proliferation rate in the recipient cells. The positively charged surface of the ZnO nanowire allowed us to isolate the highest numbers of EVs, however cell cytotoxicity was found. Interestingly, the devices integrated with ZnO/TiO_2 nanowires and ZnO/SiO_2 nanowires, which have negatively charged surface, could offer the sufficient ability to partially remove EV numbers to be lower than the threshold value of causing the abnormal growth and cytotoxicity was not occurred with these nanowires. These results provide a proof-of-concept for the use of oxide nanowire as a promising EVs elimination platform, namely blood purification therapy, to inhibit the spread of metastases. Even though further trials need to be performed to confirm the feasibility of the device in real sample, such as whole blood and plasma, we believe that the current result opens up a new possibility in the development of future therapeutic strategies against cancer progression.

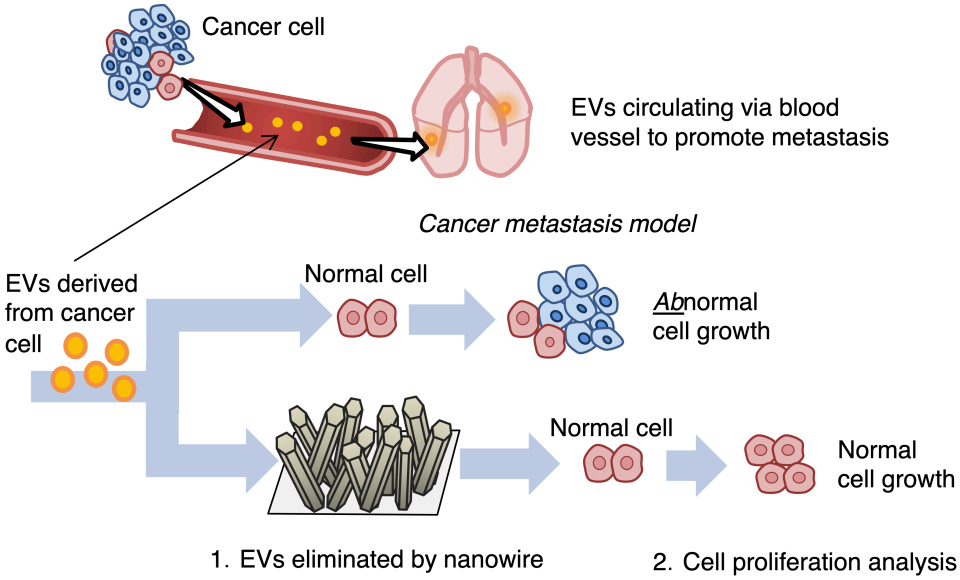

Fig. 29 Schematic illustration of the propose method.

The model of cancer metastasis induced by EVs was described by the phenomenon that normal mammary gland epithelial cells cultured with breast cancer cell-derived EVs were acquired abnormal growth rate, which potentially resulting in tumor development in recipient cells. We constructed an evaluation system for the suppression of metastasis activity by eliminating cancer cell-derived EVs from the culture environment using oxide nanowire devices. Then, the degree of proliferation of the epithelial cells were compared, and it is evaluated whether or not the abnormal proliferation can be suppressed by EV eliminating effect using nanowire devices.

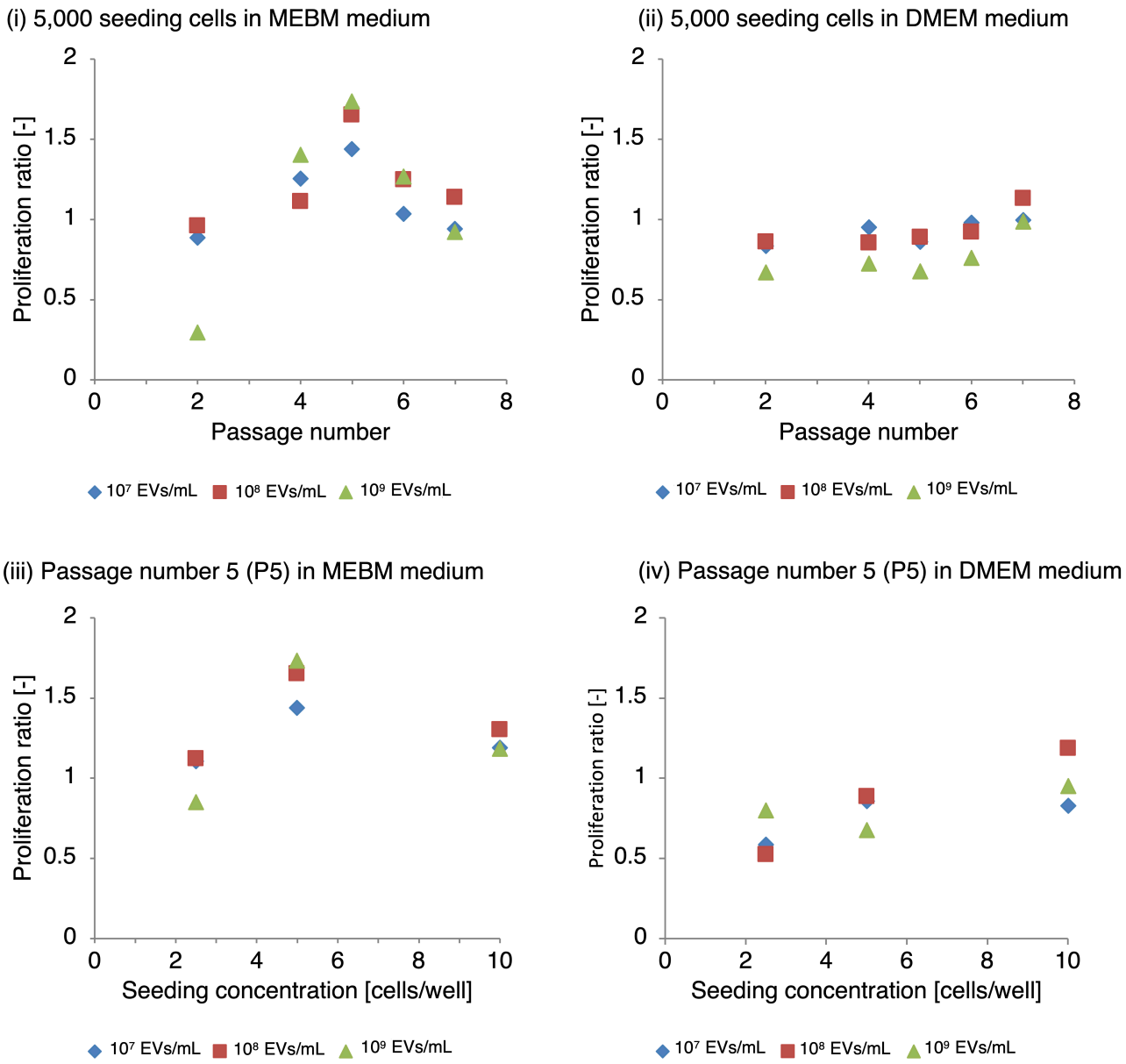

Fig. 30 The cell proliferation test.

The MCF10A cells were cultured in various condition parameters, including cell culture medium, cell passage number, cell seeding concentration, and concentration of added EVs to evaluate the abnormal proliferation rate. It was confirmed that MCF10A cells at passage number 5 (P5) which were seeded at 5000 cells/well and cultured in MEBM medium with the condition of 10^8 to 10^9 EVs/mL were optimal for cell proliferation test.

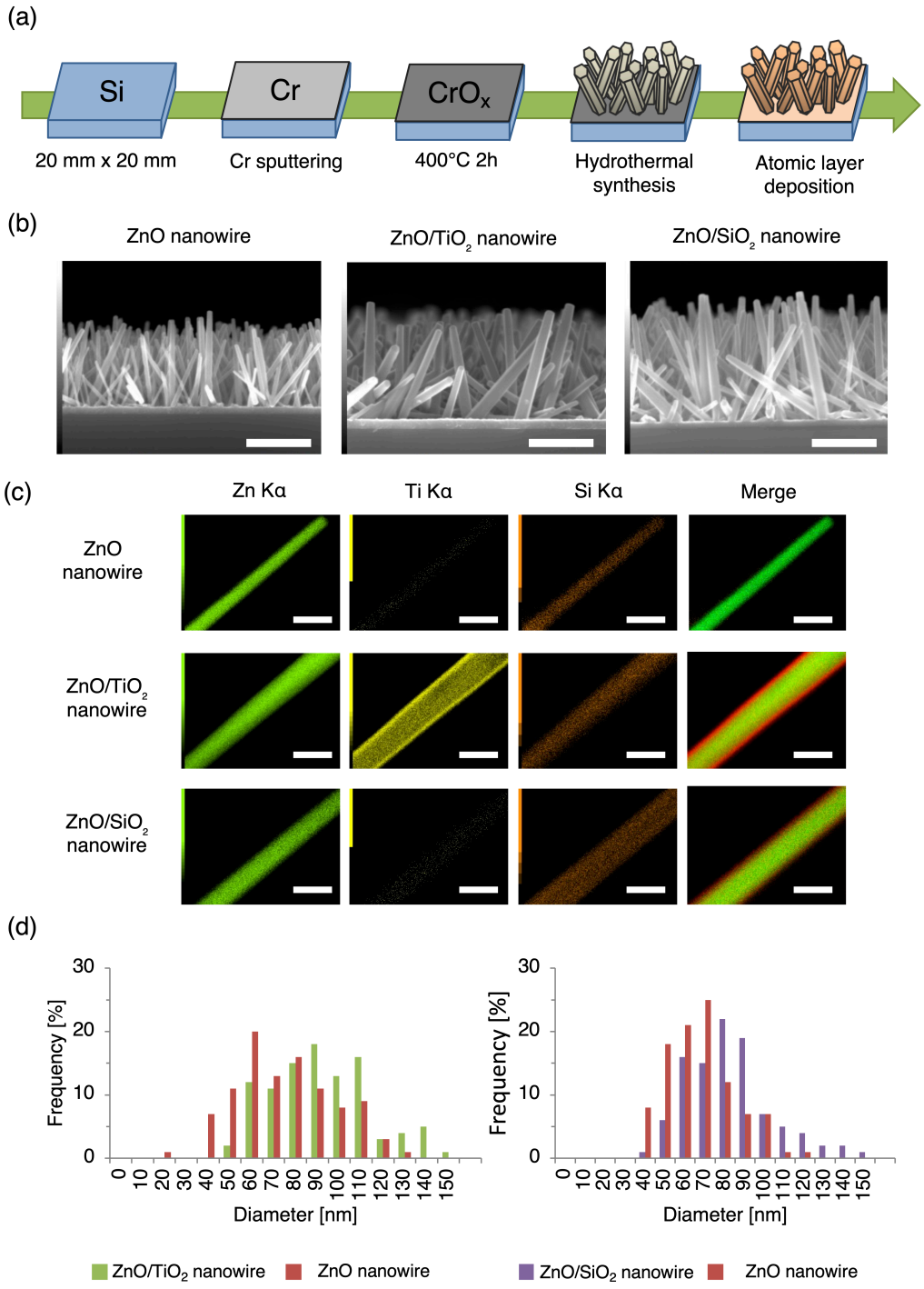

Fig. 31 Fabrication and characterization of oxide nanowires.

(a) ZnO nanowires were fabricated on Cr seeding layer on Si substrate using a hydrothermal method and the oxide layers (TiO_2 and SiO_2) were deposited by atomic layer deposition (ALD) technique. (b) Cross-sectional SEM images of oxide nanowires. The scale bar = 1000 nm. (c) STEM-EDS mapping analysis of oxide nanowires showed a thin layer of TiO_2 and SiO_2 on ZnO nanowire surfaces. The scale bar = 200 nm. (d) The histograms of oxide nanowires diameter comparing between ZnO nanowires (before deposition) and ZnO/TiO_2 nanowires and ZnO/SiO_2 nanowires (after deposition). *N = 100* nanowires/sample.

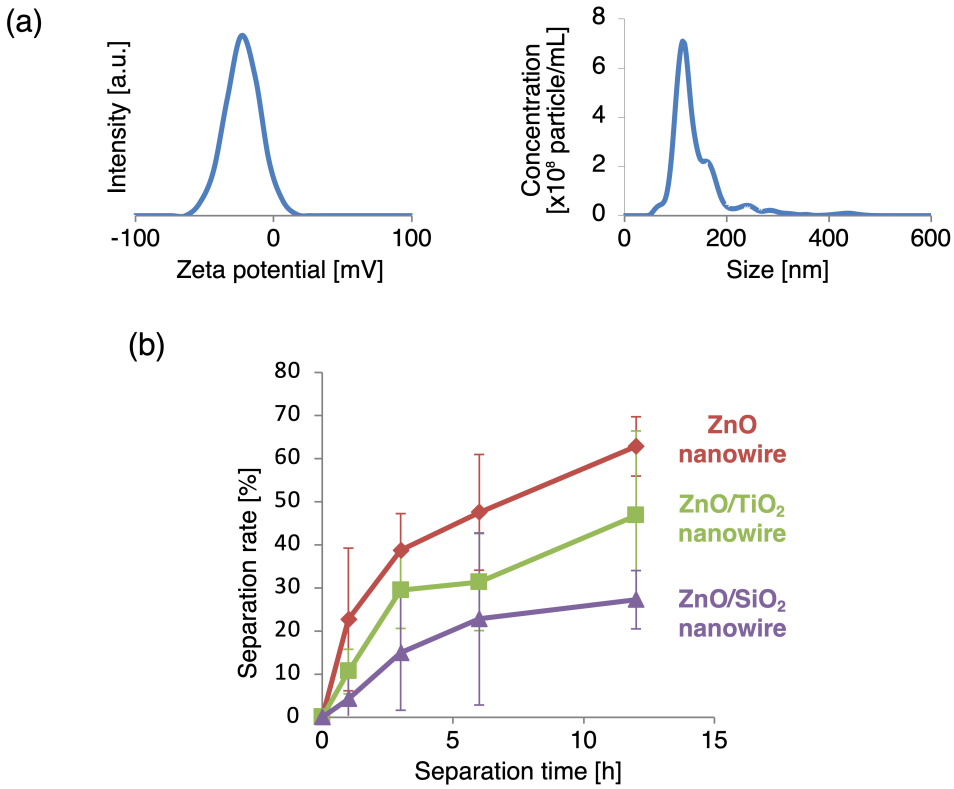

Fig. 32 Surface charge-based EV capture ability of oxide nanowire devices.

(a) The vesicles had an average zeta potential (ζ) of -22.5 mV and average diameter of 140.1 nm. (b) The EVs were introduced into devices integrated ZnO nanowires, ZnO/ TiO_2 nanowires, or ZnO/SiO_2 nanowires, and the EV separation ability was evaluated by comparing the EV concentrations before and after introduction into the devices.

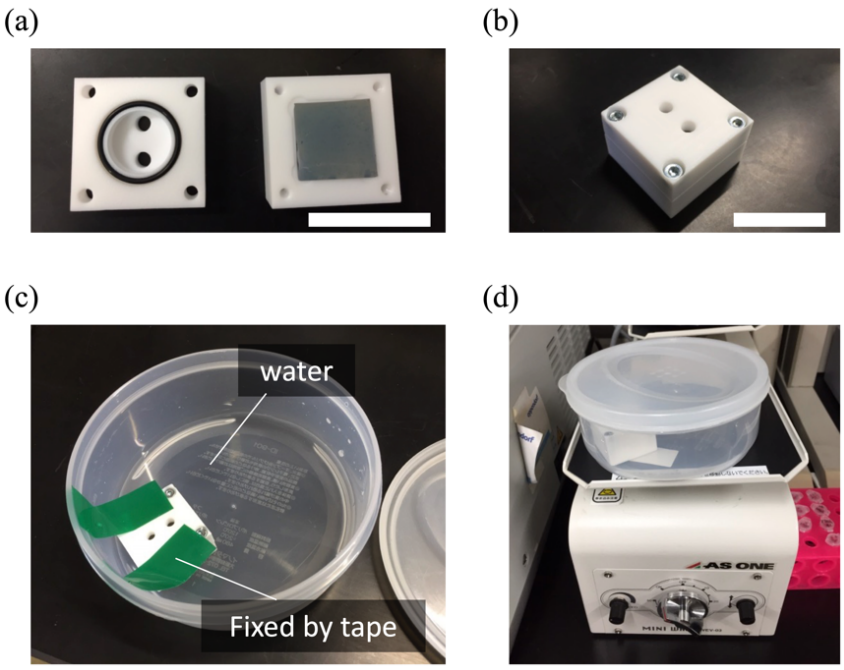

Fig. 33 The configuration of a nanowire device and experimental setting.

The nanowire substrate was aligned on the lower block, and assembled with the upper block into a single integrated device that was tightened together by screws. The holder was placed in a closed container filled with an amount of water to prevent the sample evaporation. The 1 mL of EV-suspended PBS was supplied and incubated in the chamber at room temperature for 1, 3, 6, and 12 h with a shaker.

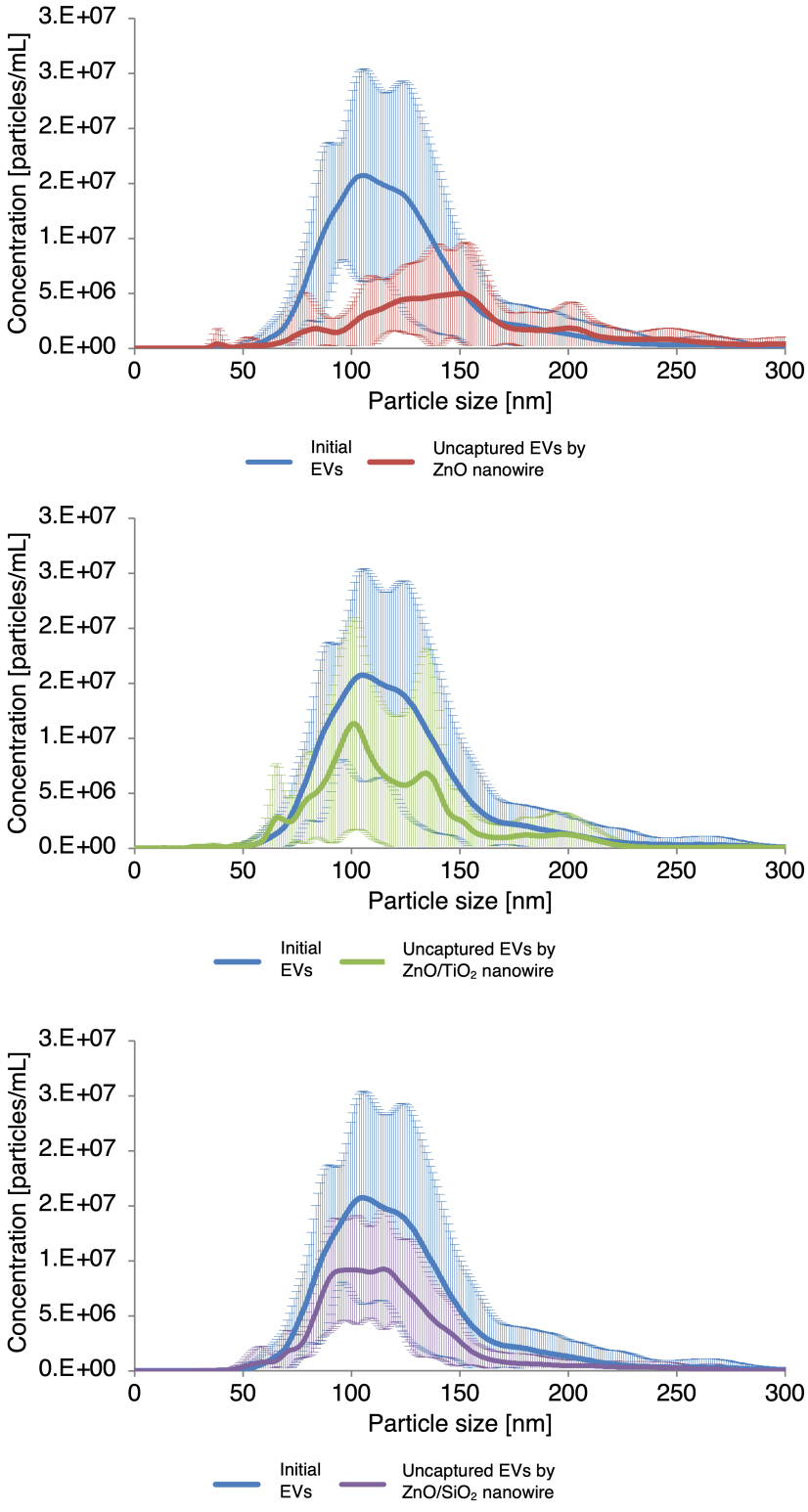

Fig. 34 The size distribution comparing initial EVs and uncaptured EVs by oxide nanowires.

This suggests the possibility of EV subgroups were specifically separated in each metal oxide material.

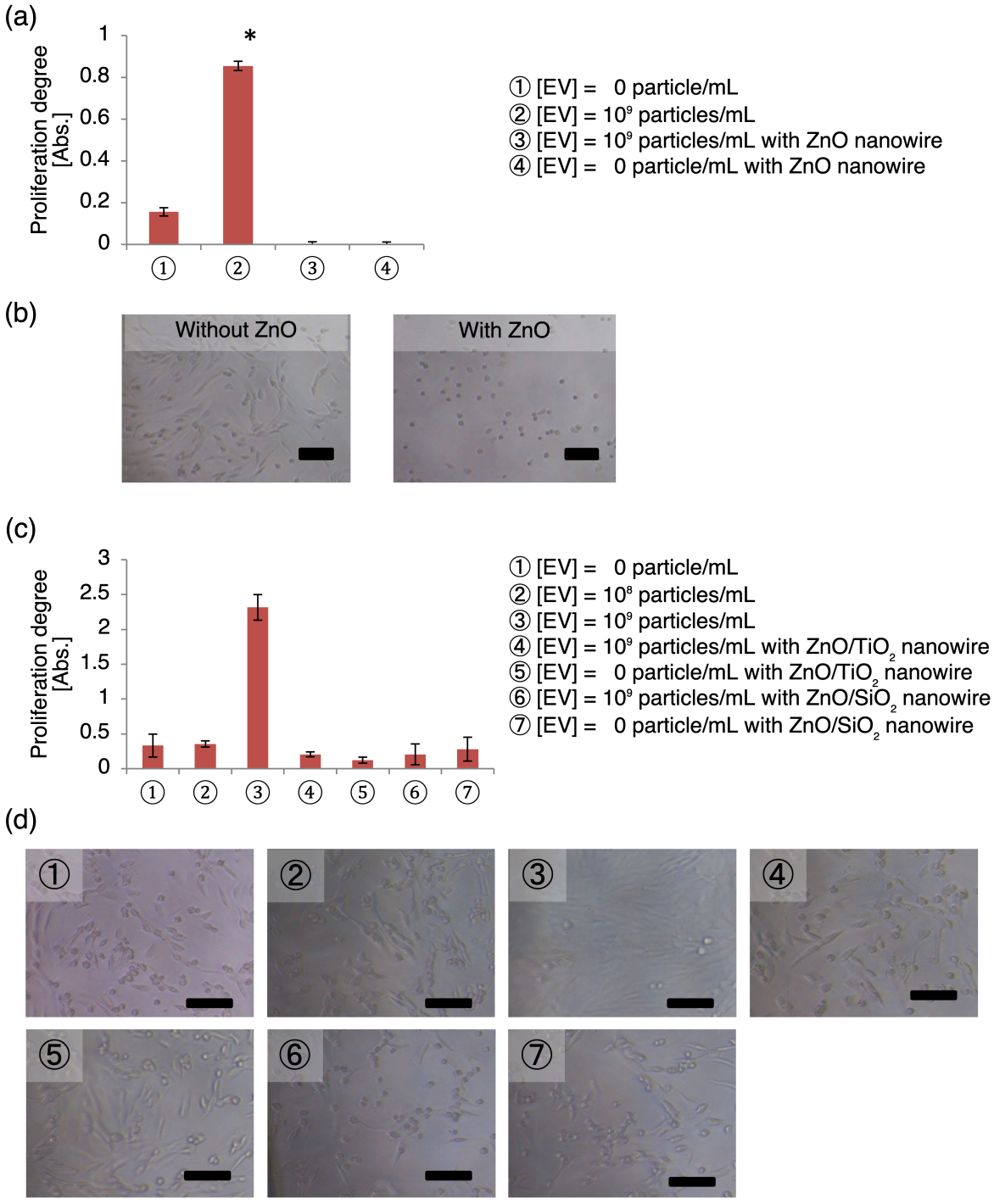

Fig. 35 Evaluation of cancer metastasis inhibitory by cell proliferation test using oxide nanowire devices.

(a) When ZnO nanowire device was used, the degree of normal cell proliferation was zero and (b) the microscopic observation found that cell growth was stopped or cells died due to the cytotoxicity of the ZnO nanowires. The scale bar = 100 μm. (c) In cases of ZnO/TiO_2 and ZnO/SiO_2 nanowires, the suppression of abnormal growth of MCF10A cells was observed by the EV eliminating using these types of nanowire device and (d) the cells grew in the normal state compared to control condition. The scale bar = 100 μm.

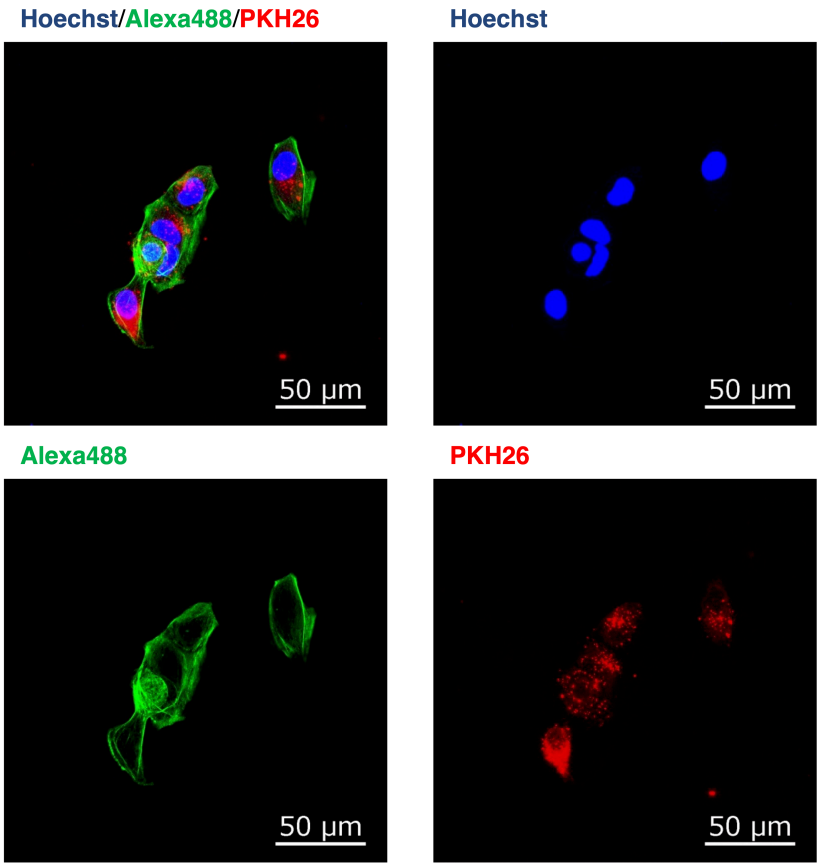

Fig. 36 The localization of cancer cell-derived EVs in epithelia MCF10A cells.

A red fluorescent dye (PKH26) was used for EV tracking. The confocal microscopic imaging showed PKH26-labelled EVs were found assembled inside the cytoplasm of MCF10A cells, indicating the diffusion of EVs into the recipient cells.

Table 6 The NGS analysis of miRNAs extracted from MDA-MB-231 cancer cell-derived EVs.

hsa-miR-148a-3p	hsa-miR-182-5p	hsa-miR-425-5p	hsa-miR-671-3p	hsa-miR-103a-3p
hsa-miR-151a-3p	hsa-miR-127-3p	hsa-miR-582-3p	hsa-miR-126-5p	hsa-miR-107
hsa-miR-100-5p	hsa-miR-146b-5p	hsa-miR-93-5p	hsa-miR-22-5p	hsa-miR-9-3p
hsa-miR-122-5p	hsa-miR-99b-3p	hsa-miR-320d	hsa-miR-29c-3p	hsa-miR-339-5p
hsa-let-7f-5p	hsa-miR-941	hsa-miR-30c-2-3p	hsa-miR-374a-5p	hsa-miR-9-5p
hsa-let-7a-5p	hsa-miR-215-5p	hsa-miR-30e-3p	hsa-miR-7706	hsa-miR-382-3p
hsa-miR-21-5p	hsa-miR-184	hsa-miR-7-5p	hsa-miR-326	hsa-miR-142-5p
hsa-miR-423-5p	hsa-miR-191-5p	hsa-miR-412-5p	hsa-miR-382-5p	hsa-miR-4433b-3p
hsa-let-7i-5p	hsa-miR-224-5p	hsa-miR-200c-3p	hsa-miR-3934-5p	hsa-miR-106b-5p
hsa-let-7g-5p	hsa-miR-147b	hsa-miR-206	hsa-miR-378c	hsa-miR-342-5p
hsa-miR-30a-5p	hsa-miR-574-5p	hsa-miR-125b-1-3p	hsa-miR-378d	hsa-miR-199a-5p
hsa-miR-25-3p	hsa-miR-409-3p	hsa-miR-142-3p	hsa-miR-659-5p	hsa-miR-223-5p
hsa-miR-92a-3p	hsa-miR-361-3p	hsa-miR-744-5p	hsa-miR-937-3p	hsa-miR-30e-5p
hsa-miR-146a-5p	hsa-miR-379-5p	hsa-miR-204-3p	hsa-miR-181a-2-3p	hsa-miR-335-3p
hsa-miR-486-5p	hsa-miR-192-5p	hsa-miR-493-5p	hsa-miR-629-5p	hsa-miR-370-3p
hsa-miR-30d-5p	hsa-miR-503-5p	hsa-miR-6873-3p	hsa-miR-140-5p	hsa-miR-654-5p
hsa-miR-24-3p	hsa-miR-320c	hsa-miR-3678-5p	hsa-miR-374b-5p	hsa-miR-150-5p
hsa-miR-99b-5p	hsa-miR-126-3p	hsa-miR-200a-3p	hsa-miR-219a-1-3p	hsa-miR-28-5p
hsa-miR-320a	hsa-miR-186-5p	hsa-miR-24-2-5p	hsa-miR-2110	hsa-let-7b-3p
hsa-let-7b-5p	hsa-miR-125b-5p	hsa-miR-139-5p	hsa-miR-561-5p	hsa-miR-1292-5p
hsa-miR-451a	hsa-miR-381-3p	hsa-miR-7704	hsa-miR-760	hsa-miR-155-5p
hsa-miR-222-3p	hsa-miR-1307-3p	hsa-miR-1273d	hsa-miR-877-5p	hsa-miR-185-3p
hsa-miR-30a-3p	hsa-miR-28-3p	hsa-miR-133a-3p	hsa-miR-223-3p	hsa-miR-196b-5p
hsa-miR-10a-5p	hsa-miR-30c-5p	hsa-miR-328-3p	hsa-miR-125a-3p	hsa-miR-200a-5p
hsa-miR-10b-5p	hsa-miR-26b-5p	hsa-miR-330-3p	hsa-miR-1269b	hsa-miR-200b-5p
hsa-miR-183-5p	hsa-miR-32-5p	hsa-let-7a-3p	hsa-miR-16-5p	hsa-miR-217
hsa-miR-101-3p	hsa-miR-584-5p	hsa-miR-185-5p	hsa-miR-194-5p	hsa-miR-23b-5p
hsa-let-7e-5p	hsa-miR-98-5p	hsa-miR-152-3p	hsa-miR-27b-5p	hsa-miR-3138
hsa-miR-27a-3p	hsa-miR-432-5p	hsa-miR-214-3p	hsa-miR-331-5p	hsa-miR-3158-3p
hsa-miR-181a-5p	hsa-miR-29a-3p	hsa-miR-542-3p	hsa-miR-1468-5p	hsa-miR-335-5p
hsa-miR-27b-3p	hsa-miR-125a-5p	hsa-miR-1283	hsa-miR-361-5p	hsa-miR-424-5p
hsa-miR-99a-5p	hsa-miR-144-3p	hsa-miR-129-5p	hsa-miR-199a-3p	hsa-miR-4488
hsa-let-7c-5p	hsa-miR-23b-3p	hsa-miR-130b-5p	hsa-miR-199b-3p	hsa-miR-4642
hsa-miR-423-3p	hsa-miR-92b-3p	hsa-miR-21-3p	hsa-miR-15b-5p	hsa-miR-486-3p
hsa-miR-106b-3p	hsa-miR-493-3p	hsa-miR-30b-5p	hsa-miR-222-5p	hsa-miR-548ah-3p
hsa-miR-26a-5p	hsa-miR-208b-3p	hsa-miR-505-3p	hsa-miR-323a-3p	hsa-miR-548p
hsa-miR-140-3p	hsa-miR-625-3p	hsa-miR-664a-5p	hsa-miR-369-5p	hsa-miR-589-5p
hsa-miR-532-5p	hsa-miR-197-3p	hsa-miR-144-5p	hsa-miR-375	hsa-miR-660-5p
hsa-miR-320b	hsa-let-7d-5p	hsa-miR-299-5p	hsa-miR-484	hsa-miR-6866-5p
hsa-miR-148b-3p	hsa-miR-8485	hsa-miR-519a-5p	hsa-miR-4326	
hsa-miR-221-3p	hsa-miR-1246	hsa-miR-769-5p	hsa-miR-1307-5p	
hsa-miR-128-3p	hsa-miR-136-5p	hsa-miR-218-5p	hsa-miR-4745-5p	
hsa-miR-378a-3p	hsa-miR-20a-5p	hsa-miR-411-5p	hsa-miR-191-3p	
hsa-miR-27a-5p	hsa-miR-19b-3p	hsa-miR-1306-3p	hsa-miR-615-3p	
hsa-miR-181b-5p	hsa-miR-1180-3p	hsa-miR-181a-3p	hsa-miR-130a-3p	
hsa-miR-23a-3p	hsa-miR-574-3p	hsa-miR-421	hsa-miR-29c-5p	
hsa-miR-143-3p	hsa-miR-455-5p	hsa-miR-424-3p	hsa-miR-145-3p	
hsa-miR-22-3p	hsa-miR-16-2-3p	hsa-miR-4504	hsa-miR-149-5p	
	hsa-miR-4746-5p	hsa-miR-516a-5p	hsa-miR-429	
	hsa-miR-7641	hsa-let-7d-3p	hsa-miR-330-5p	
	hsa-miR-3615			

Chapter 6. Concluding Remarks and Future Perspectives

1. In the nanowire chemical property study (chapter 2), three types of metal oxide nanowires with different surface chemistry were used for evaluating the most suitable candidate for label-free EV capture. We have demonstrated that our nanowire device could achieve membrane protein profiling of EV subsets obtained through surface charge-based capture from biological samples. The positively charged surface of the ZnO (bare) nanowires had an important role in the charge-based capture of negatively charged EVs that we then used for in-situ profiling of EV membrane proteins, CD9, CD63, CD81, and CD147. The ZnO (bare) nanowires allowed us to obtain a higher expression level ratio (CD147/CD9) from colon cancer cell-derived EVs and to detect an expression level ratio (CD147/CD9) from the EVs of a healthy volunteer urine sample. Our methodology showed the potential to provide a novel indicator of the EV subset role (surface charge) for cancer diagnosis, although we need to perform further trials for the confirmation of the indicator. Since we have already identified cancer-related microRNAs from urine samples using ZnO nanowires, we expect it would also be possible to identify the membrane protein-based markers from urine samples after making a correlation between in-situ EV profiling and EV-encapsulated microRNAs. At this point, a startup company (Craif Inc.) has already introduced a ZnO nanowire-based device to the market based on microRNA profiling, and in the future, in-situ EV profiling should come to be commercialized widely. Although we need to perform more trials for the highly precise cancer diagnosis, the present results have led us to believe that our developed approach will be a powerful tool which offers a new strategy for researchers to perform cancer diagnosis using urine samples.

2. In the nanowire physical property study (chapter 3), we achieved fabricating ZnO nanowires with different morphologies and crystallinities using an ammonia-assisted hydrothermal method, and we comprehensively analysed the crystalline nature and oriented growth of the synthesized nanowires by X-ray diffraction analysis and selected area electron diffraction using high resolution transmission electron microscopy. This is the first study to identify the effects of crystallinity and morphology of ZnO nanowires grown hydrothermally with NH_3 addition on their electrostatic properties for capturing EVs. As found from results of the XRD and HRTEM analyses, the crystal structures of all samples had the main characteristics of the ZnO wurtzite phase, but they were also mixed with zinc blende phase when grown under some conditions, making them suitable for EV capture on the nanowires. Considering the crystallinity and the morphology of the nanowires, the nanowires grown for 6 h with NH_3 ammonia addition offered the highest EV capture performance due to the presence of zinc blende phase and high density of the nanowires. These findings are expected to facilitate the realization of tunable nanowires with high potential suitability for integration into

advanced label-free EV capture devices which will open up opportunities for further fundamental studies (*i.e.*, adsorption mechanisms by biomolecules) and alternative applications in high-performance integrated nanowire devices.

3. In the classification of EV subpopulations by crystallinity and elution assay (chapter 4), we developed a new methodology for specific separation and classification of EV subpopulations using oxide nanowire microfluidic devices based on physically and chemically specific surface adsorption onto nanowire surfaces and specific sequential elution. The characterization of EV numbers and quantification of carried molecules including membrane protein markers and EV-encapsulated miRNAs were analyzed to confirm feasibility and specific isolation of the device. The recovered EV subsets obtained through charge-based isolation would provide a unique insight into EV information corresponding to EV contents, offer a new understanding of small EV heterogeneity base on surface charges in tumor cell biology as well as would be beneficial for the development of high precision of cancer diagnostic and therapeutic strategy.

4. In the alternative application of nanowire device in therapeutic purpose (chapter 5), we describe an EV-elimination device using nanowires which can specifically remove EV-miRNAs from cancer cell supernatant for inhibiting abnormal growth in recipient cells without toxicity to the cells. EVs from breast adenocarcinoma cells (MDA-MB-231) supernatant were incubated within an integrated device that induces charge-based interaction and captures the vesicles onto oxide nanowire surfaces. The cleansed medium was then transferred to the culture environment of mammary gland epithelial cells (MCF10A), the proliferation rate was evaluated. The results showed that positively charged ZnO nanowires allowed us to isolate the highest numbers of EVs, however cytotoxicity was found. Interestingly, the devices integrated with ZnO/TiO_2 nanowires and ZnO/SiO_2 nanowires, which have negatively charged surface, could offer sufficient isolation capacity to partially remove EV numbers to be lower than the threshold value of causing the abnormal growth and cytotoxicity was not found with these nanowires. These results provide a proof-of-concept for the use of oxide nanowire as a promising EVs isolation platform, namely blood purification therapy, in order to inhibit the spread of metastases in cancer progression. This research provides new possibilities for the development of future therapeutic strategies. However, further experiment needs to be performed to confirm the inhibitory effect whether it came from depletion of EVs or other essential growth factors for the epithelia cells.

From our discoveries and developments throughout the thesis, we explored the insights in modification and utilization of oxide nanowire feasibilities as a highly efficient and flexible platform with tunable properties for customized application in both of cancer diagnostic and therapeutic purposes. We recently achieved greater performance of the devices with high sensitivity and selectivity in EV capture and isolation. However, the downstream analysis of the collected molecules in various subpopulations, including EVs and its cargos, and their clinical applications have not been comprehensively discussed yet. Moreover, the different mechanisms of capture EVs using nanowires were shown, but the identification and detailed discussion are still unclear. To know for the certain, future research efforts will be focusing on analyzing the interactions based on diverse adsorption and desorption events for deeper understanding and unveiling the distinct mechanisms. Regardless, it is foreseeable that due to their unique chemical and physical characteristics, nanowire-based microfluidics will become a powerful tool in the near future for EV isolation, classification, and elimination devices, providing infinite power to overcome limitations of current conventional methods for accurate early diagnosis and efficient treatment of cancers.

Acknowledgements

I would like to thank the following people, without whom I would not have been able to complete this research, and without whom I would not have delightfully made it through my PhD!

First of all, the Baba Lab team at Nagoya University, I would like to express my sincere gratitude to my supervisor Prof. BABA Yoshinobu for his valuable guidance during this research. He is excellent with no doubts, and also the kindest sensei that one student could have in his/her good and tough time in academic life. I feel very lucky to have him as a role model in real life showing me how a scientist dedicates his life in researching and impactfully contributes it to the betterment of the society. Baba laboratory is such a big and warm school for me and other young scientists. I am really grateful to have you as my PhD supervisor and I do respect you from the bottom of my heart.

To Assoc. Prof. YASUI Takao, my advisor and research mentor, without you I could not see myself as a PhD degree holder and as an independent researcher. Throughout the process, I have learnt and grown up a lot from working with you. Since day one we met, you showed me great passion and sharp vision in doing high quality research. And most of all, you were always supportive and encouraged me when I faced a hard time. Thank you so much, I really needed it.

I would like to thank you to other Baba Lab's senseis, Des. Prof. YUKAWA Hiroshi, Des. Assoc. Prof. ONOSHIMA Daisuke, Des. Assoc. Prof. ARIMA Akihide, Des. Assis. Prof. ZHU Zetao for all of their supervision and suggestion in our regular and non-regular meetings for the betterment of my research. All of senseis has created a really great environment for students to pursue their educational achievement and enjoy the journey with generous guidance along the way. We are lucky to have you, thank you very much.

I thank all the former and current lab members of the Baba Lab as well as our kind staff Ms. URABE Yoko, Ms. SANO Takako, and Ms. IIDA Mikiko for supporting me in studying and living in Japan. Without you, I would definitely have a really tough management in life during my study. You made my life easier and helped me a lot to be able to concentrate only on my research. Special thank you to, Mr. NAGANAWA Tsuyoshi and Mr. NAKAMURA Yuta, the former Baba lab's students who had a huge contribution to my research in chapter 3 and 5. As well as all former and current Japanese, Thai, and international students who taught me the technical experiments and also spent enjoyable time inside and outside the school together. I do miss the Baba lab's trips, parties, sports and cultural activities we had before the pandemic hit. This is the real student life in abroad that I always wished for and I will remember it in the rest of my life! I do hope to see you again either in Japan or somewhere else.

I would like to thank you Prof. MURAKAMI Hiroki and Prof. NARUTAKI Ayae, the thesis and defense committee, for their constructive comments and suggestions. I really enjoyed discussing with you to strengthen and improve my research giving me a sense of completion and of a job well done after the revision.

I am also thankful to NAGOYA UNIVERSTY and Graduate School of Engineering, the well-designed system and very considerate staff, for creating a unique and friendly environment for scientific and non-scientific researchers, and for foreign students in particular. The support was always provided when students were in need in a critical situation. It made me feel secured during my study and I do appreciate that. I also enjoyed picking and taking not only academic classes, training program, seminar, but also intercultural activities, career consultant, job hunting workshop provided by the school so much.

I also would like to say thank you to my former advisors at Chulalongkorn University, Prof. Vudhichai Parasuk, Prof. Tawachai Tuntulani, Prof. Sumrit Wacharasindhu, and Assis. Prof. Pannee Leeladee, my referees and academic advisors, who built up a great foundation in Chemistry since I was an undergrad student, always provided advice and support for me to pursue my research career and PhD in a grad school.

I would like to say big thank you to the NANOTEC team in Thailand, Dr. Wiyong Kanwansupamonkon, Dr. Annop Klamchuen, Dr. Suwimon Boonrungsiman, Dr. Chaweewan Sapacharoenkun, Ms. Panita Kasamechonchung, Mr. Tuksadon Wuthikhun, and Mr. Visittapong Yordsri, who first introduced me to the nanomaterial research field. Thank you very much for your support when I was working as a research assistant, and until now while I was studying my PhD far away from you. The journey would not have been started and completed without your support.

I am grateful for all the people in my life outside of science. Friends in Japan, especially Thai friends from The Society of Nagoya, you made my life in Japan joyful and memorable. Also, I am really happy to have supportive friends outside Japan who always cheered me up in every step of the journey.

Finally, and most of all, I would like to highly thank my family for their endless understanding, encouraging, supporting and all everything I needed. Thank you for being by my side, always.

References

1. M. Iero, R. Valenti, V. Huber, P. Filipazzi, G. Parmiani, S. Fais and L. Rivoltini, *Cell Death Differ*, 2008, **15**, 80-88.
2. K. Al-Nedawi, B. Meehan, J. Micallef, V. Lhotak, L. May, A. Guha and J. Rak, *Nat Cell Biol*, 2008, **10**, 619-624.
3. J. Skog, T. Wurdinger, S. van Rijn, D. H. Meijer, L. Gainche, M. Sena-Esteves, W. T. Curry, Jr., B. S. Carter, A. M. Krichevsky and X. O. Breakefield, *Nat Cell Biol*, 2008, **10**, 1470-1476.
4. A. V. Vlassov, S. Magdaleno, R. Setterquist and R. Conrad, *Biochim Biophys Acta*, 2012, **1820**, 940-948.
5. C. J. Koch, R. A. Lustig, X. Y. Yang, W. T. Jenkins, R. L. Wolf, M. Martinez-Lage, A. Desai, D. Williams and S. M. Evans, *Transl Oncol*, 2014, **7**, 752-758.
6. J. Zhang, S. Li, L. Li, M. Li, C. Guo, J. Yao and S. Mi, *Genomics Proteomics Bioinformatics*, 2015, **13**, 17-24.
7. S. Rahmati, F. Shojaei, A. Shojaeian, L. Rezakhani and M. B. Dehkordi, *Chem Phys Lipids*, 2020, **226**, 104836.
8. J. Jabalee, R. Towle and C. Garnis, *Cells*, 2018, **7**.
9. A. T. Reiner, K. W. Witwer, B. W. M. van Balkom, J. de Beer, C. Brodie, R. L. Corteling, S. Gabrielsson, M. Gimona, A. G. Ibrahim, D. de Kleijn, C. P. Lai, J. Lotvall, H. A. Del Portillo, I. G. Reischl, M. Riazifar, C. Salomon, H. Tahara, W. S. Toh, M. H. M. Wauben, V. K. Yang, Y. Yang, R. W. Y. Yeo, H. Yin, B. Giebel, E. Rohde and S. K. Lim, *Stem Cells Transl Med*, 2017, **6**, 1730-1739.
10. B. W. Sodar, A. Kovacs, T. Visnovitz, E. Pallinger, K. Vekey, G. Pocsfalvi, L. Turiak and E. I. Buzas, *Expert Rev Proteomics*, 2017, **14**, 1073-1090.
11. O. Ruhen and K. Meehan, *Proteomics*, 2019, **19**, e1800155.
12. M. Yanez-Mo, P. R. Siljander, Z. Andreu, A. B. Zavec, F. E. Borras, E. I. Buzas, K. Buzas, E. Casal, F. Cappello, J. Carvalho, E. Colas, A. Cordeiro-da Silva, S. Fais, J. M. Falcon-Perez, I. M. Ghobrial, B. Giebel, M. Gimona, M. Graner, I. Gursel, M. Gursel, N. H. Heegaard, A.

Hendrix, P. Kierulf, K. Kokubun, M. Kosanovic, V. Kralj-Iglic, E. M. Kramer-Albers, S. Laitinen, C. Lasser, T. Lener, E. Ligeti, A. Line, G. Lipps, A. Llorente, J. Lotvall, M. Mancek-Keber, A. Marcilla, M. Mittelbrunn, I. Nazarenko, E. N. Nolte-'t Hoen, T. A. Nyman, L. O'Driscoll, M. Olivan, C. Oliveira, E. Pallinger, H. A. Del Portillo, J. Reventos, M. Rigau, E. Rohde, M. Sammar, F. Sanchez-Madrid, N. Santarem, K. Schallmoser, M. S. Ostenfeld, W. Stoorvogel, R. Stukelj, S. G. Van der Grein, M. H. Vasconcelos, M. H. Wauben and O. De Wever, *J Extracell Vesicles*, 2015, **4**, 27066.

13. R. Wiggins, A. Glatfelter, B. Kshirsagar and T. Beals, *Laboratory Investigation*, 1987, **56**, 264-272.
14. T. Pisitkun, R. F. Shen and M. A. Knepper, *Proceedings of the National Academy of Sciences of the United States of America*, 2004, **101**, 13368-13373.
15. W. C. Xu, G. Qian, A. Q. Liu, Y. Q. Li and H. Q. Zou, *Chinese Medical Journal*, 2018, **131**, 1357-1364.
16. I. Panfoli, *Translational Cancer Research*, 2017, **6**, S1389-S1393.
17. B. Dhondt, J. Van Deun, S. Vermaerke, A. de Marco, N. Lumen, O. De Wever and A. Hendrix, *International Journal of Biochemistry & Cell Biology*, 2018, **99**, 236-256.
18. T. Murakami, C. M. Yamamoto, T. Akino, H. Tanaka, N. Fukuzawa, H. Suzuki, T. Osawa, T. Tsuji, T. Seki and H. Harada, *Oncotarget*, 2018, **9**, 32810-32821.
19. J. Linxweiler and K. Junker, *Nat Rev Urol*, 2019.
20. Y. Li, Y. Zhang, F. Qiu and Z. Qiu, *Electrophoresis*, 2011, **32**, 1976-1983.
21. E. R. Barros and C. A. Carvajal, *Frontiers in Endocrinology*, 2017, **8**.
22. A. Santelli, I. O. Sun, A. Eirin, A. M. Abumoawad, J. R. Woollard, A. Lerman, S. C. Textor, A. S. Puranik and L. O. Lerman, *J Am Heart Assoc*, 2019, **8**, e012584.
23. M. Y. Konoshenko, E. A. Lekchnov, A. V. Vlassov and P. P. Laktionov, *Biomed Res Int*, 2018, **2018**, 8545347.
24. C. Thery, K. W. Witwer, E. Aikawa, M. J. Alcaraz, J. D. Anderson, R. Andriantsitohaina, A. Antoniou, T. Arab, F. Archer, G. K. Atkin-Smith, D. C. Ayre, J. M. Bach, D. Bachurski, H. Baharvand, L. Balaj, S. Baldacchino, N. N. Bauer, A. A. Baxter, M. Bebawy, C. Beckham, A.

Bedina Zavec, A. Benmoussa, A. C. Berardi, P. Bergese, E. Bielska, C. Blenkiron, S. Bobis-Wozowicz, E. Boilard, W. Boireau, A. Bongiovanni, F. E. Borras, S. Bosch, C. M. Boulanger, X. Breakefield, A. M. Breglio, M. A. Brennan, D. R. Brigstock, A. Brisson, M. L. Broekman, J. F. Bromberg, P. Bryl-Gorecka, S. Buch, A. H. Buck, D. Burger, S. Busatto, D. Buschmann, B. Bussolati, E. I. Buzas, J. B. Byrd, G. Camussi, D. R. Carter, S. Caruso, L. W. Chamley, Y. T. Chang, C. Chen, S. Chen, L. Cheng, A. R. Chin, A. Clayton, S. P. Clerici, A. Cocks, E. Cocucci, R. J. Coffey, A. Cordeiro-da-Silva, Y. Couch, F. A. Coumans, B. Coyle, R. Crescitelli, M. F. Criado, C. D'Souza-Schorey, S. Das, A. Datta Chaudhuri, P. de Candia, E. F. De Santana, O. De Wever, H. A. Del Portillo, T. Demaret, S. Deville, A. Devitt, B. Dhondt, D. Di Vizio, L. C. Dieterich, V. Dolo, A. P. Dominguez Rubio, M. Dominici, M. R. Dourado, T. A. Driedonks, F. V. Duarte, H. M. Duncan, R. M. Eichenberger, K. Ekstrom, S. El Andaloussi, C. Elie-Caille, U. Erdbrugger, J. M. Falcon-Perez, F. Fatima, J. E. Fish, M. Flores-Bellver, A. Forsonits, A. Frelet-Barrand, F. Fricke, G. Fuhrmann, S. Gabrielsson, A. Gamez-Valero, C. Gardiner, K. Gartner, R. Gaudin, Y. S. Gho, B. Giebel, C. Gilbert, M. Gimona, I. Giusti, D. C. Goberdhan, A. Gorgens, S. M. Gorski, D. W. Greening, J. C. Gross, A. Gualerzi, G. N. Gupta, D. Gustafson, A. Handberg, R. A. Haraszti, P. Harrison, H. Hegyesi, A. Hendrix, A. F. Hill, F. H. Hochberg, K. F. Hoffmann, B. Holder, H. Holthofer, B. Hosseinkhani, G. Hu, Y. Huang, V. Huber, S. Hunt, A. G. Ibrahim, T. Ikezu, J. M. Inal, M. Isin, A. Ivanova, H. K. Jackson, S. Jacobsen, S. M. Jay, M. Jayachandran, G. Jenster, L. Jiang, S. M. Johnson, J. C. Jones, A. Jong, T. Jovanovic-Talisman, S. Jung, R. Kalluri, S. I. Kano, S. Kaur, Y. Kawamura, E. T. Keller, D. Khamari, E. Khomyakova, A. Khvorova, P. Kierulf, K. P. Kim, T. Kislinger, M. Klingeborn, D. J. Klinke, 2nd, M. Kornek, M. M. Kosanovic, A. F. Kovacs, E. M. Kramer-Albers, S. Krasemann, M. Krause, I. V. Kurochkin, G. D. Kusuma, S. Kuypers, S. Laitinen, S. M. Langevin, L. R. Languino, J. Lannigan, C. Lasser, L. C. Laurent, G. Lavieu, E. Lazaro-Ibanez, S. Le Lay, M. S. Lee, Y. X. F. Lee, D. S. Lemos, M. Lenassi, A. Leszczynska, I. T. Li, K. Liao, S. F. Libregts, E. Ligeti, R. Lim, S. K. Lim, A. Line, K. Linnemannstons, A. Llorente, C. A. Lombard, M. J. Lorenowicz, A. M. Lorincz, J. Lotvall, J. Lovett, M. C. Lowry, X. Loyer, Q. Lu, B. Lukomska, T. R. Lunavat, S. L. Maas, H. Malhi, A. Marcilla, J. Mariani, J. Mariscal, E.

S. Martens-Uzunova, L. Martin-Jaular, M. C. Martinez, V. R. Martins, M. Mathieu, S. Mathivanan, M. Maugeri, L. K. McGinnis, M. J. McVey, D. G. Meckes, Jr., K. L. Meehan, I. Mertens, V. R. Minciacchi, A. Moller, M. Moller Jorgensen, A. Morales-Kastresana, J. Morhayim, F. Mullier, M. Muraca, L. Musante, V. Mussack, D. C. Muth, K. H. Myburgh, T. Najrana, M. Nawaz, I. Nazarenko, P. Nejsum, C. Neri, T. Neri, R. Nieuwland, L. Nimrichter, J. P. Nolan, E. N. Nolte-'t Hoen, N. Noren Hooten, L. O'Driscoll, T. O'Grady, A. O'Loghlen, T. Ochiya, M. Olivier, A. Ortiz, L. A. Ortiz, X. Osteikoetxea, O. Ostergaard, M. Ostrowski, J. Park, D. M. Pegtel, H. Peinado, F. Perut, M. W. Pfaffl, D. G. Phinney, B. C. Pieters, R. C. Pink, D. S. Pisetsky, E. Pogge von Strandmann, I. Polakovicova, I. K. Poon, B. H. Powell, I. Prada, L. Pulliam, P. Quesenberry, A. Radeghieri, R. L. Raffai, S. Raimondo, J. Rak, M. I. Ramirez, G. Raposo, M. S. Rayyan, N. Regev-Rudzki, F. L. Ricklefs, P. D. Robbins, D. D. Roberts, S. C. Rodrigues, E. Rohde, S. Rome, K. M. Rouschop, A. Rughetti, A. E. Russell, P. Saa, S. Sahoo, E. Salas-Huenuleo, C. Sanchez, J. A. Saugstad, M. J. Saul, R. M. Schiffelers, R. Schneider, T. H. Schoyen, A. Scott, E. Shahaj, S. Sharma, O. Shatnyeva, F. Shekari, G. V. Shelke, A. K. Shetty, K. Shiba, P. R. Siljander, A. M. Silva, A. Skowronek, O. L. Snyder, 2nd, R. P. Soares, B. W. Sodar, C. Soekmadji, J. Sotillo, P. D. Stahl, W. Stoorvogel, S. L. Stott, E. F. Strasser, S. Swift, H. Tahara, M. Tewari, K. Timms, S. Tiwari, R. Tixeira, M. Tkach, W. S. Toh, R. Tomasini, A. C. Torrecilhas, J. P. Tosar, V. Toxavidis, L. Urbanelli, P. Vader, B. W. van Balkom, S. G. van der Grein, J. Van Deun, M. J. van Herwijnen, K. Van Keuren-Jensen, G. van Niel, M. E. van Royen, A. J. van Wijnen, M. H. Vasconcelos, I. J. Vechetti, Jr., T. D. Veit, L. J. Vella, E. Velot, F. J. Verweij, B. Vestad, J. L. Vinas, T. Visnovitz, K. V. Vukman, J. Wahlgren, D. C. Watson, M. H. Wauben, A. Weaver, J. P. Webber, V. Weber, A. M. Wehman, D. J. Weiss, J. A. Welsh, S. Wendt, A. M. Wheelock, Z. Wiener, L. Witte, J. Wolfram, A. Xagorari, P. Xander, J. Xu, X. Yan, M. Yanez-Mo, H. Yin, Y. Yuana, V. Zappulli, J. Zarubova, V. Zekas, J. Y. Zhang, Z. Zhao, L. Zheng, A. R. Zheutlin, A. M. Zickler, P. Zimmermann, A. M. Zivkovic, D. Zocco and E. K. Zuba-Surma, *J Extracell Vesicles*, 2018, **7**, 1535750.

25. T. A. Hartjes, S. Mytnyk, G. W. Jenster, V. van Steijn and M. E. van Royen, *Bioengineering (Basel)*, 2019, **6**.

26. J. M. Street, E. H. Koritzinsky, D. M. Glispie, R. A. Star and P. S. Yuen, *Adv Clin Chem*, 2017, **78**, 103-122.

27. M. L. Merchant, I. M. Rood, J. K. J. Deegens and J. B. Klein, *Nat Rev Nephrol*, 2017, **13**, 731-749.

28. L. He, D. Zhu, J. Wang and X. Wu, *Int J Mol Med*, 2019, **43**, 83-90.

29. I. M. Rood, J. K. Deegens, M. L. Merchant, W. P. Tamboer, D. W. Wilkey, J. F. Wetzels and J. B. Klein, *Kidney Int*, 2010, **78**, 810-816.

30. A. H. Gheinani, M. Vogeli, U. Baumgartner, E. Vassella, A. Draeger, F. C. Burkhard and K. Monastyrskaya, *Scientific Reports*, 2018, **8**.

31. S. Cho, H. C. Yang and W. J. Rhee, *Process Biochemistry*, 2020, **88**, 197-203.

32. E. Oeyen, K. Van Mol, G. Baggerman, H. Willems, K. Boonen, C. Rolfo, P. Pauwels, A. Jacobs, K. Schildermans, W. C. Cho and I. Mertens, *J Extracell Vesicles*, 2018, **7**, 1490143.

33. B. Talebjedi, N. Tasnim, M. Hoorfar, G. F. Mastromonaco and M. De Almeida Monteiro Melo Ferraz, *Frontiers in Veterinary Science*, 2021, **7**.

34. J. C. Contreras-Naranjo, H.-J. Wu and V. M. Ugaz, *Lab on a Chip*, 2017, **17**, 3558-3577.

35. J. Wang, P. Ma, D. H. Kim, B.-F. Liu and U. Demirci, *Nano Today*, 2021, **37**, 101066.

36. M.-C. N. Le and H. Z. Fan, *Biomedical Materials*, 2021.

37. T. Yasui, T. Yanagida, S. Ito, Y. Konakade, D. Takeshita, T. Naganawa, K. Nagashima, T. Shimada, N. Kaji, Y. Nakamura, I. A. Thiodorus, Y. He, S. Rahong, M. Kanai, H. Yukawa, T. Ochiya, T. Kawai and Y. Baba, *Sci Adv*, 2017, **3**, e1701133.

38. I. Evans-Osses, L. H. Reichembach and M. I. Ramirez, *Parasitol Res*, 2015, **114**, 3567-3575.

39. G. Raposo and W. Stoorvogel, *Journal of Cell Biology*, 2013, **200**, 373-383.

40. R. Szatanek, J. Baran, M. Siedlar and M. Baj-Krzyworzeka, *Int J Mol Med*, 2015, **36**, 11-17.

41. A. Bobrie, M. Colombo, G. Raposo and C. Théry, *Traffic*, 2011, **12**, 1659-1668.

42. J. S. Schorey and S. Bhatnagar, *Traffic*, 2008, **9**, 871-881.

43. C. Thery, M. Ostrowski and E. Segura, *Nat Rev Immunol*, 2009, **9**, 581-593.

44. G. van Niel, I. Porto-Carreiro, S. Simoes and G. Raposo, *J Biochem*, 2006, **140**, 13-21.

45. E. Willms, H. J. Johansson, I. Mäger, Y. Lee, K. E. M. Blomberg, M. Sadik, A. Alaarg, C. I. E. Smith, J. Lehtiö, S. El Andaloussi, M. J. A. Wood and P. Vader, *Scientific Reports*, 2016, **6**, 22519.

46. M. Iero, R. Valenti, V. Huber, P. Filipazzi, G. Parmiani, S. Fais and L. Rivoltini, *Cell Death & Differentiation*, 2008, **15**, 80-88.

47. F. Properzi, M. Logozzi and S. Fais, *Biomark Med*, 2013, **7**, 769-778.

48. D. D. Taylor and C. Gercel-Taylor, *Gynecol Oncol*, 2008, **110**, 13-21.

49. D. K. Jeppesen, A. M. Fenix, J. L. Franklin, J. N. Higginbotham, Q. Zhang, L. J. Zimmerman, D. C. Liebler, J. Ping, Q. Liu, R. Evans, W. H. Fissell, J. G. Patton, L. H. Rome, D. T. Burnette and R. J. Coffey, *Cell*, 2019, **177**, 428-445.e418.

50. M. F. Peterson, N. Otoc, J. K. Sethi, A. Gupta and T. J. Antes, *Methods*, 2015, **87**, 31-45.

51. A. Hoshino, B. Costa-Silva, T.-L. Shen, G. Rodrigues, A. Hashimoto, M. Tesic Mark, H. Molina, S. Kohsaka, A. Di Giannatale, S. Ceder, S. Singh, C. Williams, N. Soplop, K. Uryu, L. Pharmer, T. King, L. Bojmar, A. E. Davies, Y. Ararso, T. Zhang, H. Zhang, J. Hernandez, J. M. Weiss, V. D. Dumont-Cole, K. Kramer, L. H. Wexler, A. Narendran, G. K. Schwartz, J. H. Healey, P. Sandstrom, K. Jørgen Labori, E. H. Kure, P. M. Grandgenett, M. A. Hollingsworth, M. de Sousa, S. Kaur, M. Jain, K. Mallya, S. K. Batra, W. R. Jarnagin, M. S. Brady, O. Fodstad, V. Muller, K. Pantel, A. J. Minn, M. J. Bissell, B. A. Garcia, Y. Kang, V. K. Rajasekhar, C. M. Ghajar, I. Matei, H. Peinado, J. Bromberg and D. Lyden, *Nature*, 2015, **527**, 329-335.

52. S. A. Melo, L. B. Luecke, C. Kahlert, A. F. Fernandez, S. T. Gammon, J. Kaye, V. S. LeBleu, E. A. Mittendorf, J. Weitz, N. Rahbari, C. Reissfelder, C. Pilarsky, M. F. Fraga, D. Piwnica-Worms and R. Kalluri, *Nature*, 2015, **523**, 177-182.

53. Y. Kitano, K. Aoki, F. Ohka, S. Yamazaki, K. Motomura, K. Tanahashi, M. Hirano, T. Naganawa, M. Iida, Y. Shiraki, T. Nishikawa, H. Shimizu, J. Yamaguchi, S. Maeda, H. Suzuki, T. Wakabayashi, Y. Baba, T. Yasui and A. Natsume, *ACS Appl. Mater. Inter.*, 2021, **in press**, 10.1021/acsami.1021c01754.

54. G. A. Parks, *Chemical Reviews*, 1965, **65**, 177-198.

55. S. Rahong, T. Yasui, N. Kaji and Y. Baba, *Lab on a Chip*, 2016, **16**, 1126-1138.

56. E. K. Sackmann, A. L. Fulton and D. J. Beebe, *Nature*, 2014, **507**, 181-189.

57. Q. L. Liu, T. Yasui, K. Nagashima, T. Yanagida, M. Hara, M. Horiuchi, Z. T. Zhu, H. Takahashi, T. Shimada, A. Arima and Y. Baba, *Journal of Physical Chemistry C*, 2020, **124**, 20563-20568.

58. J. Liu, K. Nagashima, H. Yamashita, W. Mizukami, J. Uzuhashi, T. Hosomi, M. Kanai, X. Zhao, Y. Miura, G. Zhang, T. Takahashi, M. Suzuki, D. Sakai, B. Samransuksamer, Y. He, T. Ohkubo, T. Yasui, Y. Aoki, J. C. Ho, Y. Baba and T. Yanagida, *Communications Materials*, 2020, **1**, 58.

59. D. Sakai, K. Nagashima, H. Yoshida, M. Kanai, Y. He, G. Zhang, X. Zhao, T. Takahashi, T. Yasui, T. Hosomi, Y. Uchida, S. Takeda, Y. Baba and T. Yanagida, *Sci Rep*, 2019, **9**, 14160.

60. R. A. Dragovic, C. Gardiner, A. S. Brooks, D. S. Tannetta, D. J. P. Ferguson, P. Hole, B. Carr, C. W. G. Redman, A. L. Harris, P. J. Dobson, P. Harrison and I. L. Sargent, *Nanomedicine-Nanotechnology Biology and Medicine*, 2011, **7**, 780-788.

61. C. Borzi, L. Calzolari, A. M. Ferretti, L. Caleca, U. Pastorino, G. Sozzi and O. Fortunato, *Cell Death Dis*, 2019, **10**, 759.

62. C. Charoenviriyakul, Y. Takahashi, M. Morishita, A. Matsumoto, M. Nishikawa and Y. Takakura, *Eur J Pharm Sci*, 2017, **96**, 316-322.

63. M. Dash, K. Palaniyandi, S. Ramalingam, S. Sahabudeen and N. S. Raja, *Biochim Biophys Acta Biomembr*, 2021, **1863**, 183490.

64. T. Hikita, M. Miyata, R. Watanabe and C. Oneyama, *Scientific Reports*, 2018, **8**, 14035.

65. H. Im, H. Shao, Y. I. Park, V. M. Peterson, C. M. Castro, R. Weissleder and H. Lee, *Nature Biotechnology*, 2014, **32**, 490-495.

66. M. Logozzi, A. De Milito, L. Lugini, M. Borghi, L. Calabrò, M. Spada, M. Perdicchio, M. L. Marino, C. Federici, E. Iessi, D. Brambilla, G. Venturi, F. Lozupone, M. Santinami, V. Huber, M. Maio, L. Rivoltini and S. Fais, *PLOS ONE*, 2009, **4**, e5219.

67. Y. Yoshioka, N. Kosaka, Y. Konishi, H. Ohta, H. Okamoto, H. Sonoda, R. Nonaka, H. Yamamoto, H. Ishii, M. Mori, K. Furuta, T. Nakajima, H. Hayashi, H. Sugisaki, H. Higashimoto, T. Kato, F. Takeshita and T. Ochiya, *Nature Communications*, 2014, **5**, 3591.

68. K. Boye, J. M. Nesland, B. Sandstad, M. Haugland Haugen, G. M. Mælandsmo and K. Flatmark, *British Journal of Cancer*, 2012, **107**, 667-674.

69. D. S. Choi, D. Y. Choi, B. S. Hong, S. C. Jang, D. K. Kim, J. Lee, Y. K. Kim, K. P. Kim and Y. S. Gho, *J Extracell Vesicles*, 2012, **1**.

70. J. R. Edgar, *BMC Biology*, 2016, **14**, 46.

71. D. Xiao, J. Ohlendorf, Y. Chen, D. D. Taylor, S. N. Rai, S. Waigel, W. Zacharias, H. Hao and K. M. McMasters, *PLOS ONE*, 2012, **7**, e46874.

72. V. R. Minciacchi, M. R. Freeman and D. Di Vizio, *Semin Cell Dev Biol*, 2015, **40**, 41-51.

73. G. K. Patel, M. A. Khan, H. Zubair, S. K. Srivastava, M. d. Khushman, S. Singh and A. P. Singh, *Sci. Rep.*, 2019, **9**, 5335.

74. S. Gandham, X. Su, J. Wood, A. L. Nocera, S. C. Alli, L. Milane, A. Zimmerman, M. Amiji and A. R. Ivanov, *Trends Biotechnol.*, 2020, **38**, 1066-1098.

75. T.-W. Lo, Z. Zhu, E. Purcell, D. Watza, J. Wang, Y.-T. Kang, S. Jolly, D. Nagrath and S. Nagrath, *Lab Chip*, 2020, **20**, 1762-1770.

76. H. Jeon, S.-K. Kang and M.-S. Lee, *PLoS One*, 2020, **15**, e0235793.

77. H. K. Woo, V. Sunkara, J. Park, T. H. Kim, J. R. Han, C. J. Kim, H. I. Choi, Y. K. Kim and Y. K. Cho, *ACS Nano*, 2017, **11**, 1360-1370.

78. E. Oeyen, K. Van Mol, G. Baggerman, H. Willems, K. Boonen, C. Rolfo, P. Pauwels, A. Jacobs, K. Schildermans, W. C. Cho and I. Mertens, *J. Extracell. Vesicles*, 2018, **7**, 1490143.

79. T. Yasui, T. Yanagida, S. Ito, Y. Konakade, D. Takeshita, T. Naganawa, K. Nagashima, T. Shimada, N. Kaji, Y. Nakamura, I. A. Thiodorus, Y. He, S. Rahong, M. Kanai, H. Yukawa, T. Ochiya, T. Kawai and Y. Baba, *Sci. Adv.*, 2017, **3**, e1701133.

80. R. G. Hobbs, N. Petkov and J. D. Holmes, *Chemistry of Materials*, 2012, **24**, 1975-1991.

81. B. Tian, T. J. Kempa and C. M. Lieber, *Chemical Society Reviews*, 2009, **38**, 16-24.

82. N. P. Dasgupta, J. W. Sun, C. Liu, S. Brittman, S. C. Andrews, J. Lim, H. W. Gao, R. X. Yan and P. D. Yang, *Advanced Materials*, 2014, **26**, 2137-2184.

83. P. C. McIntyre and A. Fontcuberta i Morral, *Materials Today Nano*, 2020, **9**, 100058.

84. V. Gerbreders, M. Krasovska, E. Sledevskis, A. Gerbreders, I. Mihailova, E. Tamanis and A. Ogurcovs, *CrystEngComm*, 2020, **22**, 1346-1358.

85. P. Ambhorkar, Z. Wang, H. Ko, S. Lee, K.-I. Koo, K. Kim and D.-I. D. Cho, *Micromachines*, 2018, **9**, 679.

86. N. Caicedo, R. Leturcq, J.-P. Raskin, D. Flandre and D. Lenoble, *Sensors and Actuators B: Chemical*, 2019, **297**, 126602.

87. B. Tian and C. M. Lieber, *Chemical Reviews*, 2019, **119**, 9136-9152.

88. A. M. Nahhas, *American Journal of Nanomaterials*, 2021, **8**, 18-31.

89. T. Suwatthanarak, I. A. Thiodorus, M. Tanaka, T. Shimada, D. Takeshita, T. Yasui, Y. Baba and M. Okochi, *Lab Chip*, 2020.

90. M. Musa, T. Yasui, Z. Zhu, K. Nagashima, M. Ono, Q. Liu, H. Takahashi, T. Shimada, A. Arima, T. Yanagida and Y. Baba, *Anal Sci*, 2021, **37**, 1139-1145.

91. H. Takahashi, T. Yasui, H. Kashida, K. Makino, K. Shinjo, Q. Liu, T. Shimada, S. Rahong, N. Kaji, H. Asanuma and Y. Baba, *Nanotechnology*, 2021, **32**.

92. T. Yasui, P. Paisrisarn, T. Yanagida, Y. Konakade, Y. Nakamura, K. Nagashima, M. Musa, I. A. Thiodorus, H. Takahashi, T. Naganawa, T. Shimada, N. Kaji, T. Ochiya, T. Kawai and Y. Baba, *Biosens Bioelectron*, 2021, **194**, 113589.

93. H. Takahashi, T. Yasui, A. Klamchuen, N. Khemasiri, T. Wuthikhun, P. Paisrisarn, K. Shinjo, Y. Kitano, K. Aoki, A. Natsume, S. Rahong and Y. Baba, *Nanomaterials (Basel)*, 2021, **11**.

94. Y. He, T. Yanagida, K. Nagashima, F. W. Zhuge, G. Meng, B. Xu, A. Klamchuen, S. Rahong, M. Kanai, X. M. Li, M. Suzuki, S. Kai and T. Kawai, *Journal of Physical Chemistry C*, 2013, **117**, 1197-1203.

95. V. Strano, R. G. Urso, M. Scuderi, K. O. Iwu, F. Simone, E. Ciliberto, C. Spinella and S. Mirabella, *The Journal of Physical Chemistry C*, 2014, **118**, 28189-28195.

96. P. Kasamechonchung, M. Horprathum, K. Boonpavanitchakul, N. Supaka, P. Prompinit, W. Kangwansupamonkon, A. Somboonkaew, J. Wetcharungsri, S. Pratontep, S. Porntheeraphat and A. Klamchuen, *Physica Status Solidi a-Applications and Materials Science*, 2015, **212**, 394-400.

97. Q. Huang, L. Fang, X. Chen and M. R. Saleem, *Journal of Alloys and Compounds*, 2011, **509**, 9456-9459.

98. L.-Y. Chen, Y.-T. Yin, C.-H. Chen and J.-W. Chiou, *The Journal of Physical Chemistry C*, 2011, **115**, 20913-20919.

99. T. Demes, C. Ternon, F. Morisot, D. Riassetto, M. Legallais, H. Roussel and M. Langlet, *Applied Surface Science*, 2017, **410**, 423-431.

100. R. Hao, X. Deng, J. Zhang, H. Jang, Y. Zeng and H. Guo, 2017.

101. R. Parize, J. D. Garnier, E. Appert, O. Chaix-Pluchery and V. Consonni, *ACS omega*, 2018, **3**, 12457-12464.

102. J. Joo, B. Y. Chow, M. Prakash, E. S. Boyden and J. M. Jacobson, *Nature Materials*, 2011, **10**, 596-601.

103. T. H. Kwon, K. Kim, S. H. Park, A. A. Annamalai and M. J. Lee, *International Journal of Nanotechnology*, 2013, **10**, 681.

104. L. Liu, K. Hong, X. Ge, D. Liu and M. Xu, *The Journal of Physical Chemistry C*, 2014, **118**, 15551-15555.

105. R. Kumar, O. Al-Dossary, G. Kumar and A. Umar, *Nano-Micro Letters*, 2015, **7**, 97-120.

106. J. Wang, X. Li, C. Teng, Y. Xia, J. Xu, D. Xie, L. Xiang and S. Komarneni, *Journal of Materials Chemistry C*, 2016, **4**, 5755-5765.

107. S. V. Kurudirek, K. C. Pradel and C. J. Summers, *Journal of Alloys and Compounds*, 2017, **702**, 700-709.

108. A. C. Campos, S. C. Paes, B. S. Correa, G. A. Cabrera-Pasca, M. S. Costa, C. S. Costa, L. Otubo and A. W. Carbonari, *Acs Applied Nano Materials*, 2020, **3**, 175-185.

109. G. van Niel, G. D'Angelo and G. Raposo, *Nat Rev Mol Cell Biol*, 2018, **19**, 213-228.

110. L. M. Doyle and M. Z. Wang, *Cells*, 2019, **8**, 727.

111. R. Xu, A. Rai, M. Chen, W. Suwakulsiri, D. W. Greening and R. J. Simpson, *Nat Rev Clin Oncol*, 2018, **15**, 617-638.

112. L. Han, E. W. F. Lam and Y. Sun, *Molecular Cancer*, 2019, **18**, 59.

113. Y. Gao, Y. Qin, C. Wan, Y. Sun, J. Meng, J. Huang, Y. Hu, H. Jin and K. Yang, *Frontiers in Oncology*, 2021, **11**.

114. L. K. Chin, T. Son, J.-S. Hong, A.-Q. Liu, J. Skog, C. M. Castro, R. Weissleder, H. Lee and H. Im, *ACS nano*, 2020, **14**, 14528-14548.

115. S. Sharma, M. K. Masud, Y. V. Kaneti, P. Rewatkar, A. Koradia, M. S. A. Hossain, Y. Yamauchi, A. Popat and C. Salomon, *Small*, 2021, **17**, e2102220.

116. Z. Zhuo, J. Wang, Y. Luo, R. Zeng, C. Zhang, W. Zhou, K. Guo, H. Wu, W. Sha and H. Chen, *Acta Biomaterialia*, 2021, **134**, 13-31.

117. H. Zhang, D. Freitas, H. S. Kim, K. Fabijanic, Z. Li, H. Chen, M. T. Mark, H. Molina, A. B. Martin, L. Bojmar, J. Fang, S. Rampersaud, A. Hoshino, I. Matei, C. M. Kenific, M. Nakajima, A. P. Mutvei, P. Sansone, W. Buehring, H. Wang, J. P. Jimenez, L. Cohen-Gould, N. Paknejad, M. Brendel, K. Manova-Todorova, A. Magalhães, J. A. Ferreira, H. Osório, A. M. Silva, A. Massey, J. R. Cubillos-Ruiz, G. Galletti, P. Giannakakou, A. M. Cuervo, J. Blenis, R. Schwartz, M. S. Brady, H. Peinado, J. Bromberg, H. Matsui, C. A. Reis and D. Lyden, *Nature Cell Biology*, 2018, **20**, 332-343.

118. C. Xu, P. Shin, L. Cao and D. Gao, *Journal of Physical Chemistry C*, 2010, **114**, 125-129.

119. M. Law, L. E. Greene, J. C. Johnson, R. Saykally and P. D. Yang, *Nature Materials*, 2005, **4**, 455-459.

120. Y. Y. Zhang, M. K. Ram, E. K. Stefanakos and D. Y. Goswami, *Journal of Nanomaterials*, 2012, **2012**.

121. A. Ashrafi and C. Jagadish, *Journal of Applied Physics*, 2007, **102**.

122. N. Munoz-Aguirre, L. Martinez-Perez, S. Munoz-Aguirre, L. A. Flores-Herrera, E. V. Hernandez and O. Zelaya-Angel, *Materials*, 2019, **12**.

123. X. Huang, M. G. Willinger, H. Fan, Z. L. Xie, L. Wang, A. Klein-Hoffmann, F. Girgsdies, C. S. Lee and X. M. Meng, *Nanoscale*, 2014, **6**, 8787-8795.

124. S. Boubenia, A. S. Dahiya, G. Poulin-Vittrant, F. Morini, K. Nadaud and D. Alquier, *Scientific Reports*, 2017, **7**.

125. H. J. Joyce, J. Wong-Leung, Q. Gao, H. H. Tan and C. Jagadish, *Nano Letters*, 2010, **10**, 908-915.

126. K. Ikejiri, Y. Kitauchi, K. Tomioka, J. Motohisa and T. Fukui, *Nano Letters*, 2011, **11**, 4314-4318.

127. A. Jenichen, C. Engler and B. Rauschenbach, *Surface Science*, 2013, **613**, 74-79.

128. M. Ghosh, D. Karmakar, S. Basu, S. N. Jha, D. Bhattacharyya, S. C. Gadkari and S. K. Gupta, *Journal of Physics and Chemistry of Solids*, 2014, **75**, 543-549.

129. K. Momeni and H. Attariani, *Physical Chemistry Chemical Physics*, 2014, **16**, 4522-4527.

130. G. Midekessa, K. Godakumara, J. Ord, J. Viil, F. Lättekivi, K. Dissanayake, S. Kopanchuk, A. Rinken, A. Andronowska, S. Bhattacharjee, T. Rinken and A. Fazeli, *ACS Omega*, 2020, **5**, 16701-16710.

131. Z. N. Kayani, F. Saleemi and I. Batool, *Applied Physics A*, 2015, **119**, 713-720.

132. M. R. Parra and F. Z. Haque, *Journal of Materials Research and Technology*, 2014, **3**, 363-369.

133. E. Y. Shaba, J. O. Jacob, J. O. Tijani and M. A. T. Suleiman, *Applied Water Science*, 2021, **11**, 48.

134. R. C. Paolicelli, G. Bergamini and L. Rajendran, *Neuroscience*, 2019, **405**, 148-157.

135. J. Maia, S. Caja, M. C. Strano Moraes, N. Couto and B. Costa-Silva, *Frontiers in Cell and Developmental Biology*, 2018, **6**.

136. G. Berumen Sánchez, K. E. Bunn, H. H. Pua and M. Rafat, *Cell Communication and Signaling*, 2021, **19**, 104.

137. M. Verma, T. K. Lam, E. Hebert and R. L. Divi, *BMC Clinical Pathology*, 2015, **15**, 6.

138. Z. Zhao, S. Yang, A. Zhou, X. Li, R. Fang, S. Zhang, G. Zhao and P. Li, *Frontiers in Oncology*, 2021, **11**.

139. H. Wu, M. Fu, J. Liu, W. Chong, Z. Fang, F. Du, Y. Liu, L. Shang and L. Li, *Molecular Cancer*, 2021, **20**, 71.

140. M. Mohammadi, H. Zargartalebi, R. Salahandish, R. Aburashed, K. Wey Yong and A. Sanati-Nezhad, *Biosensors and Bioelectronics*, 2021, **183**, 113176.

141. T. Liangsupree, E. Multia and M. L. Riekkola, *J Chromatogr A*, 2021, **1636**, 461773.

142. E. Willms, C. Cabañas, I. Mäger, M. J. A. Wood and P. Vader, *Frontiers in Immunology*, 2018, **9**.

143. E. S. Martens-Uzunova, G. D. Kusuma, S. Crucitta, H. K. Lim, C. Cooper, J. E. Riches, A. Azad, T. Ochiya, G. M. Boyle, M. C. Southey, M. Del Re, R. Lim, G. A. Ramm, G. W. Jenster and C. Soekmadji, *J Extracell Vesicles*, 2021, **10**, e12136.

144. F. Cocozza, E. Grisard, L. Martin-Jaular, M. Mathieu and C. Théry, *Cell*, 2020, **182**, 262-262.e261.

145. N. Ludwig, T. L. Whiteside and T. E. Reichert, *International journal of molecular sciences*, 2019, **20**, 4684.

146. Y. X. F. Lee, H. Johansson, M. J. A. Wood and S. El Andaloussi, *Frontiers in Neuroscience*, 2019, **13**.

147. J. Van Deun, P. Mestdagh, R. Sormunen, V. Cocquyt, K. Vermaelen, J. Vandesompele, M. Bracke, O. De Wever and A. Hendrix, *Journal of Extracellular Vesicles*, 2014, **3**, 24858.

148. M. Mathieu, L. Martin-Jaular, G. Lavieu and C. Théry, *Nat Cell Biol*, 2019, **21**, 9-17.

149. A. Zijlstra and D. Di Vizio, *Nat Cell Biol*, 2018, **20**, 228-230.

150. R. Crescitelli, C. Lässer and J. Lötvall, *Nature Protocols*, 2021, **16**, 1548-1580.

151. S. Cavallaro, F. Pevere, F. Stridfeldt, A. Görgens, C. Paba, S. S. Sahu, D. R. Mamand, D. Gupta, S. El Andaloussi, J. Linnros and A. Dev, *Small*, 2021, **17**, e2008155.

152. G. Bordanaba-Florit, F. Royo, S. G. Kruglik and J. M. Falcón-Pérez, *Nature Protocols*, 2021, **16**, 3163-3185.

153. N. C. Martin, A. A. Pirie, L. V. Ford, C. L. Callaghan, K. McTurk, D. Lucy and D. G. Scrimger, *Sci Justice*, 2006, **46**, 179-184.

154. F. Wang, R. A. Cerione and M. A. Antonyak, *STAR Protocols*, 2021, **2**, 100295.

155. S. Gurung, D. Perocheau, L. Touramanidou and J. Baruteau, *Cell Communication and Signaling*, 2021, **19**, 47.

156. Z. Andreu and M. Yáñez-Mó, *Frontiers in Immunology*, 2014, **5**.

157. M. A. Livshits, E. Khomyakova, E. G. Evtushenko, V. N. Lazarev, N. A. Kulemin, S. E. Semina, E. V. Generozov and V. M. Govorun, *Sci Rep*, 2015, **5**, 17319.

158. T. Baranyai, K. Herczeg, Z. Onódi, I. Voszka, K. Módos, N. Marton, G. Nagy, I. Mäger, M. J. Wood, S. El Andaloussi, Z. Pálinkás, V. Kumar, P. Nagy, Á. Kittel, E. I. Buzás, P. Ferdinandy and Z. Giricz, *PLOS ONE*, 2015, **10**, e0145686.

159. S.-S. Lee, J.-H. Won, G. J. Lim, J. Han, J. Y. Lee, K.-O. Cho and Y.-K. Bae, *Cell Communication and Signaling*, 2019, **17**, 95.

160. M. Mathieu, N. Névo, M. Jouve, J. I. Valenzuela, M. Maurin, F. J. Verweij, R. Palmulli, D. Lankar, F. Dingli, D. Loew, E. Rubinstein, G. Boncompain, F. Perez and C. Théry, *Nature Communications*, 2021, **12**, 4389.

161. M. Simons and G. Raposo, *Curr Opin Cell Biol*, 2009, **21**, 575-581.

162. Y. Zhang, M. S. Kim, B. Jia, J. Yan, J. P. Zuniga-Hertz, C. Han and D. Cai, *Nature*, 2017, **548**, 52-57.

163. T. Maemura, S. Fukuyama, Y. Sugita, T. J. S. Lopes, T. Nakao, T. Noda and Y. Kawaoka, *J Infect Dis*, 2018, **217**, 1372-1382.

164. A. Schneider and M. Simons, *Cell Tissue Res*, 2013, **352**, 33-47.

165. H. Valadi, K. Ekstrom, A. Bossios, M. Sjostrand, J. J. Lee and J. O. Lotvall, *Nat Cell Biol*, 2007, **9**, 654-659.

166. J. Massague and A. C. Obenauf, *Nature*, 2016, **529**, 298-306.

167. A. H. Buck, G. Coakley, F. Simbari, H. J. McSorley, J. F. Quintana, T. Le Bihan, S. Kumar, C. Abreu-Goodger, M. Lear, Y. Harcus, A. Ceroni, S. A. Babayan, M. Blaxter, A. Ivens and R. M. Maizels, *Nat Commun*, 2014, **5**, 5488.

168. J. Rak, *Nature*, 2015, **527**, 312-314.

169. I. Wortzel, S. Dror, C. M. Kenific and D. Lyden, *Dev Cell*, 2019, **49**, 347-360.

170. C. Marar, B. Starich and D. Wirtz, *Nature Immunology*, 2021, **22**, 560-570.

171. C. Giordano, G. La Camera, L. Gelsomino, I. Barone, D. Bonofiglio, S. Ando and S. Catalano, *Cancers (Basel)*, 2020, **12**.

172. F. Cappello, M. Logozzi, C. Campanella, C. C. Bavisotto, A. Marcilla, F. Properzi and S. Fais, *Eur J Pharm Sci*, 2017, **96**, 93-98.

173. D. Hoshino, K. C. Kirkbride, K. Costello, E. S. Clark, S. Sinha, N. Grega-Larson, M. J. Tyska and A. M. Weaver, *Cell Rep*, 2013, **5**, 1159-1168.

174. E. R. Sauter, *Translational Cancer Research*, 2017, S1316-S1320.

175. S. A. Melo, H. Sugimoto, J. T. O'Connell, N. Kato, A. Villanueva, A. Vidal, L. Qiu, E. Vitkin, L. T. Perelman, C. A. Melo, A. Lucci, C. Ivan, G. A. Calin and R. Kalluri, *Cancer Cell*, 2014, **26**, 707-721.

176. C. Kahlert and R. Kalluri, *J Mol Med (Berl)*, 2013, **91**, 431-437.

177. Y. Kitano, K. Aoki, F. Ohka, S. Yamazaki, K. Motomura, K. Tanahashi, M. Hirano, T. Naganawa, M. Iida, Y. Shiraki, T. Nishikawa, H. Shimizu, J. Yamaguchi, S. Maeda, H. Suzuki, T. Wakabayashi, Y. Baba, T. Yasui and A. Natsume, *ACS Appl Mater Interfaces*, 2021, **13**, 17316-17329.

178. N. Tominaga, N. Kosaka, M. Ono, T. Katsuda, Y. Yoshioka, K. Tamura, J. Lotvall, H. Nakagama and T. Ochiya, *Nat Commun*, 2015, **6**, 6716.

179. L. T. Vu, J. Gong, T. T. Pham, Y. Kim and M. T. N. Le, *Cell Prolif*, 2020, **53**, e12877.

180. J. Chen, C. Hu and P. Pan, *Frontiers in physiology*, 2017, **8**, 1028-1028.

181. G. Rodrigues, A. Hoshino, C. M. Kenific, I. R. Matei, L. Steiner, D. Freitas, H. S. Kim, P. R. Oxley, I. Scandariato, I. Casanova-Salas, J. Dai, C. R. Badwe, B. Gril, M. Tesic Mark, B. D. Dill, H. Molina, H. Zhang, A. Benito-Martin, L. Bojmar, Y. Ararso, K. Offer, Q. LaPlant, W. Buehring, H. Wang, X. Jiang, T. M. Lu, Y. Liu, J. K. Sabari, S. J. Shin, N. Narula, P. S. Ginter, V. K. Rajasekhar, J. H. Healey, E. Meylan, B. Costa-Silva, S. E. Wang, S. Rafii, N. K. Altorki, C. M. Rudin, D. R. Jones, P. S. Steeg, H. Peinado, C. M. Ghajar, J. Bromberg, M. de Sousa, D. Pisapia and D. Lyden, *Nat Cell Biol*, 2019, **21**, 1403-1412.

182. J. H. Kang, M. Super, C. W. Yung, R. M. Cooper, K. Domansky, A. R. Graveline, T. Mammoto, J. B. Berthet, H. Tobin, M. J. Cartwright, A. L. Watters, M. Rottman, A. Waterhouse, A. Mammoto, N. Gamini, M. J. Rodas, A. Kole, A. Jiang, T. M. Valentin, A. Diaz, K. Takahashi and D. E. Ingber, *Nat Med*, 2014, **20**, 1211-1216.

183. T. Rimmelé and J. A. Kellum, *Critical Care*, 2011, **15**, 205.

184. F. Sanfilippo, G. Martucci, L. La Via, G. Cuttone, G. Dimarco, C. Pulizzi, A. Arcadipane and M. Astuto, *Artif Organs*, 2021, **45**, 1466-1476.

185. G. Villa, J. J. Zaragoza, A. Sharma, M. Neri, A. R. De Gaudio and C. Ronco, *Blood Purification*, 2014, **38**, 167-173.

186. B. Malard, C. Lambert and J. A. Kellum, *Intensive Care Medicine Experimental*, 2018, **6**, 12.

187. T. Tani, K. Numa, K. Hanasawa and M. Kodama, *Ther Apher*, 1998, **2**, 182-184.

188. N. Kimura, H. Tanaka, H. Kawaguchi, H. Eguchi and K. Endo, *Iryo Yakugaku (Japanese Journal of Pharmaceutical Health Care and Sciences)*, 2006, **32**, 314-319.

189. K. Kaizu, Y. Inada, A. Kawamura, S. Oda and H. Hirasawa, *Contrib Nephrol*, 2010, **166**, 4-10.

190. H. Yamada and S. Ohtsuru, *Journal of Intensive Care*, 2021, **9**, 74.

191. E. C. Poli, L. Alberio, A. Bauer-Doerries, C. Marcucci, A. Roumy, M. Kirsch, E. De Stefano, L. Liaudet and A. G. Schneider, *Critical Care*, 2019, **23**, 108.

192. M. Kosmulski, *Adv Colloid Interface Sci*, 2016, **238**, 1-61.

193. M. Kosmulski, *Advances in Colloid and Interface Science*, 2021, **296**, 102519.

194. J. Q. Gerlach and M. D. Griffin, *Mol Biosyst*, 2016, **12**, 1071-1081.

195. S. Y. Ko and H. Naora, *Int J Mol Sci*, 2020, **21**.

196. T. J. Brunner, P. Wick, P. Manser, P. Spohn, R. N. Grass, L. K. Limbach, A. Bruinink and W. J. Stark, *Environmental Science & Technology*, 2006, **40**, 4374-4381.

197. N. M. Franklin, N. J. Rogers, S. C. Apte, G. E. Batley, G. E. Gadd and P. S. Casey, *Environmental Science & Technology*, 2007, **41**, 8484-8490.

198. A. R. Pinho, F. Martins, M. E. V. Costa, A. M. R. Senos, O. Silva, M. L. Pereira and S. Rebelo, *Cells*, 2020, **9**.

199. L. X. Yan, Q. N. Wu, Y. Zhang, Y. Y. Li, D. Z. Liao, J. H. Hou, J. Fu, M. S. Zeng, J. P. Yun, Q. L. Wu, Y. X. Zeng and J. Y. Shao, *Breast Cancer Res*, 2011, **13**, R2.

200. L. Ma, J. Teruya-Feldstein and R. A. Weinberg, *Nature*, 2007, **449**, 682-688.

List of Scientific Papers for PhD Thesis

I. **Paisrisarn P**, Yasui T, Baba Y.

A method to analyze urinary extracellular vesicles.
Anal. Sci. 2020 Mar 13; 36(7):791-798. https://doi.org/10.2116/analsci.20R001. *Review.*

II. Yasui T, **Paisrisarn P**, Yanagida T, Konakade Y, Nakamura Y, Nagashima K, Musa M, Thiodorus IA, Takahashi H, Naganawa T, Shimada T, Kaji N, Ochiya T, Kawai T, Baba Y.

Molecular profiling of extracellular vesicles via charge-based capture using nanowire microfluidics.
Biosens. Bioelectron. 2021 Dec 15; 194:113589. https://doi.org/10.1016/j.bios.2021.113589.

III. **Paisrisarn P**, Yasui T, Zhu Z, Klamchuen A, Kasamechonchung P, Wuthikhun T, Yordsri V, Baba Y.

Tailoring ZnO nanowire crystallinity and morphology for label-free capturing of extracellular vesicles.
Nanoscale. 2022. *In Press*

IV. **Paisrisarn P**, Yasui T, Nakamura Y, Baba Y.

Elimination of cancer cell-derived extracellular vesicles by oxide nanowires for *in vitro* metastasis suppressing.
In Submission

V. **Paisrisarn P**, Yasui T, Tokeshi M, Baba Y.

Classifying tumor-specific extracellular vesicles via charge-based isolation using ZnO nanowire microfluidics.
In Manuscript

VI. **Paisrisarn P**, Yasui T, Baba Y.

Nanowire microfluidic devices for specific charge-based isolation of small extracellular vesicles.
MicroTAS. 2021 Oct 12; 1209-1210. *Proceedings.*

Scientific Papers Not Included in the Thesis

I. Ryuzaki S, Yasui T, Tsutsui M, Yokota K, Komoto Y, **Paisrisarn P**, Kaji N, Ito D, Tamada K, Ochiya T, Taniguchi M, Baba Y, Kawai T.

Rapid discrimination of extracellular vesicles by shape distribution analysis.
Anal. Chem. 2021 Apr 28; 93(18):7037-7044. https://doi.org/10.1021/acs.analchem.1c00258.

II. Takahashi H, Yasui T, Klamchuen A, Khemasiri N, Wuthikhun T, **Paisrisarn P**, Shinjo K, Kitano Y, Aoki K, Natsume A, Rahong S, Baba Y.

Annealed ZnO/Al_2O_3 core-shell nanowire as a platform to capture RNA in blood plasma.
Nanomaterials. 2021 Jul 7; 11(7):1768. https://doi.org/10.3390/nano11071768.